INDUCED SUPERCONDUCTIVITY IN THE TOPOLOGICAL INSULATOR MERCURY TELLURIDE

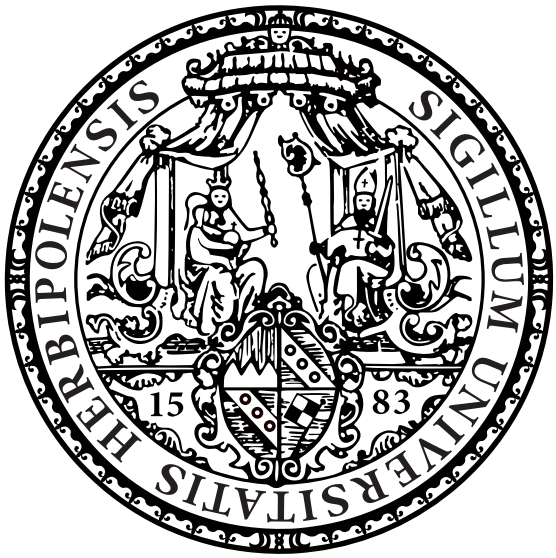

Dissertation

zur Erlangung des naturwissenschaftlichen Doktorgrades der
Julius-Maximilians-Universität Würzburg

vorgelegt von Luis Maier
aus Moosburg a. d. Isar

Würzburg 2015

Eingereicht am: _____
bei der Fakultät für Physik und Astronomie

1. Gutachter: Prof. Dr. Hartmut Buhmann
2. Gutachter: Prof. Dr. Matthias Bode
3. Gutachter: _____
der Dissertation

Vorsitzende(r): _____

1. Prüfer: Prof. Dr. Hartmut Buhmann
2. Prüfer: Prof. Dr. Matthias Bode
3. Prüfer: _____
im Promotionskolloquium

Tag des Promotionskolloquiums: _____

Doktorurkunde ausgehändigt am: _____

CONTENTS

PUBLICATIONS

Parts of this thesis have already been published in the following papers:

- **L. Maier**, J. B. Oostinga, D. Knott, C. Brüne, P. Virtanen, G. Tkachov, E. M. Hankiewicz, C. Gould, H. Buhmann, and L. W. Molenkamp. Induced superconductivity in the three-dimensional topological insulator HgTe. *Phys. Rev. Lett.*, 109:186806, Nov 2012.

- J. B. Oostinga, **L. Maier**, P. Schüffelgen, D. Knott, C. Ames, C. Brüne, G. Tkachov, H. Buhmann, and L. W. Molenkamp. Josephson supercurrent through the topological surface states of strained bulk HgTe. *Phys. Rev. X*, 3:021007, May 2013

- **L. Maier**, E. Bocquillon, M. Grimm, J. Oostinga, C. Ames, C. Gould, C. Brune, H. Buhmann, L.W. Molenkamp, Phase-sensitive SQUIDs based on the 3D topological insulator HgTe. To be published in *Physica Scripta*

Further publications:

- J. Wiedenmann, E. Bocquillon, R. S. Deacon, S. Hartinger, T. M. Klapwijk, **L. Maier**, C. Ames, C. Brüne, K. Ishibashi, S. Tarucha, H. Buhmann, L. W. Molenkamp. Zero-energy Andreev bound states in a HgTe-based Topological Josephson Junction. Submitted to *Science*

- I. Sochnikov, **L. Maier**, C. A. Watson, J. R. Kirtley, C. Gould, G. Tkachov, E. M. Hankiewicz, C. Brüne, H. Buhmann, L. W. Molenkamp, and K. A. Moler. Nonsinusoidal current-phase relationship in Josephson junctions from the 3D topological insulator HgTe. Accepted for publication in *Phys. Rev. Lett.*

- H. Thierschmann, M. Henke, J. Knorr, **L. Maier**, C. Heyn, W. Hansen, H. Buhmann, and L. W. Molenkamp. Diffusion thermopower of a serial double quantum dot. *New Journal of Physics*, 15(12):123010, 2013

ACRONYMS

AC	alternating current
AR	Andreev reflection
BdG	Bogoliubov-de Gennes
CP	Cooper pair
DC	direct current
DI	deionized
DOS	density of states
EC	Eccosorb CRS-117
JJ	Josephson junction
MBE	molecular beam epitaxy
MF	Majorana fermion
N	normal conductor
PMMA	polymethyl methacrylate
QHE	quantum Hall effect
RCSJ	resistively and capacitively shunted junction
S	superconductor
SC	superconductivity
SdH	Shubnikov-de Haas
SEM	scanning electron microscope
SQUID	superconducting quantum interference device
TI	topological insulator
US	ultrasonic
ZMFA	zero magnetic field anomaly

1

INTRODUCTION

We'll have to think up bigger problems
if we want to keep them [computers] busy.

— Howard Hathaway Aiken [1]

Computation was an important driving force for the fast developments of the late 20th century [2] and is the defining feature of many common tasks, like information exchange via the internet and local data processing, e.g. word processing. In the scientific setting computers are used for automated data collection and handling as well as simulation of complex physical systems. Especially the latter can be one of those "bigger problems" mentioned in the quote at the top, which was said by Howard Aiken referring to electromechanical computers in the 1940ies. Even though computing power has increased by several orders of magnitude since then [3] and thus much more complex problems can be solved, there are still enough left that are too hard to be calculated. Some can be computed in parallel to be solvable in a reasonable time, which lead to the development of multicore central processing units (CPUs) and, a step further, general purpose computing on graphics processing units (GPUs), which consist not only of 2, 4 or 8 cores, but several thousands [4].

While all these ideas lead to a tremendous amount of computing power it is not nearly sufficient in some cases. One very prominent example is the factorization of big integer numbers into primes. This problem is believed to be superpolynomial on a classical computer, which means with bigger input numbers the time to factorize them grows faster than polynomial. In order to solve this problem it is useful to think about completely different types of computers to reduce the overall complexity of the issue

and not just to increase the speed of existing systems. It is believed that this factorization, upon other problems, can be solved faster with the use of a quantum computer. Those machines extend the information of a bit to the qunatum mechanical analog, a qubit, which is represented by a two state system. Due to its quantum nature the qubit allows for superpositions of the two states in each qubit as well as entanglement between neighboring qubits. These two properties constitute the main differences to a classical computer and enable the implementation of new types of algorithms, like Shor's algorithm in the case of prime factorization. [5]

However, the quantum information stored in the qubits has to be stable over time to be able to perform the calculations intended. The probability of decoherence in the system becomes bigger with environmental noise and as more qubits are introduced [6, 7]. In contrast to classical computers the quantum information can not just be cloned [8] in order to correct errors on a hardware basis. Other forms of quantum error correction are possible, but increase the amount of qubits and operations needed [9, 10]. Consequently effects of decoherence in the system have to be reduced to advance quantum computation from a scientific idea to a useful application.

Data storage with qubits has been realized in several systems, e.g. quantum dots [11], trapped ions [12] or nuclear magnetic resonance [13] only to name a few. In the latter it was even possible to apply Shor's algorithm to the number 15 to receive the factors 3 and 5 [13]. But all these systems have a serious problem with decoherence, when they are scaled to larger size. A possibility to avoid most types of decoherence is given in the subcategory of topological quantum computing. Here non-abelian anyons are used to encode the quantum information. In contrast to common particles like fermions or bosons, these types of quasiparticles are able to store the information non-locally and perform calculations by braiding, i.e. exchanging the particles. Thus common causes of decoherence based on local interaction, like electron-phonon or electron-electron interactions, are expected to have no influence on the qubit system [14].

One way to experimentally realize these non-abelian anyons was given by Fu and Kane in 2008. They suggested the use of a topological insulator in contact with a s-wave superconductor [15]. This interface should be able to host zero energy bound states so-called Majorana states, which obey non-abelian statistics and thus can be used for topological quantum computing. The goal of this thesis is to develop a fabrication process to produce these interfaces for the first time. Afterwards they are

studied in transport measurements to investigate, if any signatures proposed by Fu and Kane are appearing due to the usage of a topological insulator.

The first component of the interface, the topological insulator, is a newly discovered state of matter. This material is insulating in the bulk, but at the same time has conductive states at its surfaces [16, 17]. Its properties will be discussed in chapter 2 for the case of strained bulk HgTe. The second component, the s-wave superconductor, is already a well known system. After a short overview of the theoretical basics required for understanding superconducting devices the idea behind the combination of a topological insulator and a superconductor will be presented in chapter 3. Before moving on to the experimental results, the sample preparation and the equivalently important filtering and measurement systems will be described in chapter 4.

The concept as well as the measurements on superconductor/topological insulator/superconductor junctions is presented in chapter 5, which allows to test for the appearance of Majorana states. This is followed by superconducting quantum interference devices (SQUIDs) built from two of the above junctions to test for unusual phase relations between the superconducting leads in chapter 6. Finally the results will be recapped in an English as well as a German summary in chapter 7 and 8 respectively.

2

HGTE AS A 3D TOPOLOGICAL INSULATOR

The main motivation of this thesis is to detect signatures of Majorana fermions in the solid state context. It is expected, that one way of achieving this is the combination of a topological insulator (TI) and a superconductor (S) to mimic a $p_x + ip_y$ superconductor [15]. This type of S can then be gapped to generate a Majorana bound state [18]. This chapter will discuss the TI, which is the first part needed in the realization of these special states.

2.1 BAND STRUCTURE OF HGTE

Two requirements have to be met in order to form a TI: on the one hand the material must have a band inversion and on the other hand an insulating bulk. In Fig. 1 the band structure of bulk HgTe is shown. In contrast to the usual band ordering the Γ_6-band is below the heavy and light hole Γ_8-bands. HgTe already has an inverted band ordering.

The second requirement is not fulfilled. Looking at the Γ-point, the two Γ_8-bands are touching at the Fermi energy — HgTe is a semimetal. To circumvent this limitation one can introduce strain into the system to break the symmetry and to open a band gap.

The HgTe layers are grown on CdTe substrates along the [001]- or z-direction (see Fig. 2). Due to the underlaying CdTe lattice the HgTe is forced to adapt the lattice constant of CdTe in the (xy)-plane, which leads to tensile strain.

The strain in the (xy)-plane can be calculated by comparing the lattice constant of CdTe $a_{\mathrm{CdTe}} = 0.6481$ nm with the lattice constant of unstrained HgTe $a_{\mathrm{HgTe}} = 0.6461$ nm (both values taken from [20]). The resulting strain is then

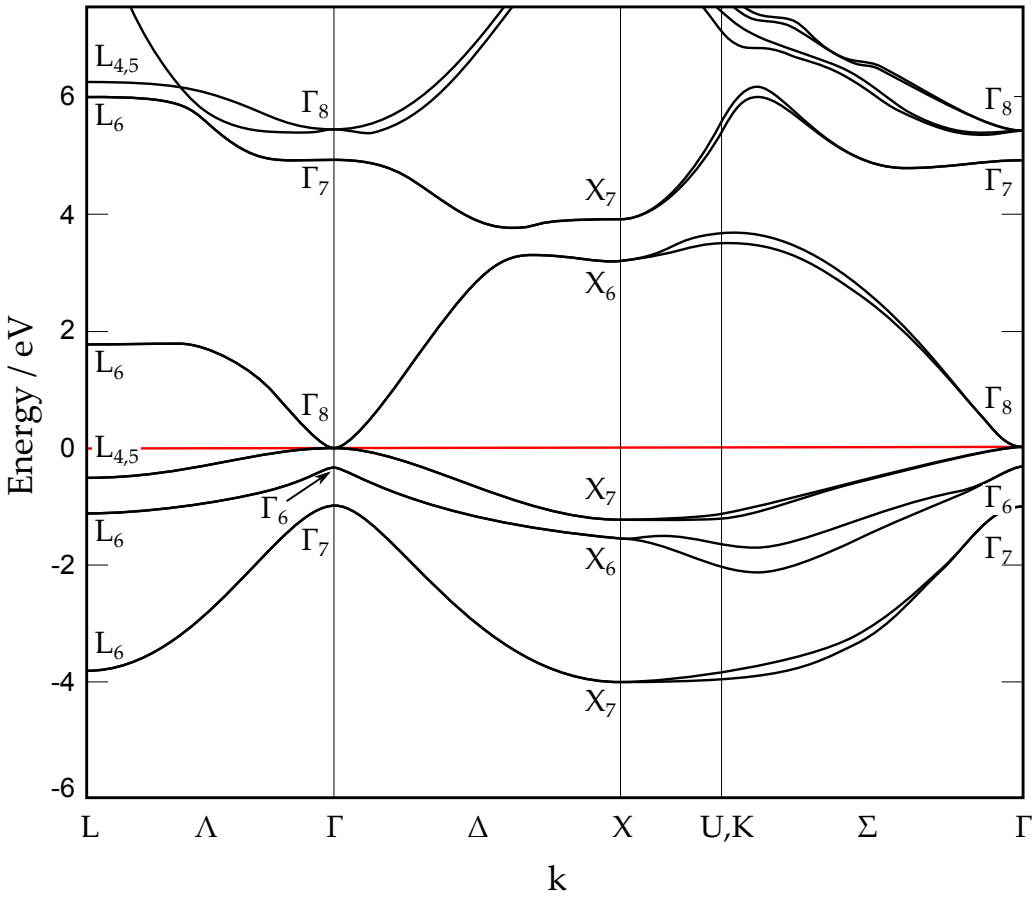

Figure 1: Band structure of HgTe. The Fermi energy is drawn as a red line. Redrawn after [19]

$$\epsilon = \epsilon_{xx} = \epsilon_{yy} = \frac{a_{CdTe} - a_{HgTe}}{a_{HgTe}} = 0.3\%. \tag{1}$$

To calculate the complete strain energy of this problem one also needs to know the strain in z-direction ϵ_{zz}. This component can be derived by looking at Hooke's law $\sigma = \underline{C}\epsilon$, which connects the stress σ to the strain ϵ via the elastic stiffness matrix $\underline{C}$, often also called Young's modulus. Written in Voigt notation and taking into account the cubic symmetry of the zinkblende structure of HgTe one obtains [21]

$$\begin{pmatrix} \sigma_{xx} \\ \sigma_{yy} \\ \sigma_{zz} \\ \sigma_4 \\ \sigma_5 \\ \sigma_6 \end{pmatrix} = \begin{pmatrix} C_{11} & C_{12} & C_{12} & & & \\ C_{12} & C_{11} & C_{12} & & & \\ C_{12} & C_{12} & C_{11} & & & \\ & & & C_{44} & & \\ & & & & C_{44} & \\ & & & & & C_{44} \end{pmatrix} \begin{pmatrix} \epsilon_{xx} \\ \epsilon_{yy} \\ \epsilon_{zz} \\ 2\epsilon_{23} \\ 2\epsilon_{13} \\ 3\epsilon_{12} \end{pmatrix}. \tag{2}$$

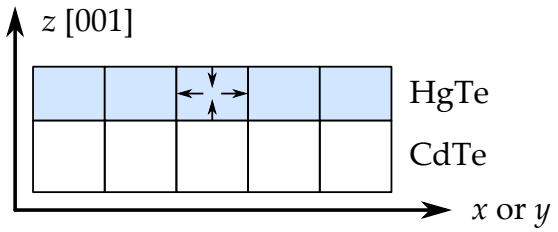

Figure 2: Symbolic representation of unit cells as rectangles at a HgTe/CdTe interface. The direction of strain in HgTe due to the growth on a CdTe substrate is shown as small arrows.

No stress is applied on the structure in z-direction $\sigma_{zz} = 0$ and thus, extracting the according equation from the matrix notation, one gets

$$C_{12}\epsilon_{xx} + C_{12}\epsilon_{yy} + C_{11}\epsilon_{zz} = 0. \tag{3}$$

Substituting the above mentioned $\epsilon_{xx} = \epsilon_{yy}$ the final form is

$$\epsilon_{zz} = -2\epsilon_{xx}\frac{C_{12}}{C_{11}}. \tag{4}$$

Now it is possible to calculate the size of the bandgap using

$$E_g = 2\,|b(\epsilon_{xx} - \epsilon_{zz})| = 2\epsilon\,|b(1 + 2C_{12}/C_{11})|\,, \tag{5}$$

taken from [22]. Where b = -1.5 eV [23] is the uniaxial deformation potential and the ratio of the stiffness constants amounts to $C_{12}/C_{11} = 0.683$ [24]. The resulting direct band gap at the Γ-point is $E_g = 21$ meV.

The ordering of the bands in unstrained HgTe around the Γ-point is shown in Fig. 3 a). Taking the calculated strain energy into account a band gap develops between the Γ_8 heavy hole and light hole bands [Fig. 3 b)] turning the semimetal HgTe into a semiconductor. As a consequence the system now suffices both prerequisites for a TI, a inverted band ordering and an insulating bulk.

2.2 SURFACE STATES

One of the most interesting features of a TI is the formation of surface states, which can be explained as follows: When looking at an interface between a TI, e.g. HgTe, and a normal insulator, e.g. CdTe, the inverted bands need to change places from one

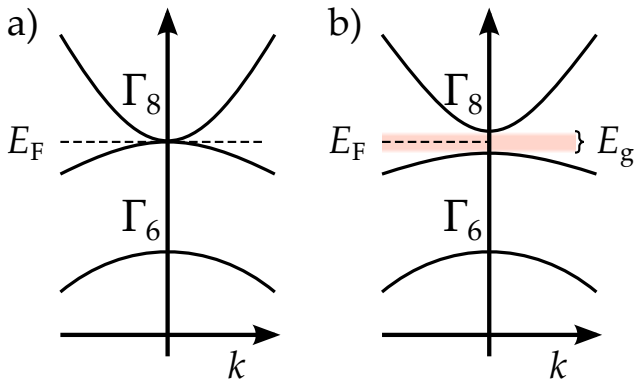

Figure 3: Band structure of unstrained a) and strained b) HgTe at the Γ-point.

material to the other (see Fig. 4). As long as the Fermi energy E_F lies in the band gap in both bulk materials there always has to be a crossing of E_F at the interface leading to conducting states at this position.

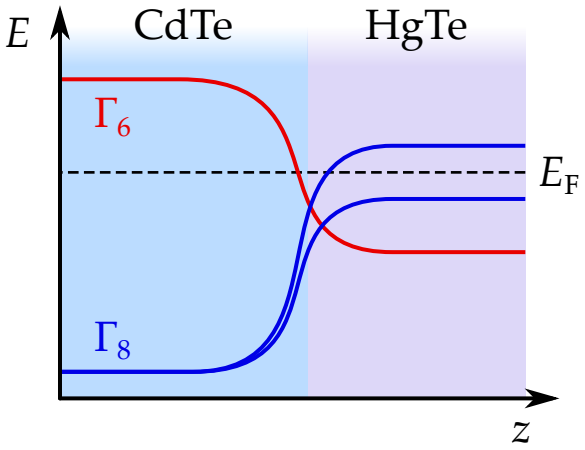

Figure 4: Sketch of the position-dependent band gap at a CdTe/HgTe interface.

One feature of these surface states is their linear dispersion relation [25] in contrast to the usual quadratic dispersion. The surface states can be described within the Dirac-Hamiltonian for massless fermions [26]

$$H_{\text{surface}} = -i\hbar v_F \boldsymbol{\sigma} \boldsymbol{\nabla}, \tag{6}$$

with the Fermi velocity v_F, the vector $\boldsymbol{\sigma} = (\sigma_x, \sigma_y)$ constructed from the Pauli spin matrices and the nabla operator $\boldsymbol{\nabla}$. Only the (xy)-plane of the interface is described with this Hamiltonian, which reduces the problem to two dimensions. This, for now, only describes part of the problem and other surfaces need to be added later to de-

scribe the compete system with all surfaces. By solving Eq. (6) one can extract the energy dispersion relation

$$E = \pm \hbar v_F \left| \boldsymbol{k} \right| , \tag{7}$$

which is clearly linear: $E \propto |\boldsymbol{k}|$. The energy dispersion resulting from H_{surface} is shown in Fig. 5 a). One can see that not only the energy dispersion is unusual, but also the spin texture is significantly different from a normal metal or semiconductor.

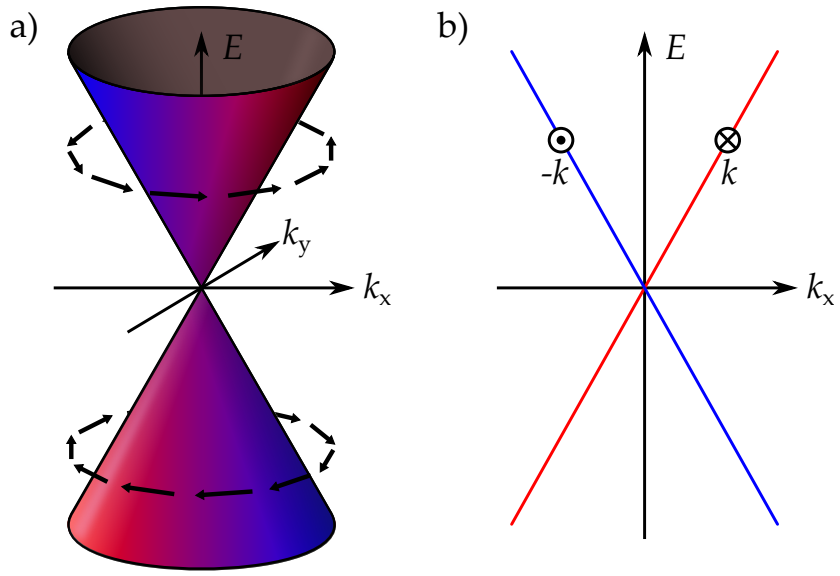

Figure 5: a) Dirac cone with sketched spin directions (indicated by coloring and arrows) b) Cut of the cone in the (E,k_x)-plane with two exemplary spin states at k and $-k$.

In contrast to most systems the spin is not doubly degenerate. Still, due to time reversal symmetry, for every state in the system with wavevector $\boldsymbol{k}$ there has to be a state at $-\boldsymbol{k}$ with opposite spin and equal energy. This leads to the spin situation sketched in the cut through the Dirac cone in Fig. 5 b). One can see that every state on the red branch has a partner in the blue branch that exactly fulfills this claim. If one then expands this into the two dimensions of momentum one gets a chiral spin polarization of the system as depicted by the arrows in Fig. 5 a).

Hence, it is important to understand which selection criteria were utilized to choose the materials used in the experiments. On the one hand the thickness of the HgTe layers has to be smaller than 160 nm [27]. Otherwise the crystal strain energy gets too big and relaxation processes start to set in. As a result the samples are no longer fully strained and the band gap decreases. On the other hand the layers must be thicker than roughly 40 nm [28] to ensure that the quantum mechanical confinement does not start

to play a dominant role and that the surface states on the top (HgTe/air) and bottom (HgTe/CdTe) interfaces [see Fig. 6 a)] do not start to overlap. The samples used in this thesis ranged from 66 nm to 76 nm and are thus well within the wanted range. The second important criterion is the dominance of the surface state conduction over bulk conduction, which can be verified by performing magneto-resistance measurements.

2.3 PROOF OF 2-DIMENSIONALITY

A good way to investigate the dimensionality of a system is to probe it for quantum Hall effect (QHE), which can only exist in a 2-dimensional system [29]. The most used geometry for this kind of measurements is a Hall bar, as depicted in Fig. 6 b). One records the current I and the longitudinal voltage V_{xx}, while varying the magnetic field B, to be able to extract the longitudinal resistance $R_{xx} = V_{xx}/I$. Oscillatory behavior in R_{xx} is often referred to as Shubnikov-de Haas (SdH) oscillations. Similarly one can measure the Hall resistance $R_{xy} = V_{xy}/I$.

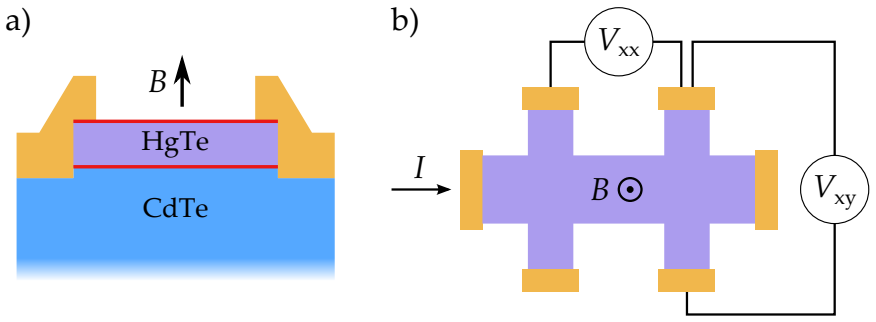

Figure 6: a) Sideview of the HgTe layer on CdTe substrate with contacts in orange. The red lines symbolize the two conducting layers assumed in the model. b) Top view of the Hall bar geometry with exemplary voltage probe setup.

When looking at a Hall bar of bulk HgTe the description of the surface states by Eq. (6) has to be expanded to the geometry at hand and has to include magnetic field dependence. To simplify the problem, the Hall bar is described as two parallel surfaces α (top and bottom), with spin σ, which are oriented perpendicular to the applied magnetic field $\boldsymbol{B}$. The surfaces are sketched as red lines in Fig. 6 a). The states of the system can then be noted as $|\alpha, \sigma\rangle$. The new Hamiltonian in this basis is then [30]

$$\underline{H}_{2D} = \hbar v_F \begin{pmatrix} k_x\sigma_y - k_y\sigma_x & 0 \\ 0 & -(k_x\sigma_y - k_y\sigma_x) \end{pmatrix}. \tag{8}$$

One can now introduce the magnetic field in z-direction by using a Peierls substitution and replacing $\boldsymbol{k}$ with $\boldsymbol{\pi} = \boldsymbol{k} + \frac{e}{\hbar}\boldsymbol{A}$, where $\boldsymbol{A} = (0,\, B_0 x,\, 0)$ describes the field $\boldsymbol{B} = B_0 \hat{\boldsymbol{z}}$. The resulting energy dispersion in magnetic field is given by

$$E_\alpha(n_\alpha) = \mathrm{sgn}(n_\alpha)\sqrt{2e\,|n_\alpha|\,\hbar v_\mathrm{F}^2 B_0} \qquad n_\alpha = 0, \pm 1, \pm 2, \ldots \tag{9}$$

with the Landau level index n_α. The resulting density of states (DOS) at finite magnetic field is sketched in Fig. 7, clearly showing the unusual Landau level position at zero energy, which would not be possible in a system with quadratic dispersion.

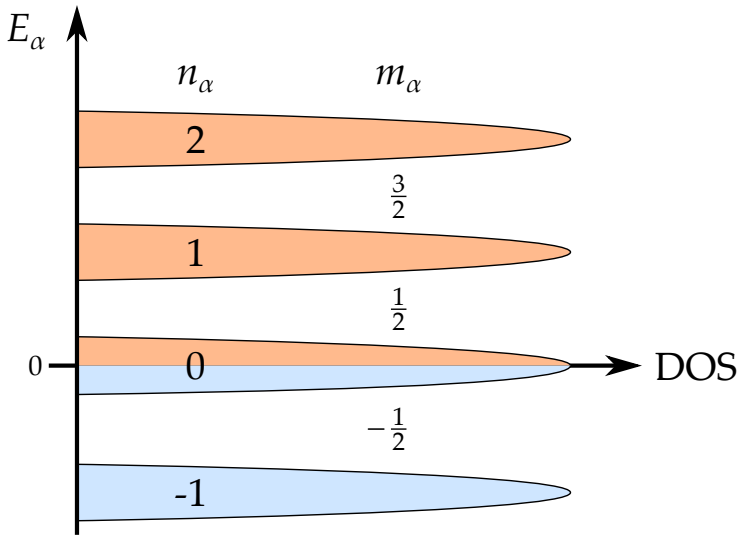

Figure 7: DOS of a single Dirac surface plotted against energy E_α at finite magnetic field. The Landau levels n_α are numbered in integers and the SdH minimum index is the half integer value between both neighboring Landau levels, $m_\alpha = (n_{\alpha,1} + n_{\alpha,2})/2$.

Comparable to the results on graphene systems [31], which have a degeneracy of four, a single surface as described by Eq. (6) only consists of one non degenerate Dirac valley and thus shows quantized conduction values of

$$\sigma_{\alpha,\mathrm{xy}} = m_\alpha \frac{e^2}{h} \qquad m_\alpha = \pm\frac{1}{2}, \pm\frac{3}{2}, \pm\frac{5}{2}, \ldots \tag{10}$$

between the Landau levels, with m_α being the SdH minimum index. One can also express m_α as half integer value between both neighboring Landau levels, $m_\alpha = (n_{\alpha,1} + n_{\alpha,2})/2$. Due to the values of m_α this is often referred to as *half integer* QHE.

To understand the how the of the Hall and SdH resistance develop from the single surface, described so far, to a more complete model one can look at the case of two symmetric surfaces with equal carrier densities and thus equal Fermi velocities v_F.

Due to the equal energy dispersions both surfaces would undergo the transition from one SdH minimum to the next at the same magnetic field value and equivalently the transition from one Hall plateau to the next happens in parallel with the resulting quantization of

$$\sigma_{\text{top, xy}} + \sigma_{\text{bottom, xy}} = 2m_{\text{sym}}\frac{e^2}{h} = N\frac{e^2}{h} \qquad N = 1, 3, 5, \ldots \tag{11}$$

only showing odd plateau values in the Hall resistance R_{xy}.

This however is not the case here as the top and bottom surface differ in their composition. The bottom layer is a CdTe/HgTe interface that is buried in the structure and thus much better protected against any form of contamination. The top layer is a HgTe/Air interface and exposed to different chemicals during sample processing as well as oxide from the atmosphere. Hence it is expected that the carrier densities of both surfaces are not equal and the transitions between the SdH minima and Hall plateaus do not happen at the same magnetic field value in top and bottom surface. The resulting Hall traces have to be considered as a superposition of two surfaces with different densities and plateaus only occur if both subsystems are simultaneously in a stable quantized configuration. In this case one could use $N = m_{\text{top}} + m_{\text{bottom}}$ and the resulting N would be integer, but has not to be an odd number. In the following discussion the two surface model will be applied to a Hall measurement.

Figure 8 a) shows R_{xx} and R_{xy} for a 70 nm thick HgTe sample in Hall bar geometry at $T = 4.2\,\text{K}$. The metallic contacts (golden areas) of the Hall bar are connected to the top and bottom surface simultaneously.

Both curves show some quantization features, but there are no clear plateaus visible in R_{xy}. If one would take the interval of smallest slope as plateau positions the values strongly deviate form the expected values. For comparison the fractions of the Klitzing constant $R_K = h/e^2$ [32] are included as dashed red lines. It appears as if an additional parallel conductance is present in the system, which does not show QHE.

This changes when reducing the temperature to 20 mK in Fig. 8 b). The plateaus nearly reach the expected value and a clear numbering is possible. The R_{xx} minima now develop much more clearly, when the system shows a plateau, which indicates that the parallel conductance present at 4.2 K has mostly vanished.

The plateau with $N = m_{\text{top}} + m_{\text{bottom}} = 3$, or short plateau 3, is well developed in R_{xy} and the SdH resistance shows a clear minimum. This happens because both surfaces enter this minimum simultaneously and thus R_{xy} also clearly quantizes. The

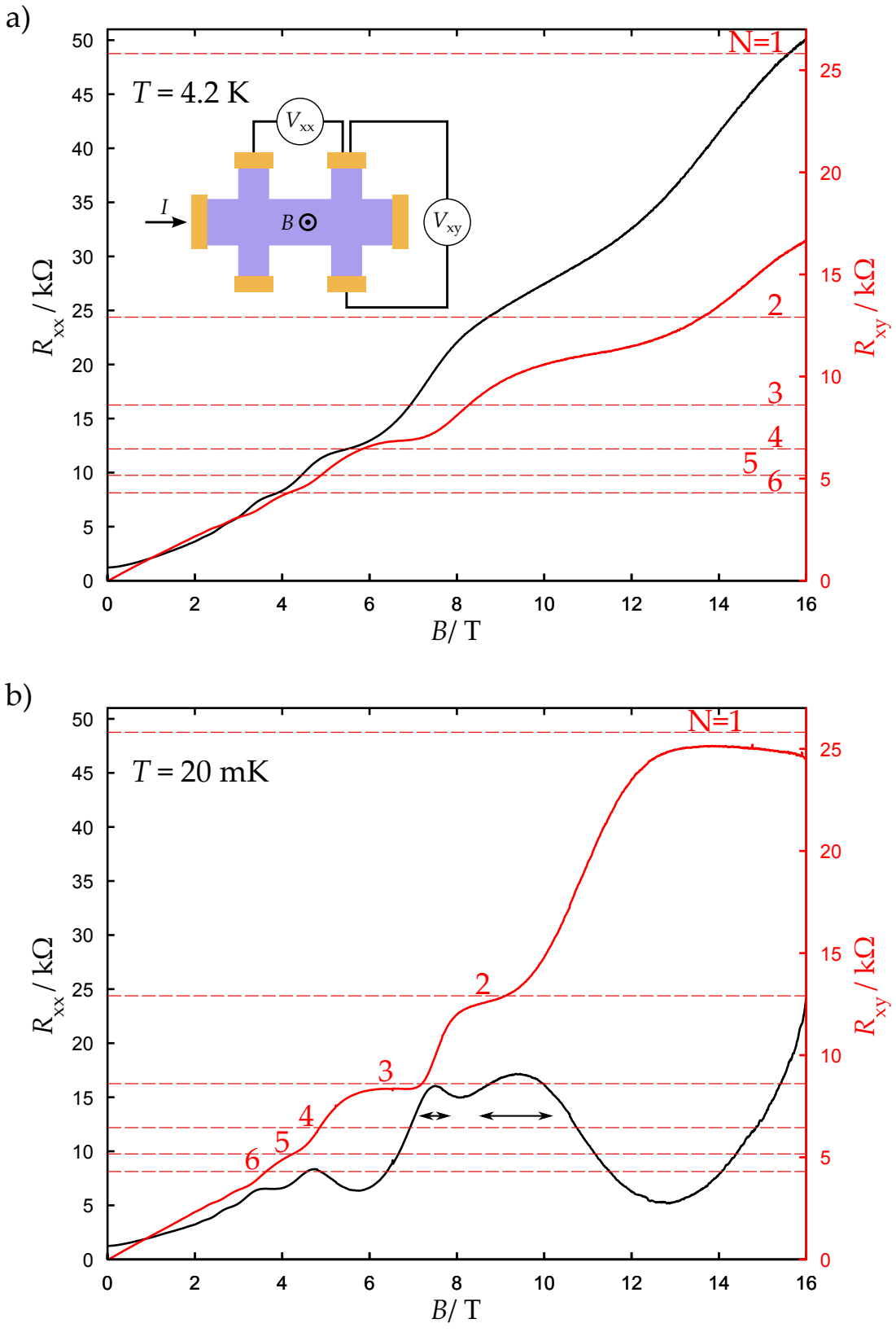

Figure 8: Magnetoelectric measurements of a 70 nm strained HgTe layer in Hall bar geometry at a) $T = 4.2\,\mathrm{K}$ and b) $T = 20\,\mathrm{mK}$. Both graphs are plotted with the same scale for better comparison. The red dashed lines show fractions of $\frac{h}{Ne^2}$.

deviation in R_{xy} from the ideal value could be attributed to a parallel conduction path. Possible options for this are a small residual bulk contribution or the mesa sides, oriented perpendicular to the magnetic field. Going to higher fields one can observe the transition to plateau 2, but before reaching a stable situation on this plateau the transition to plateau 1 already starts. This is also visible in the SdH resistance, where nearly no dip is observable.

Another indication of the different character of both surfaces is the broadening of the SdH oscillations. Looking at the transition from 3 to 2 one can see a much smaller broadening than for the transition from 2 to 1 [indicated by black arrows in Fig. 8 b)]. This hints to the first transition happening at the lower surface and the second, broadened transition happening at the dirtier top surface.

One can find, that the model only consisting of two surfaces can be applied to the measurements at $T = 20\,\mathrm{mK}$, although a lot of other influences have been neglected. Among these are, e. g., the conducting side surfaces parallel to the magnetic field $\boldsymbol{B}$ and the contribution of residual bulk conduction. Here only some basic properties of this systems have been shown. More information can be found in the papers of Brüne et al. [16, 28] and a very detailed analysis is given by the thesis of C. Thienel [33].

The contrast between 4.2 K and 20 mK has been shown, because, due to time constraints, not all material used in this thesis has been characterized at 20 mK. After having tested several strained HgTe structures at both temperatures and consistently getting the above mentioned result, a measurement comparable to the one shown in Fig. 8 a) at 4.2 K was enough to assume the sample will show clear surface conduction at 20 mK. After this introduction into strained bulk HgTe and its properties as 3-dimensional TI the basic properties of superconductivity need to be discussed before the exciting topic of interaction of TI and S is following.

3

INTRINSIC AND INDUCED SUPERCONDUCTIVITY

To understand why the phenomenon of superconductivity is interesting one should have a look at the basic properties of a Majorana fermion (MF). The common solution to the relativistic energy-momentum relation is the Dirac equation, which results in the concept of the Fermi sea and the postulation of particles and antiparticles [34]. A possible alternative solution is the interpretation of Ettore Majorana, which leads to the postulation of charge neutral particles which are their own antiparticles [35]. This type of particle has not been found yet, but there are suggestions to realize the properties of a MF as a quasiparticle state in solids [15, 36, 37]. In the following chapter the characteristics of superconductors will be presented and the prerequisites for the appearance of a Majorana state will be explored.

3.1 INTRINSIC SUPERCONDUCTIVITY

Shortly after the liquification of He was possible, transport experiments showed a very unusual behavior in some materials like Hg, Al and Pb. Below a critical temperature T_C the materials resistance drops to zero allowing for dissipationless transport. This phenomenon is now called superconductivity (SC) and was discovered by Kamerlingh-Onnes in 1913 [38].

As expected on temperature increase above T_C the superconductor (S) returns from the superconducting state back to the normal, resistive regime. But S can also be brought into the normal regime below T_C by applying a critical magnetic field intensity H_C or current I_C.

If S is brought into a magnetic field dissipationless currents are induced at the surface to hinder the penetration of magnetic flux into its volume. This is known as the Meissner effect and thus this state is called Meissner phase. Due to its response to

a magnetic field S can also be seen as perfect diamagnet [39]. The magnetic field is not instantly shielded at the surface, but has a penetration depth known as the London penetration depth λ_L. It is defined by the exponential decay of the magnetic field B_0

$$B(x) = B_0 \exp\left(-\frac{x}{\lambda_L}\right), \tag{12}$$

with x being the distance to the surface of S [40]. This will play a role when calculating the magnetic flux of an area enclosed by S, as the penetration of magnetic field into S leads to slightly bigger effective area.

S can be divided into two subgroups. Type I S loose their superconducting properties completely when exceeding H_C. They directly go from the Meissner phase into the metallic phase. In contrast to that, type II S experience the intermediate Shubnikov phase, where magnetic flux can enter S as flux tube in the magnetic field intensity range $H_{C_1} > H > H_{C_2}$. Those flux tubes only locally break SC and merely after H_{C_2} is reached the material is completely normal conducting. The superconductor used here is Nb, which is a type II material [41]. This however has no major consequences as most measurements are done in a range below 0.02 MA/m and the critical magnetic field intensity $H_{C_1} = 0.13$ MA/m [41], where Nb enters the Shubnikov phase, is well above.

So far only phenomenological aspects of S have been discussed. It is now time to have a look at the underlying microscopic BCS[1] theory. In 1956 Cooper presented the idea, that weakly, attractively interacting particles can form bound states and alter the DOS of the Fermi sea [42].

Considering the simplest case of two electrons in their lowest possible energy state, one can expect opposite momentum $\boldsymbol{k}$ and $-\boldsymbol{k}$ due to the total momentum being zero. Both particles interact with each other, but not with other electrons except by the Fermi exclusion principle. The wave function then takes the form [43]

$$\psi(\boldsymbol{r}_1 - \boldsymbol{r}_2) = \sum_{k>k_F} g_k e^{ik\boldsymbol{r}_1} e^{-ik\boldsymbol{r}_2}, \tag{13}$$

with weighting factors g_k. The total wave function has to be antisymmetric regarding electron exchange, which leads to two possible solutions: Either a spin singlet pairing[2] ($|\uparrow\downarrow\rangle - |\downarrow\uparrow\rangle$) with an antisymmetric function in position space or a triplet pairing ($|\uparrow\uparrow\rangle$, $|\downarrow\downarrow\rangle$, $|\uparrow\downarrow\rangle + |\downarrow\uparrow\rangle$) with the symmetric counterpart. Following the sym-

1 named after John Bardeen, Leon Neil Cooper and John Robert Schrieffer
2 $|\alpha\beta\rangle$ denoting the spin state of electron 1 and 2, with $\alpha, \beta = \uparrow$ (spin up) or $\downarrow$ (spin down)

metry of atomic orbitals the first type of S are referred to as s-wave S and the second type are called p-wave S [44].

As the force between the electrons is expected to be attractive the spin singlet, in most systems, has lower energy, due to the higher distribution probability of both electrons near each other. This leads to the singlet wave function with opposite spin given by

$$\psi\left(\boldsymbol{r}_1-\boldsymbol{r}_2\right)=\left\{\sum_{k>k_{\mathrm{F}}} g_k \cos\left[\boldsymbol{k}\left(\boldsymbol{r}_1-\boldsymbol{r}_2\right)\right]\right\}\left(|\uparrow\downarrow\rangle-|\downarrow\uparrow\rangle\right). \tag{14}$$

Using this equation one can solve the problem assuming the attractive potential V is only present inside the cut-off energy range $\hbar\omega_{\mathrm{C}}$ around the Fermi energy and zero otherwise. The size of $\hbar\omega_{\mathrm{C}}$ will become apparent later. Additionally utilizing the weak-coupling approximation $N(0)V \ll 1$, with the electrons DOS at zero temperature $N(0)$, the energy of the state is [43]

$$E \approx 2E_{\mathrm{F}} - 2\hbar\omega_{\mathrm{C}} e^{-2/N(0)V}. \tag{15}$$

It is clear from Eq. (15) that due to the small attractive interaction assumed here, there is a state for an electron pair with energy below $2E_{\mathrm{F}}$. Furthermore the electron pair has an energy smaller than the sum of two single electrons. Both electrons in the pair are time reversed, due to the opposite momentum and spin, and together with the interaction V form a Cooper pair (CP). The size of V also determines the superconducting band gap Δ, which is the main energy scale in S.

What is left to investigate is the nature of the attractive potential. It was found that the critical values (T_{C}, B_{C}) of S depend on the mass of the atoms used, which has been proven by looking at different isotopes of superconducting elements [45, 46]. This showed, that the potential V has to be based on the exchange of virtual phonons. As a result the energy range of the potential approximation $\hbar\omega_{\mathrm{C}}$ can be estimated with the cut-off energy of phonons in a crystal $\hbar\omega_{\mathrm{D}}$. Here ω_{D} is the Debye frequency.

To get a better feeling for the concept of CP it is interesting to look at its extent [47]

$$\xi = \frac{\hbar v_{\mathrm{F}}}{\pi\Delta} = 99\,\mathrm{nm}, \tag{16}$$

calculated for Nb, with the Fermi velocity $v_{\mathrm{F}} = 1.37 \cdot 10^6$ m/s [48] and superconducting band gap $\Delta = 2.9$ meV [49]. This means that, compared to the size of a typical lattice constant, CP occupy a larger volume and are thus strongly overlapping. Addi-

tionally the spins of both electrons are anti-parallel and as a result the total spin of CP is zero, leading to bosonic character. These properties allow to describe the ground state of S, the CP-condensate, by a single wave function

$$\Psi = \Psi_0 e^{i\phi_S} = \sqrt{n_{CP}} e^{i\phi_S}, \tag{17}$$

which only depends on the density of CPs n_{CP} and the macroscopic phase of the superconductor ϕ_S [50].

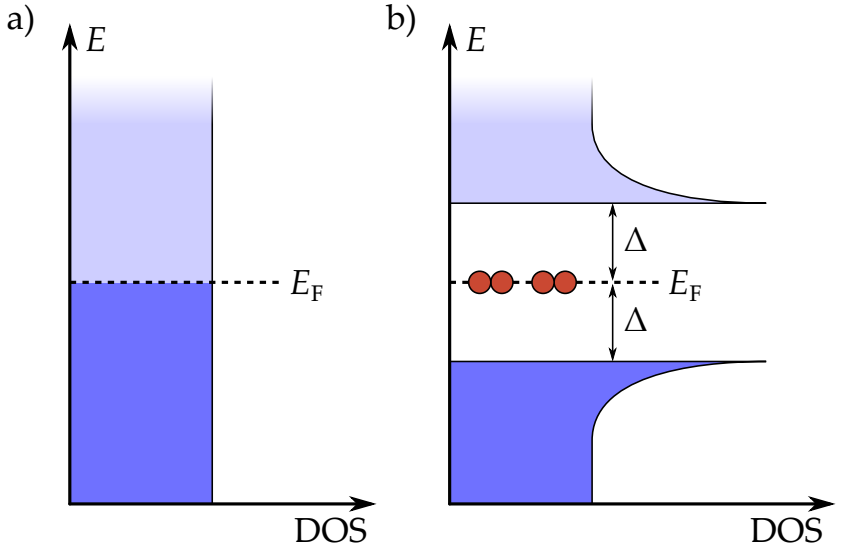

Figure 9: a) DOS of a normal metal b) DOS of a S with cooper pairs (red) in the band gap of 2Δ.

The creation of CP also has consequences for the DOS. In a normal conducting metallic system at zero temperature the DOS is continuous and filled up to the Fermi energy [see Fig. 9 a)]. If the metal becomes superconducting a band gap of 2Δ is introduced to the system [see Fig. 9 b)]. This gap can also be considered as the binding energy of a cooper pair, because it has to be overcome by magnetic field or temperature to split up CP . Because of this gap CP can not scatter with other particles and thus can conduct dissipationless. One can also see that the DOS at the band edges is strongly increased and decreases back to the DOS of the normal metal far from the gap [43].

To describe the ground state in BCS theory the concept of quasiparticles is introduced. These quasiparticles are described as superposition of hole-like and electron-like excitations. The quasiparticle operators for creation and annihilation are [43]

$$\gamma^\dagger = u^* c_\uparrow + v c_\downarrow^\dagger \tag{18}$$

$$\gamma = uc_{\uparrow}^{\dagger} + v^{*}c_{\downarrow}, \tag{19}$$

which are based on the creation $c_{\alpha}^{\dagger}$ and annihilation c_{α} operators of electrons, with spin $\alpha = \uparrow$ or $\downarrow$. The values u and v denote the statistical probability of being in a hole-like or electron-like state. The state is normalized by demanding $|u|^2 + |v|^2 = 1$. The energy dependence of u and v is given as

$$|v|^2 = 1 - |u|^2 = \frac{1}{2}\left(1 - \frac{\epsilon}{\sqrt{\Delta^2 + \epsilon^2}}\right), \tag{20}$$

with the relative energy difference of the quasiparticle and the chemical potential $\epsilon = E - \mu$ or at $T = 0$ to the Fermi energy E_{F}. For values much higher then the chemical potential $\epsilon \gg \mu$ Eq. (20) gives $|u|^2 = 1$, a state solely consisting of an electron. This is also visible in Eqs. (18) and (19), which reduce to the pure electronic excitation. Similarly for $\epsilon \ll \mu$, the same is true for holes. The interesting area is close to the chemical potential where $\epsilon \approx \mu$, here the electron and hole states coexist $|v|^2 \approx |u|^2 \approx \frac{1}{2}$.

Another interesting property, due to this description of a S, can directly be seen in Eqs. (18) and (19), which can be converted into one another by conjugate transpose. This operation also inverts the energy of the state $\epsilon \to -\epsilon$, leading to

$$\gamma(\epsilon) = \gamma^{\dagger}(-\epsilon). \tag{21}$$

This is known as electron-hole symmetry [18] and can be related back to the introduction of this chapter: the Majorana fermion (MF). They are expected to be their own antiparticle, which is fulfilled in S for the zero energy mode $\epsilon = 0$. This state however can not exist in s-wave S due to the violation of Pauli's principle [51].

Other systems have to be explored in order to realize the Majorana mode. So far the spin singlet pairing in s-wave S was investigated. It has not explicitly been shown, but this type of Ss has a momentum $\boldsymbol{k}$ independent band gap: $\Delta(\boldsymbol{k}) = \Delta$. In unconventional S this is no longer the case and the size of the band gap can vary with momentum direction.

One instance where MF can emerge is in p-wave or $p_x + ip_y$ S. The name is used because of the symmetry of the $\boldsymbol{k}$-dependent superconducting band gap. These S are in a triplet state with parallel spin and as a result the spin does not need to be explicitly included in the description below, thus the alternative name of a spinless S. In

this type of superconductors the states are not degenerate in spin and thus do break time reversal symmetry. They can be described by the Bogoliubov-de Gennes (BdG) Hamiltonian [52]

$$H_{\text{p-wave}} = \begin{pmatrix} \epsilon_p & \Delta\left(p_x + ip_y\right) \\ \Delta^*\left(p_x - ip_y\right) & -\epsilon_p \end{pmatrix}, \tag{22}$$

again with relative difference between the energy and the chemical potential $\epsilon_p = E_p - \mu$. The states of this Hamiltonian can be denoted as a two component vector $\Psi = \left(c\,, c^\dagger\right)^{\mathrm{T}}$, called Nambu basis. In the spinless case the zero energy state is possible and fulfills the claim of a Majorana mode:

$$\gamma(\epsilon = 0) = \gamma^\dagger(\epsilon = 0). \tag{23}$$

Several experiments on Sr_2RuO_4 suggest a p-wave pairing in this material [53]. It could be directly used for the purpose of creating Majorana modes, but this system is extremely sensitive to disorder [54]. As a result, even if one could detect MF in this systems the next step of storing them long enough to be able to do calculations with them appears very unlikely.

An alternative route was proposed by Fu and Kane [15]. They suggested to use a s-wave S-TI interface to create an environment capable of hosting MFs. In order to understand this concept one first needs to discuss how superconductivity can be induced in non superconducting materials.

3.2 INDUCED SUPERCONDUCTIVITY

As many other physical properties SC does not suddenly vanish at an interface between normal conductor (N) and superconductor (S). The next paragraphs will describe the behavior of quasiparticles and CP at such an interface.

Let us consider a N/S interface as shown in Fig 10 a). An electron has the energy ϵ relative to the Fermi energy, which is smaller than the superconducting band gap Δ. Coming from N it reaches S and can not be transmitted as there are no free states. The only process possible is the reflection of the electron. If one however takes higher order processes into account the electron can couple to an electron with energy $-\epsilon$ below the Fermi energy and form CP, which then can enter S. This process can equivalently

be described as an incident electron getting retroreflected as a hole with opposite momentum, while creating CP. This sequence can also happen in reverse order: CP gets annihilated, while absorbing a hole and creating an electron. This process was described by A. F. Andreev [55] and is now known as Andreev reflection (AR).

The most interesting part of these conversion processes is that both particles, electron and hole, get correlated in N — the hole will trace back the incident path of the electron and as a result the particles appear as a linked pair.

To estimate the range of this particle correlation one has to take a closer look at the process. The concept that both particles have identical momentum is only true for $\epsilon = 0$ at E_F, also referred to as perfect Andreev reflection [see Fig. 10 b)]. A small energy $\epsilon > 0$ leads to a slight difference in momentum of the electron $k_e = k_F + q$ and for the hole $k_h = k_F - q$, with the Fermi wavevector k_F [see Fig. 10 c)]. The difference in momentum perpendicular to the N/S surface is then [56]

$$\delta k = 2q = k_F \frac{\epsilon}{E_F}. \tag{24}$$

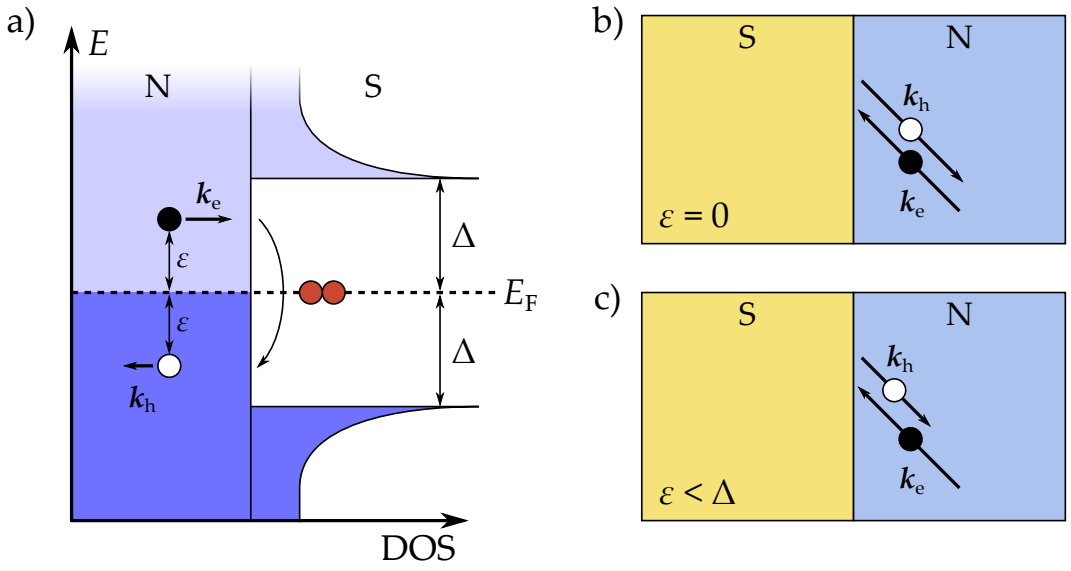

Figure 10: a) DOS at an interface of normal conductor (N) and superconductor (S) with sketch of Andreev reflection (AR) b) perfect AR at $\epsilon = 0$ plotted in real space c) AR with $\epsilon > 0$, visualizing the difference in momentum.

Due to the difference δk the phase of both particles increases monotonically and consequently one can define the energy-dependent coherent length [56]

$$L_\epsilon = \sqrt{\frac{\hbar D}{\epsilon}}, \tag{25}$$

with the diffusion coefficient D of the normal conductor. L_ϵ denotes the average distance at which both particles loose coherence and no longer retrace the path of the corresponding particle. This dephasing process is sketched in Fig. 11. The coherence length described by Eq. (25) is energy dependent and increases as ϵ approaches to zero energy. At $\epsilon = 0$ the L_ϵ would be infinite, but the process is additionally limited by the phase coherence length L_ϕ of the single electron or hole.

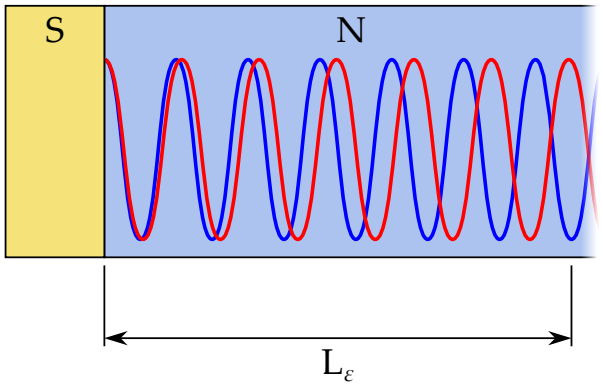

Figure 11: Dephasing of electron and hole at S/N interface (adapted after [56])

By inverting Eq. (25) one can express the distance dependance as

$$\epsilon_{\mathrm{Th}} = \frac{\hbar D}{L^2} \tag{26}$$

where ϵ_{Th} is the Thouless energy. This means, that at a distance L from the interface only electrons with an energy smaller than ϵ_{Th} are still correlated in pairs [56].

The pairing in N automatically has to lead to a reduction of unpaired quasiparticles and can be seen as an introduction of a superconducting gap in the normal metal. This is e.g. visible in tunnelspectroscopy experiments [57], where the closing of the induced gap with increasing distance to S has been shown as described by Eq. (26). A qualitative analysis of the probability of AR versus normal reflection at a N/S interface including limited interface transparency will be given in section 5.3 on page 58. It has been shown that S in contact to N can introduce a band gap. The next step is to understand what effect an induced gap can have in a TI.

3.3 TOPOLOGICAL SUPERCONDUCTIVITY

As mentioned before, Fu and Kane proposed to generate the environment needed for a Majorana fermion by combining a TI and a normal s-wave S [15]. To make a

comparison to a p-wave S [see Eq. (22)] one can have a look at the Hamiltonian of a TI with induced superconductivity [18]

$$\underline{H}_{\mathrm{TS}} = \begin{pmatrix} \underline{H}_0 & \underline{\Delta} \\ \underline{\Delta}^* & -\underline{\sigma}_{\mathrm{y}}\underline{H}_0^*\underline{\sigma}_{\mathrm{y}} \end{pmatrix}. \tag{27}$$

It is given in Nambu notation as before $\Psi = (c_\downarrow, c_\uparrow, c_\downarrow^\dagger, c_\uparrow^\dagger)^{\mathrm{T}}$, but because this is no longer a spinless system the vector has to be extended to four components. At the same time the matrix of the Hamiltonian $\underline{H}_{\mathrm{TS}}$ is extended to 4x4 and consists of the 2x2 sub matrices $\underline{H}_0$ and its time reversed counterpart $-\underline{\sigma}_{\mathrm{y}}\underline{H}_0^*\underline{\sigma}_{\mathrm{y}}$. These matrices describe the surface states of the TI as given by the Dirac Hamiltonian in Eq. (6). The off-diagonal elements $\underline{\Delta}$ and $\underline{\Delta}^*$ describe the induced s-wave superconducting coupling, i.e. they couple up and down spins and do not show any angular dependencies as seen in the case of a p-wave S before. The interesting relation between the p-wave S and the induced superconductivity in the surface state of a TI is that even though the two systems have a different Hamiltonian they both are expected to be able to host Majorana states [15]. By using the S/TI system it is expected that the problem of impurity sensitivity in Sr_2RuO_4 is not important as the states are topologically protected. The goal of this thesis is to realize and study the idea of induced superconductivity in the surface state of a topological insulator.

4

PREPARATIVE WORK

After discussing the basic concepts of TIs (Ch. 2) and SC (Ch. 3) the focus will now be shifted towards the actual realization of the experiments. First the sample fabrication will be covered and then the special requirements regarding superconducting measurements are presented, namely noise filtering and adapted transport setups.

4.1 SAMPLE FABRICATION

The used heterostructures were grown in a molecular beam epitaxy (MBE)-system. Starting from a substrate made of crystalline CdTe, an additional layer of CdTe is grown on top in-situ to achieve the best possible quality of the substrate surface. Because of the differences in growth temperature of CdTe and HgTe it is not possible to grow a HgTe layer until the substrate has been cooled down. Only then the functional layer can be grown (Fig. 12 left). This means the CdTe/HgTe interface is exposed to the chamber environment for quite some time and unwanted impurities can collect at the interface. Due to the high HgTe partial pressure during the growth, compared to those of the contaminants, it is not possible to estimate the impurity density of the interface. Additionally the top surface is exposed to atmosphere after the wafer leaves the MBE chamber. Both these factors are reducing the resulting mobility.

To circumvent this problem HgCdTe spacers have been introduced. In contrast to the first type of heterostructure this gives the possibility to continuously grow the layers without a break and the upper HgCdTe layer acts as a protection against oxidization and contamination of the upper HgTe/HgCdTe interface after the heterostructure leaves the MBE-chamber (Fig. 12 right). The second type of heterostructure is referred to as capped HgTe in contrast to uncapped HgTe in the first case. Even though the mobilities of the capped HgTe are higher, the lithographic treatment of those structures is

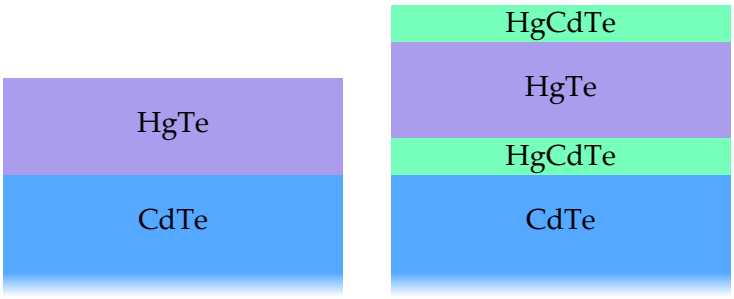

Figure 12: Typical heterostructures. Left: only a layer of HgTe is grown. Right: the HgTe layer has a HgCdTe spacer on the bottom as well as a cap on the top.

more difficult, because, in contrast to uncapped HgTe, the top HgCdTe layer needs to be properly removed before being able to produce a transparent contact to the HgTe layer.

The next steps sketch the preparation of a sample from an uncapped HgTe layer. The differences compared to capped HgTe will be discussed later. The detailed recipe is listed in Appendix B.2.

The grown heterostructure is first cleaved to adequate size for a single sample. While being handled in the MBE system the samples are glued onto a carrier using In. Before starting with the functional sample it is necessary to make sure that superconducting In-residues are removed, because they could distort applied fields or even worse trap magnetic flux. This is accomplished by etching in HCl solution while the front of the sample is protected with a wax layer.

It is now possible to define the conducting area, often also called mesa[1], with the help of a Ti etch mask and dry etching the unwanted HgTe in an Ar plasma [see Fig. 13 a)]. After the removal of the etch shield in the next, most important step the S-TI interface is fabricated.

When depositing the S, in our case Nb, on the sample one wants to produce a high transparent interface between the TI and the S to ensure a high probability of Andreev reflection [58]. To achieve this goal one deposits a polymethyl methacrylate (PMMA) etch mask. The area of superconducting contacts is exposed via e-beam lithography and afterwards the PMMA layer is locally dissolved in a development process. This exposes the contact area for further treatment. The oxide layer on top of the HgTe is removed with a short dry etching process. Here one needs to find the balance between etching long enough to remove all residues on top of the HgTe layer and

1 Named after the hill formation, which is, just as the lithographically defined mesa, an elevation with a flat top.

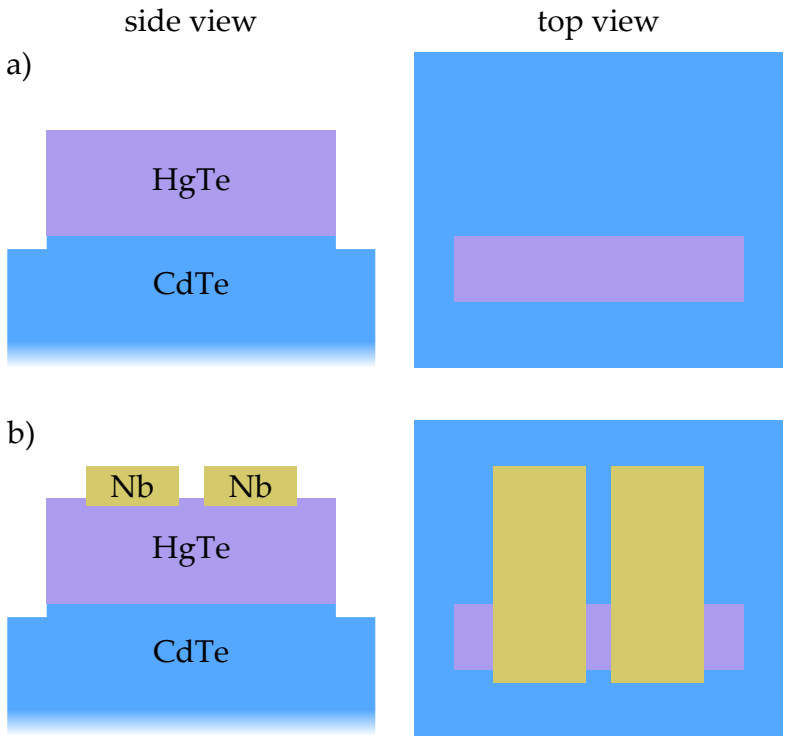

Figure 13: a) HgTe stripe after dry etching and etch mask removal b) finished Nb layer after interface cleaning and sputtering

etching short enough to not damage the PMMA layer too strong to no longer be able to perform a clean lift-off[2]. After the cleaning process the sample is transferred to the sputtering chamber as fast as possible. Ideally the sample should be kept in vacuum, but this is not possible due to the used equipment. Before inserting the sample into the main chamber the Nb target is cleaned by sputtering, ensuring the removal of unwanted contaminants on the source material as well as the best possible pressure in the chamber. Thin layers of evaporated Nb react with residual gases in the chamber and reduce the overall pressure [59]. This is often referred to as getter properties and is more commonly known for Ti, which is used in Ti sublimation pumps. In the next step Nb is sputtered onto the sample to produce the S-TI interface. To protect the Nb layer from oxidation two thin layers of Al and Ru are sputtered. To ensure a sufficient coverage of the mesa side surface the material is sputtered at an angle of $\gamma = 20°$ with respect to the surface normal (see Fig. 14 lower left). After the lift-off one obtains the situation sketched in Fig. 13 b).

The procedure for capped HgTe layers is the same, except for the etching process. The etch time needs to be adjusted to cut through the complete HgCdTe layer on the top which is normally 5 nm thick. This gives problems with the used PMMA, because

2 Process of removing the unwanted metal deposited on top of the resist layer by solving the resist.

the damage done during the etch process [60] leads to a very poor lift-off performance. One needs to use ultrasonic and still the yield of working structures is reduced. For HgCdTe layers bigger than 5 nm this process is not usable at all. To be able to work with thicker cap layers a different more etch resistant type of resist shield needs to be developed in the future.

The resulting Nb layers, colored in orange, can be seen in the scanning electron microscope (SEM) pictures of Fig. 14. The orientation of the sputter angle $\gamma = 20°$ is shown in the lower left picture and is indicated in all four pictures by the red arrows. Looking at the topview of both samples one can see that more material is deposited on the lower edge and less on the upper edge of the Nb layer. Sputtering is not a very directional process, due to the high gas pressure in the chamber and the big source material area, still the angling of the sample has the desired result of depositing more material on one side. This enables sufficient coverage of the mesa side surfaces to ensure a stable superconducting layer.

When comparing the quality of the Nb layer deposited on uncapped HgTe with an etch time of 6 s and capped HgTe with 12 s one can clearly see the increase of material deposition at the edges of the Nb layers as unwanted sidewalls. In the case of the capped sample the sidewalls are close to the PMMA thickness of 110 nm. Hence the lift-off quality is strongly reduced.

To finish the sample it is necessary to deposit metallic contacts to be able to later bond[3] the sample after it is glued into the chip carrier[4]. After the Nb layer is deposited these samples should always be stored in a nitrogen atmosphere to prevent any further oxidization. Nevertheless samples need several months of exposure to air, before they deteriorate, meaning the Nb no longer gets superconducting. The storage in nitrogen is therefore recommended, but not absolutely necessary. But not only a clean sample is required, but one also needs to carefully prepare the measurement environment as seen below.

4.2 FILTERING SYSTEM

To get a feeling for the energy scale of induced superconductivity in this samples let us consider two typical values: the critical current is in the range of 5 µA and the

3 Bonding describes a way of connecting the metal contacts on the sample to a standardized chip carrier via gold wires.

4 The chip carrier is a ceramic sample carrier with multiple contacts. This standardized contact layout can then be easily mounted in the measurement stations.

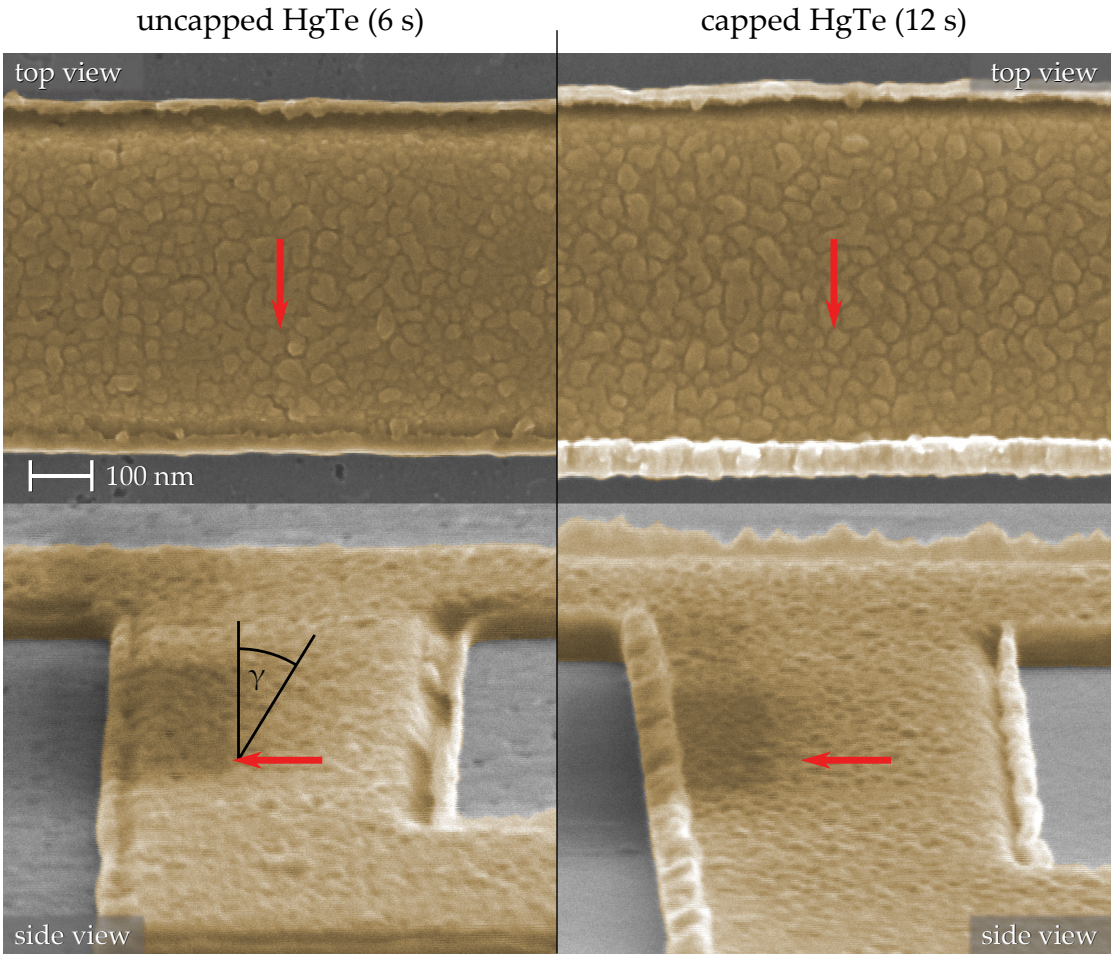

Figure 14: SEM image of Nb layers (colored in orange) on mesa. Left: uncapped HgTe with an Ar etch time of 6 s. Right: capped HgTe which needs to be etched for at least 12 s. The sidewall formation is much more dominant.

critical voltage is 150 µV. To be able to properly resolve this values one needs to be well below these with all other energy scales.

The first aspect that comes to mind is temperature. A pumped ^{4}He cryostat can reach the energy scale of $E_{\mathrm{Th}}(1.7\,\mathrm{K}) = k_{\mathrm{B}}T = 146\,\mu\mathrm{eV}$. This could be enough to see an onset of induced superconductivity, but is not enough to properly resolve it. For this one needs a ^{3}He cryostat or a ^{3}He/^{4}He dilution refrigerator. The measurements in this thesis were mostly carried out in the latter and it could reach a base temperature of 25 mK giving $E_{\mathrm{Th}}(25\,\mathrm{mK}) = 2\,\mu\mathrm{eV}$. The functionality of a dilution refrigerator will not be described here and can be e.g. found in ref. [61].

Additional to thermal noise one needs to take into account electrical noise. At low temperatures the interaction of lattice phonons and electrons gets very small [62]. This means that even though the lattice is cooled to the above mentioned 25 mK the electrons can have a much higher temperature. To deal with this situation a low noise

environment needs to deal with electromagnetic noise, which is mainly introduced through the cable connections. The wiring and filtering setup used for the measurements was adapted from Ref. [63] and will now be described in detail going from room temperature down to the coldest point. An overview is given in Fig. 15.

The connections at room temperature have to be done with special care, as the wiring is not already shielded by the Faraday cage of the metallic cryostat. The connection cable[5] (see black cable on top in Fig. 15) is not only shielded as a whole, but every wire has its own shield to minimize crosstalk. The cable is connected to a aluminum box, which houses switches as well as the first filter stage.

The used switches[6] employ the so called make-before-break mechanic: When switching from contact A to the contact B the switch first shorts the two contacts before disconnecting A. This ensures that at no time the wire is at an undefined potential and due to the mechanical realization also suppresses contact chatter. The switching happens between the three states: connected through the filter, connected to ground and not connected or floating. Especially the last state is different to the usual setup as the floating connection is inside the aluminum box and not exposed to the lab environment.

Before entering the cryostat each wire is individually passed through a Mini-Circuits PLP 1.9+[7] low-pass filter with a cutoff frequency of 1.9 MHz. These filters are of a considerable size (20 mm · 10 mm · 10 mm) and can not be fitted inside the cryostat.

The measurement wiring from this point going down consists of two sets of 24 twisted pair copper wires, one for each mounted sample, which are embedded in a loom for easier handling. Only 18 of those 24 wires are used for measurements.

The next filtering stage is in the cryostat and runs from room temperature at the top of the cryostat to the 1 K pot with a temperature of 1.7 K. Materials used in this context need to be able to sustain thermal cycling and the thermal gradient. Furthermore the wires need to run inside a slim metal tube, which limits the available space. To be able to construct a filter here Eccosorb CRS-117 (EC)[8] was used. The material is described as magnetically loaded, but the exact composition not disclosed by the manufacturer. It acts as as low-pass filter with a cutoff frequency of 1 GHz when in proximity to wiring. EC is a two component material, which is liquid after mixing and becomes a flexible material after drying for one day. To fit a filter in the afore mentioned space

5 Belden 8170 CM 10PR24 shielded (ul) E108998 or AWM 2493
6 ELMA, Drehschalter 07R1x4k horiz. ZB WD (Art.Nr. 07R1423-30000)
7 Mini-Circuits, Low-Pass filter PLP-1.9+ Rev. A
8 Emerson & Cuming MWP, Eccosorb CRS-117

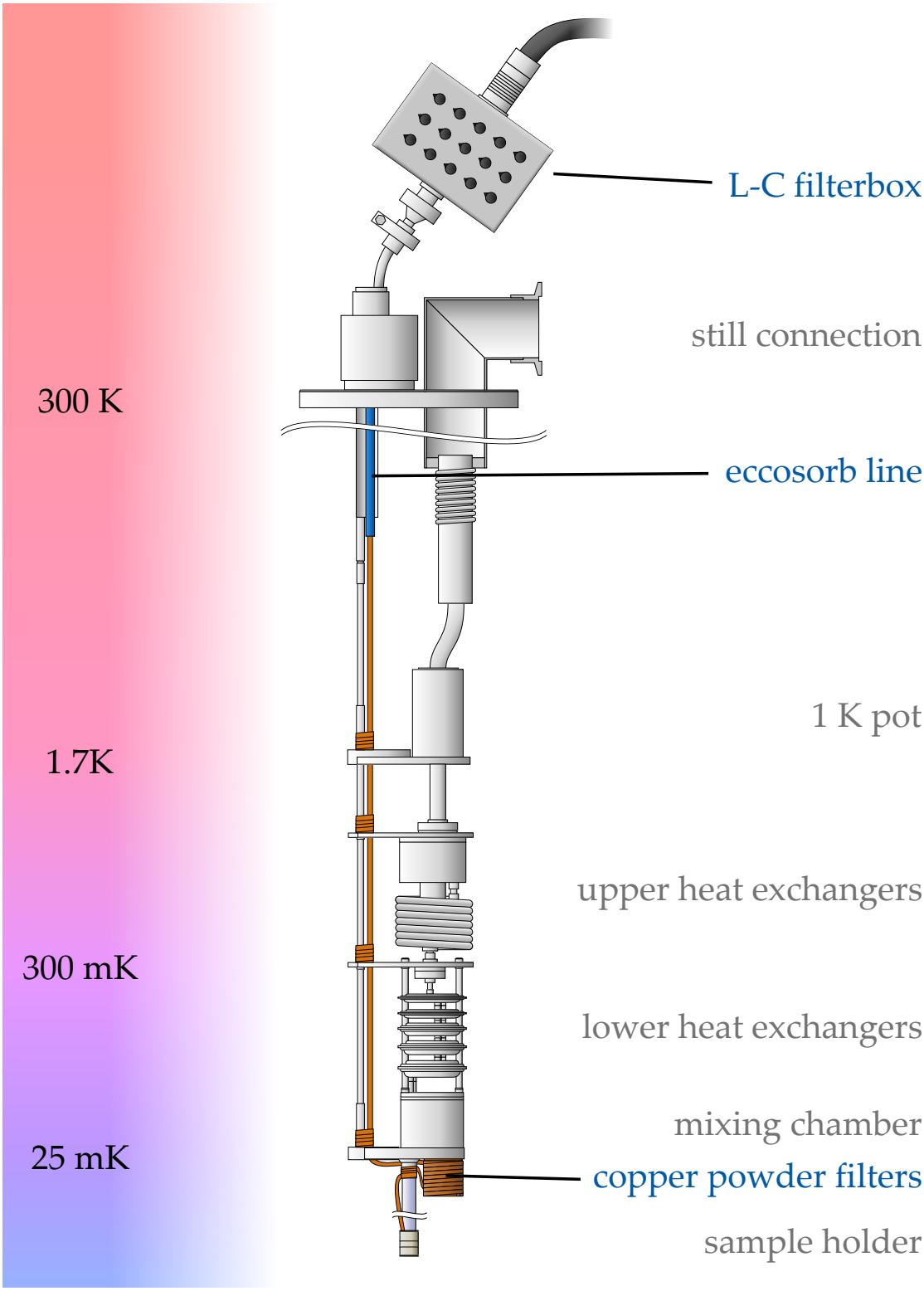

Figure 15: $^{3}He/^{4}He$ dilution refrigerator with colored temperature zones. Additional installed filters are written in blue. The cables inside the cryostat are a 24-wire twisted pair loom (orange) which are made from copper (300 K to 1.7 K and below mixing chamber) and the superconductor NbTi (1.7 K up to mixing chamber).

the wiring is first guided through a PVC hose, which is then filled with EC. After drying the PVC hose, including the wiring, can be inserted into the metal tube (see Fig. 15).

At the 1 K pot the wiring material changes to superconducting NbTi. Because of the properties of the material the thermal conduction is strongly suppressed [64] helping to decouple the different thermal stages. While the wiring continues downwards it is thermally anchored at every temperature stage to only allow the smallest amount of heat possible to propagate to the mixing chamber and the sample.

At the mixing chamber the lowest temperature of roughly 25 mK is reached. Here materials with high thermal conductivity are used to ensure a good thermal coupling to the sample and thus the best possible cooling. Hence the wiring below the mixing chamber is made from copper.

At this lowest temperature stage the wiring is filtered with a copper powder filter. As each grain of the powder has a thin oxide layer they are all insulated from each other forming a enormous surface area. The skin effect then leads to strong attenuation in the GHz range [65]. When building the filter the copper powder is mixed with the epoxy Stycast 1266 to ensure easy and clean usability after drying. The epoxy does not interfere with the attenuation properties.

Figure 16: copper powder filters in version 1 (left) with R-C-filtering and version 2 (right)

The first filter (version 1) built with this technique can be seen on the left side in Fig. 16. It is completely encased in a copper box to protect the wiring and ensure good thermal coupling to the mixing chamber when mounted. After the powder based filters the wires are connected to a PCB[9]. The board, which carries R-C-filters, is built from SMD[10] parts to be able to fit two times 18 lines in the small space available. Here

9 printed circuit board. Insulating board with printed connections for electrical components.
10 surface mounted device. Instead of wires guided through the soldering joint (THT) these devices are soldered directly on the PCB-surface. This type of mounting needs less space.

the very low cutoff frequency of 10 kHz was chosen to filter as much extra noise as possible. Because the cryostat is also used for higher resistance measurements and a manufacturing error the R-C-filters were only used once and then removed later. A second concern was the size and weight of the massive copper powder filters.

This led to the development of the second version of the filters (Fig. 16 right). Based on the same filtering idea the geometrical aspects have been changed massively. The loom carrying the wires is now just coated with a thin layer of the filtering mass (copper powder and Stycast) and then wound around two copper posts. The Stycast is hard enough to protect the wiring and the thermal coupling through the copper posts is still good enough. No additional copper housing is needed in this version. The filter is split into two parts one for each 24 wire loom and thus can be built in separately per sample. To get an idea of the size difference the base of the two versions of filters is sketched in Fig. 17. The height of both filters is comparable. The additional obtained space with version 2 can now be used for further options, like the installation of coaxial wiring for high frequency measurements. The downside of version 2 is the missing mounting for the R-C-filtering.

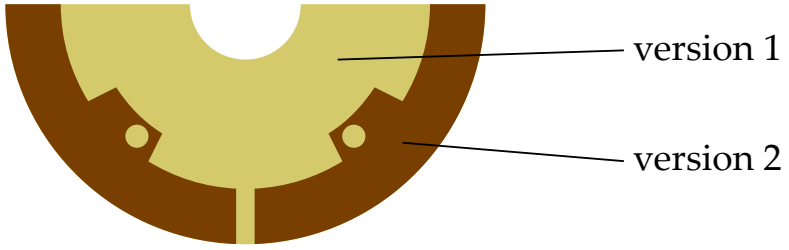

Figure 17: Comparison of the base of the two versions of copper powder filters. The height is similar.

To distinguish which filters have been used for a certain measurement the icons shown in Fig. 18 are placed next to the graphs depending on the installed filters. After optimizing the electrical connections to the sample all the magnetic influences need to be checked carefully.

4.3 MEASUREMENT SETUP

The environment for the sample needs to be prepared carefully before even building it in. All materials in the vicinity need to be checked to ensure none are superconducting, which could, due to them being diamagnetic, distort the applied magnetic fields.

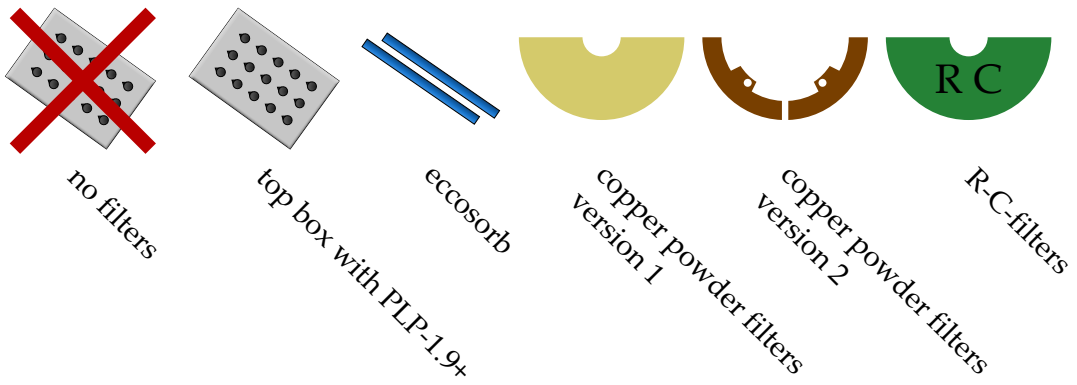

Figure 18: These icons are used in the measurement plots to indicate the used filtering

4.3.1 *Magnetic coil*

All cryostat systems, used for the measurements in this thesis, have superconducting coils built in to generate the magnetic field at the sample. The next paragraphs discuss how to optimize these coils for measurements on superconducting samples.

The materials used for the coils are based on type 2 Ss and show magnetic remanence, which depends on the magnetic history. As a result the size of the remnant field is not a fixed value, but is generally unknown. Depending on the maximum field generated by the coil the typical values range from 5 mT (9 T) to 15 mT (16 T) at zero current. These magnetic fields could already lead to trapped flux in the S in the sample, when cooling below the critical temperature.

The easiest way of reducing the remnant field is to do a so called *de-gaussing* procedure. The maximum remnant field is reached at 1 T. Starting from this value, the magnetic field is driven repeatedly from positive to negative values while continuously lowering the maximum amplitude. This procedure reduces the remnant field below 1 mT. [66]

As mentioned above the size of the remnant field is unknown, which means one can not know the exact position of zero magnetic field. To get around this problem an additional device can be created on a sample and the position of a distinct feature at zero field is used as a reference point. All magnetic values given in this thesis need to be considered as relative values.

A cleaner solution would be the construction of a superconducting shield to remove all magnetic field around the sample [67]. Inside this shield a non-superconducting coil creates a small magnetic field, which does not show remnant behavior. As a result

the magnetic zero is always also at zero current. Due to time constraints this could not yet be realized.

The power supplies normally used with superconducting magnet coils are optimized for big outputs to be able to supply the currents needed for fields of several Tesla. Consequently they do not perform as good in terms of resolution and linearity in very small field ranges. To get around this limitation the original power supply is completely disconnected and a high resolution current source is used. That way the distortions in magnetic field caused by the original power supply are no longer visible and the resolution is increased from 0.2 mT to 10 µT. The size of a typical oscillation is in the range of 0.5 mT.

4.3.2 *Bias measurement*

The most basic measurement setup is sketched in Fig. 19 (central and upper red part). A direct current (DC)-voltage is applied over the reference resistor R_{Ref} and the sample (symbolized as resistor R_{Sample}). The voltage measurement over R_{Ref} gives the current I flowing. Simultaneously the voltage drop V_{Sample} over R_{Sample} is recorded. This is often referred to as I-V measurement.

The 1:1 voltage amplifiers are used to maximize the input impedance in front of the voltmeter. They additionally shield the sample from noise generated in the voltmeter.

Depending on the desired measurement range R_{Ref} has to be adjusted. If one focuses on ranges away from the critical current $|I| \gg |I_{\text{crit}}|$ the sample resistance is not changing very strongly and one can choose $R_{\text{Ref}} \approx R_{\text{Sample}}$.

If however one is interested in the range close to I_{crit} the current should still be changed in equidistant steps with the applied voltage. To ensure this holds for the non-superconducting ($R_{\text{Sample}} > 0$) as well as the superconducting ($R_{\text{Sample}} = 0$) sample the reference resistance needs to be chosen that $R_{\text{Ref}} \gg R_{\text{Sample}}$ at all times. The former situation is referred to as voltage bias and the latter as current bias.

To be able to resolve small resistance changes the setup can be extended to additionally measure the differential resistance (see Fig. 19 blue part). A small alternating current (AC) signal is coupled into the DC line using a transformer. The voltage drop over reference and sample is then detected using lock-in amplifiers and digitized via a second voltmeter. The devices influencing the sample (e.g. DC-source and magnetic

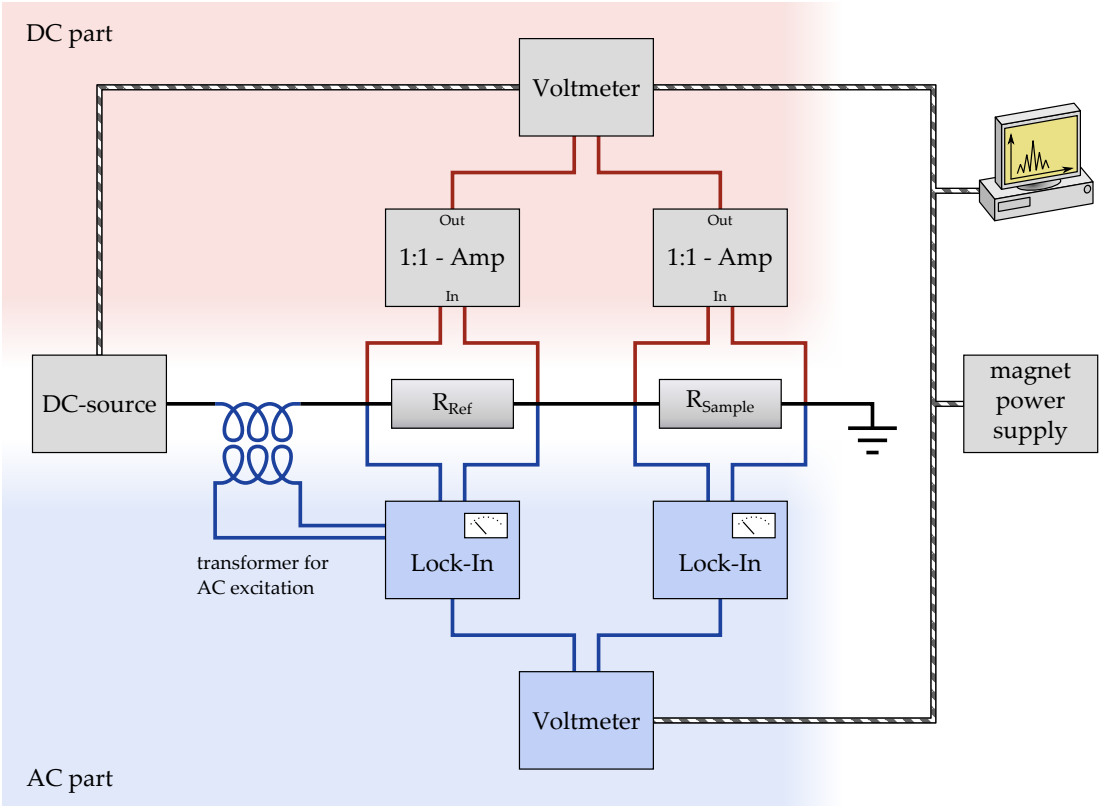

Figure 19: Setup overview for a DC measurement (upper red and central part) and extension with the AC measurement components (lower blue part). If only the DC part is used the transformer is not built in.

power supply) are set and the voltmeters are read by a computer connected via GPIB[11] (shown as hatched lines in Fig. 19).

The advantage of this setup is the good signal-to-noise ratio, which allows high resolution of measurements. But due to the integration time of the used instrumentation these two types of measurements need several seconds to record a single measurement point. Often one only wants to record the maximum critical current dependent on e.g. magnetic field. To get around the integration time limitation a different approach was taken with the next method.

4.3.3 *Threshold measurement*

To be able to conduct faster measurements of the critical current an ADwin[12] system was used. This system consists of a programmable processor and several analog in- and outputs that can read and set voltages on a timescale of µs.

11 General Purpose Interface Bus (also called IEEE-488); a digital bus system to exchange commands and measurement data

12 ADwin 16 light Rev. B by Jäger Computergesteuerte Messtechnik GmbH

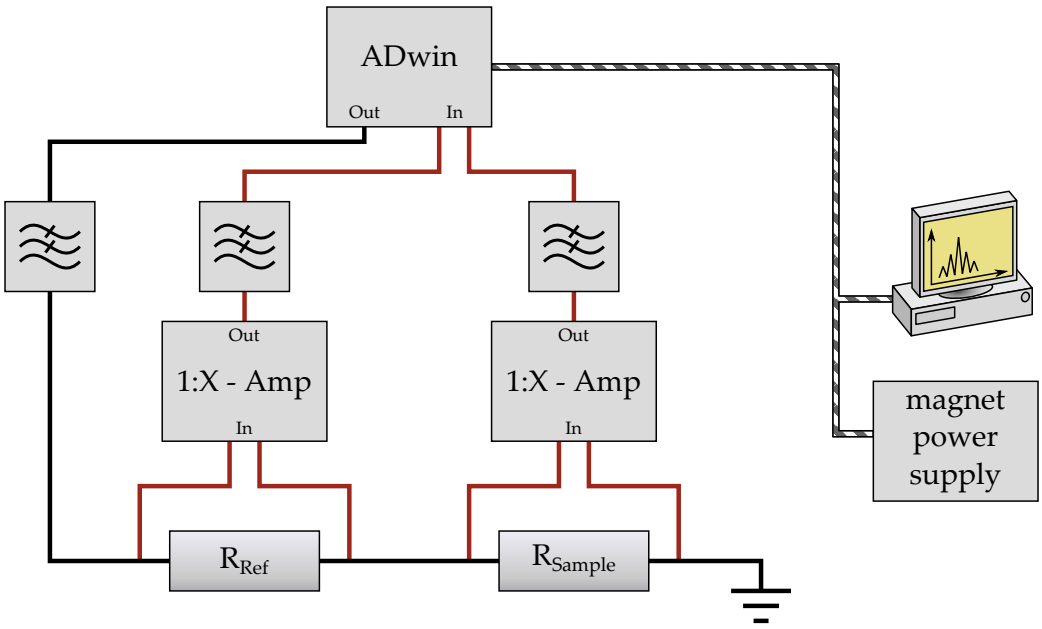

Figure 20: Measurement system with the ADwin unit. Low-pass filters are included to filter high frequency noise from the processor.

A sketch of the setup can be seen in Fig. 20. Comparable to the above mentioned setup the ADwin system applies a voltage over R_{Ref} and R_{Sample}. To measure the voltage drop the inputs of the system are used. They have a range of ± 10 V with a resolution of 375 µV. This is not enough to resolve the voltage drop over R_{Sample}. As a result the signal needs to be strongly amplified before it is passed on to the system. To achieve this the above mentioned 1:1-amplifiers have been altered to give amplification factors ranging from 10 to 100,000. One now has to take into account, that higher amplification also leads to higher capacitance in the amplifiers and thus limits the possible measurement speed.

The clock frequency of the ADwin processor leads to output noise on all connections to the system. To ensure the noise of the processor has no effect on the sample RC-low-pass filters with a cutoff frequency of 2.1 MHz are used in all lines.

To measure the critical current I_C of a device the ADwin system stepwise increases the voltage and – because in this configuration current bias has to be used – the current I is increased at the same time. Every step the sample voltage V_{Sample} is measured [see Fig. 21 a)]. As soon as V_{Sample} differs from 0 V the device is no longer superconducting and the voltage over R_{Ref} and thus I_C is recorded. The detailed measurement procedure can be found in Appendix C.1 in form of the source code.

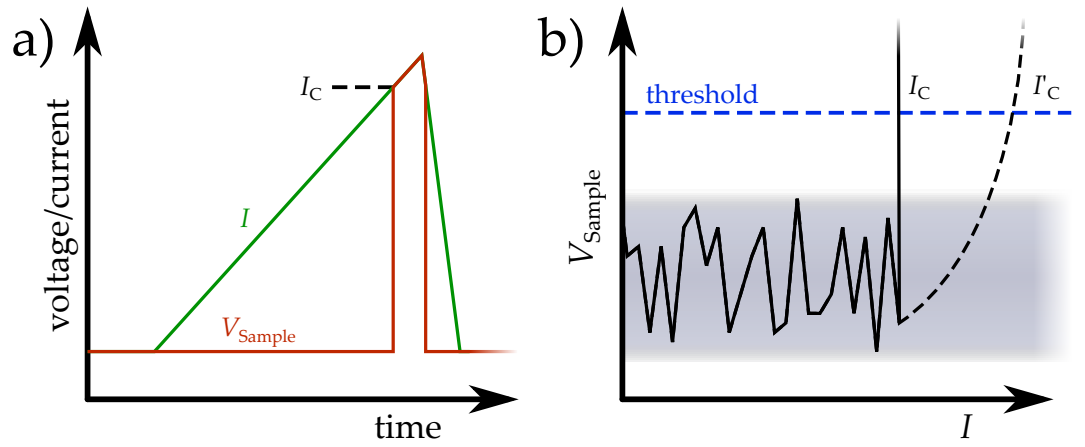

Figure 21: a) increasing current I and voltage drop over sample V_{Sample} up to critical current. b) threshold value above noise floor.

The limiting factor of this system is the resolution at which the 0 V can be measured. As a result one can only compare if V_{Sample} raises above the threshold value which needs to be chosen well above the noise level [see Fig. 21 b)]. This type of comparison is pretty exact as long as the transition from the superconducting to the normal state happens very sudden. In this case small variations of the threshold value do not change I_C. If the transition happens more slowly, because of high capacitance in the measurement system or if the critical energies of the system get comparable with thermal broadening, the measured I'_C is bigger than I_C and, due to the smaller slope, also depends on the chosen threshold.

The defining quality factor in this measurements is the amplifier used to measure V_{Sample}. The lower the noise level, the lower one can set the threshold and as a result the better I_C will be measurable.

While physically performing the same measurement as mentioned above we no longer are limited by the integration times of the high resolution voltmeters and the communication time between computer and measurement equipment. Measuring I_C once with the ADwin setup takes several ms. This enables the possibility to measure the critical current up to hundred times per second. The same timescale used to collect a single measurement point before. Additionally the collected data can be used to look at statistical fluctuations of I_C.

Another difference is the dynamic reaction of the system. Once I_C is reached the system immediately starts to reduce the current, leaving the device only as short as possible in the normal conducting regime and thus efficiently reducing joule heating

effects. This – at the same time – reduces measurement time, because the ramp is only driven as long as needed.

After this overview of sample production, all precautions necessary to ensure the best possible sample environment and used measurement techniques one can now focus on the results of measurements.

5

JOSEPHSON JUNCTIONS

Most measurements in this thesis are conducted on Josephson junctions (JJs). These junctions consist of a thin layer of non superconducting material X sandwiched between two S, forming the layer structure S/X/S. If the induced superconductivity in X is strong enough to bridge the distance between the two adjacent S the complete structure becomes superconducting. This weak coupling of two superconducting wave functions was first described by Brian David Josephson and was later called the Josephson effect, which describes the critical current flowing through the device dependent on the phase difference between both S [68].

The JJ geometry is interesting because the weak coupling is dependent on the type of material X, which in our case is the TI. Furthermore induced superconductivity in a TI of Josephson geometry should be able to host zero energy Majorana modes, which are expected to be visible in the critical current behavior of such devices [15, 69].

Additionally, the geometry is simple enough to test the general quality of the lithographic process, such as stability of the S, Nb, and transparency of the S/TI interfaces. The simplicity of the setup also makes it easier to interpret the results on this new and complex material system.

This chapter begins with a general discussion of the sample design and then determines the quality of the lithographically created S/TI interfaces. After having ascertained the samples quality the main part will be the discussion of JJs based on the 3D TI HgTe.

5.1 SAMPLE STRUCTURE

The general concept behind the sample design will be presented in the following section. In Fig. 22 one can see a selection of three samples which illustrate the development process.

The sample names are given in the upper left of each picture and are divided in three parts. The first part is the waver number, e.g "Q2446", which identifies the wafer and its properties, like thickness, mobility and carrier density of the HgTe layer. A list of the used HgTe material including the afore-mentioned values can be found in Appx. A.1 on page 115. The second part refers to the e-beam design used to create the sample, e.g. "Nb-SL VI". This effectively defines the position and size of the mesa and the S. The third part is an unique nickname to identify the sample and to simplify communication. As the full name is already given in Fig. 53, the following discussion only uses the nickname of the samples.

Many structures were fabricated to develop the lithographic process for contacting bulk HgTe with Nb, but only a few examples will be discussed here. As one can see in Fig. 22 all superconducting contacts run from top to bottom, crossing the mesa edge twice. Even though this makes the layout more complicated, it is necessary to be able to use angled sputtering of the Nb layer to increase the amount of Nb deposited at the upper edge. In prior tests non tilted contact deposition gave a stable metallic contact, but the thinned Nb at the upper mesa step did not stay superconducting in the required experimental range and thus effectively introduced two more unwanted JJs at this point. All Nb contacts to the HgTe mesa are split up for connecting them to two separate Au/Ge leads. This enables the use of 4-point measurements[1] and thus circumvents all resistances in the metallic leads as well as the wiring of the setup.

Before moving on to the characteristics of each individual sample the denotation of distances in the JJs have to be clarified to avoid any confusion. As shown in Fig. 23, the length of the JJ describes the distance between the two S. This distance has to be bridged by induced superconductivity to get a completely superconducting structure. The width of the JJ is the distance between the two edges of the mesa and it has a value of 2 µm for all three samples. It effects the area of the JJ and thus plays a role in effects like penetrating magnetic flux and the number of possible supported modes.

1 In a 4-point measurement the current path is separated from the voltage probes to only measure the resistance in the part of the structure, where current and voltage path overlap.

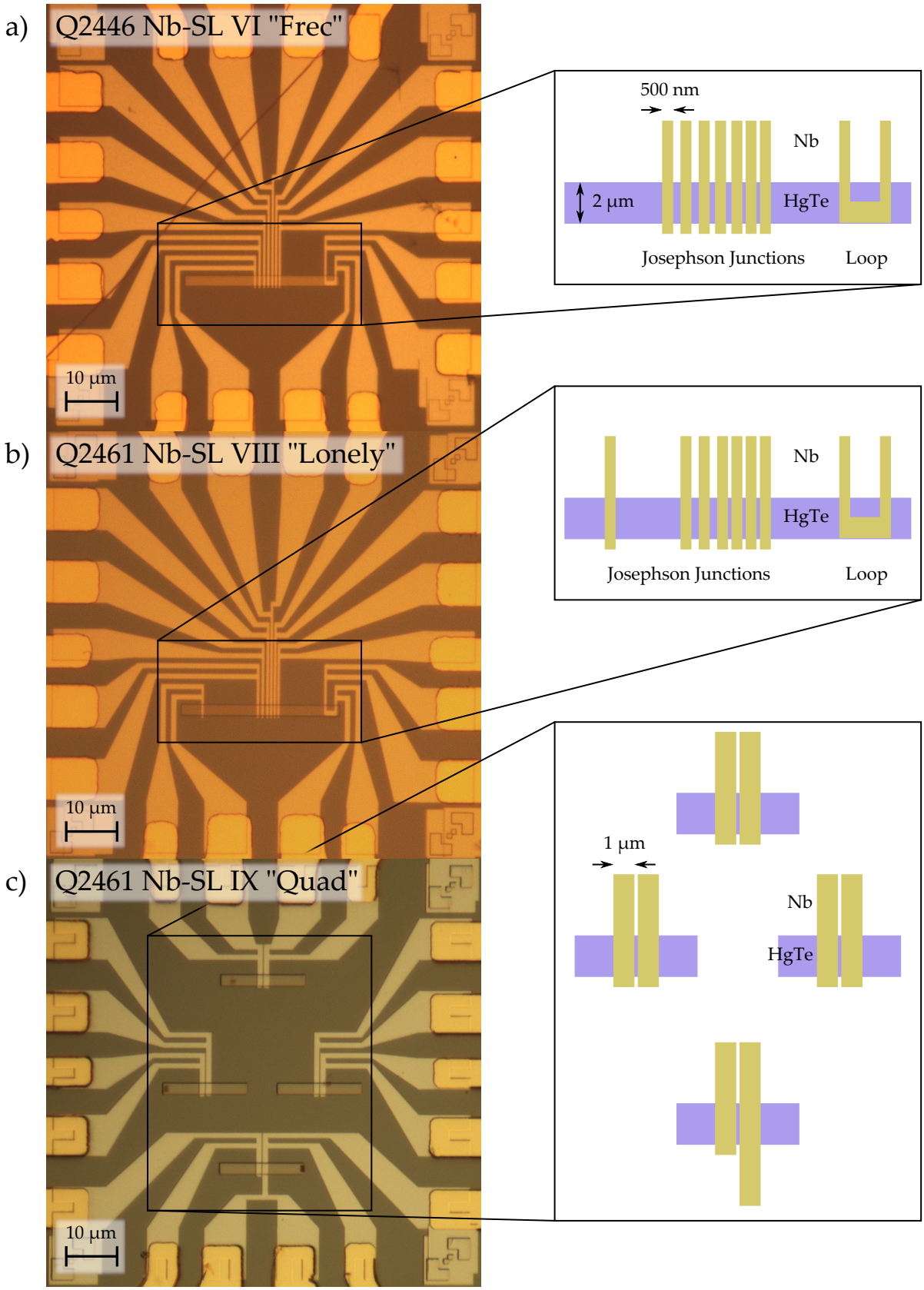

Figure 22: A set of exemplary samples. *Left side:* microscopic picture of the central area fabricated by e-beam lithography. Optically fabricated metallic contacts are still visible at the rim. *Right side:* schematic view of the functional structure built form HgTe and Nb.

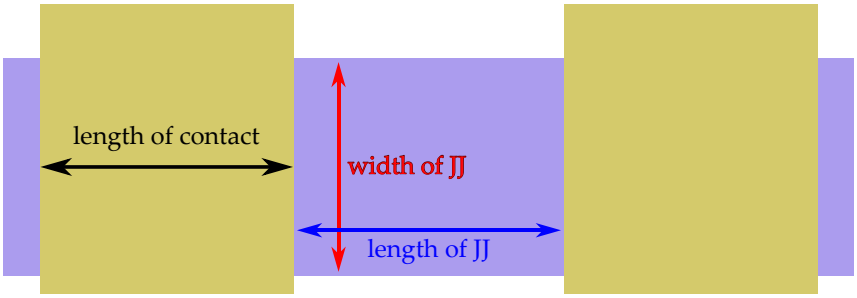

Figure 23: Definition of length and width of a JJ

The next step is to have a look at the effect of exposure and development on the nominal distances of a designs in order to find out what the actual distances are. During e-beam exposure the scattering of electrons leads to a gradient of exposure, rather than a sharp interface, between an exposed and unexposed area. This, combined with the strength of the development solution, determines if the actual structure will be bigger or smaller in relation to the nominally written structure [70].

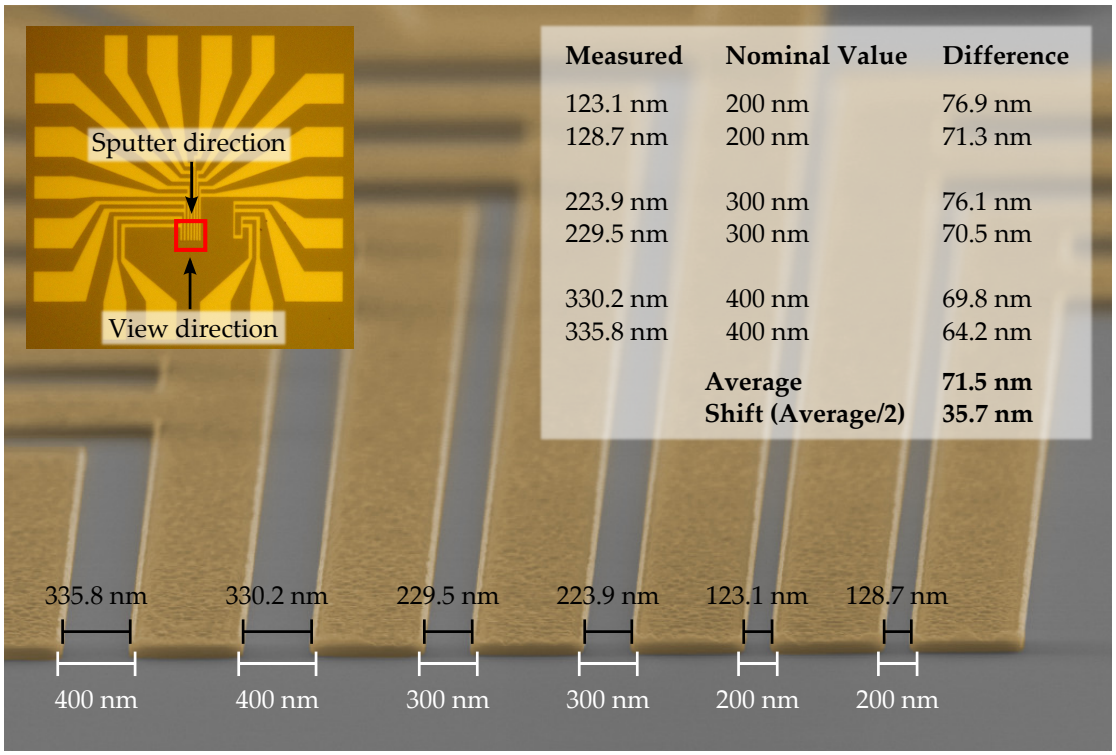

Figure 24: Nb stripes (orange) to test the difference between the nominal distance (white) and actual measured values (black). The deviations are listed in the table on the right. The optical picture on the left shows the complete structure and the area of the SEM image (red rectangle).

To quantify this effect a test sample with only the Nb layer has been produced. The result is shown in Fig. 24. At the bottom of the figure the nominal e-beam written distances are noted in white and above in black the measured distance from the SEM

image are given in comparison. The measured distance is smaller than the nominal distance. Because the area of the Nb is exposed, one can conclude, that the exposed area will always be slightly bigger, than the design. The table in the upper right corner gives the calculated differences and the average deviation of roughly 72 nm for the distance between two edges. Due to the measurement technique the error should be about 10 nm. It follows that a single exposed edge is shifted by 36 nm in the direction of the unexposed area.

Coming back to Fig. 23, this means a reduction of the nominal JJ length by 72 nm, which is a major change compared to the smallest junctions of 200 nm, which has to be taken into account. The same effect also influences the mesa and thus the width of the JJ. Here the 2 µm are increased by 72 nm, which is not a major influence, due to the bigger width in general. To keep notation of distances simple they will be given in nominal values, where not explicitly stated otherwise.

The first sample that showed an indication of a working JJ was "Frec" displayed in Fig 22 a). The idea behind this design was to ensure a stable lithographic process with regards to the angled sputtering technique. To test if the Nb layer is superconducting in the complete volume, especially at the mesa step, the superconducting loop was introduced, which, if working properly, should show a resistance of 0 Ω. The rest of the structure consists of multiple neighboring Nb contacts forming JJs with varying lengths. The distances are two times 400 nm, 300 nm and 200 nm respectively, as shown in Fig. 24. This allows the length dependent investigation of any Josephson related effects. The Nb contacts on this sample have been sputtered without any further treatment of the HgTe layer.

Being geometrically almost identical to "Frec" the main changes of sample "Lonely" [Fig. 22 b)] are found in the processing. The only difference in layout is the leftmost contact, which was moved further apart in order to investigate the behavior of the extreme limit of a very long JJ. However due to the state of the lithographic process at that time and thus only a limited amount of working JJs in "Frec" and "Lonely" it was not possible to further investigate length dependence.

Before the sputtering of the S, the surface of the HgTe layer was cleaned with a short Ar milling step to remove the oxide layer as well as any residual processing chemicals. Furthermore one expects to remove any additional perturbing insulating barriers in the system.

In the sample "Quad" the single mesa stripe of previous samples has been separated into four stripes with two superconducting contacts each. Due to the separation, interference between neighboring JJs can be ruled out, but this also reduces the amount of possible JJs with the same amount of contacts. To be able to compare the four devices all JJs have a length of 200 nm. As the superconductivity of the Nb layer has been tested in prior samples, the loop was no longer needed to ensure functionality of the samples.

Additional to Ar cleaning of the mesa, the transfer time to the sputtering chamber has been minimized in order to reduce the samples oxygen exposure time. By this means one should achieve the lowest amount of oxides between the S/TI interface with the available equipment. The initial step in ensuring functionality of the samples is to check the stability of superconductivity in the Nb leads.

5.2 CRITICAL PROPERTIES OF THE SPUTTERED NB

There are many ways to probe the SC in a material. In this case the transport properties were chosen for ease of access, namely the vanishing resistance of Nb in the superconducting state. Although all critical parameters would be available in literature they have to be confirmed for the samples at hand. The thin layer thickness of only 70 nm makes it hard to directly compare it with bulk Nb. Moreover, slight differences in the sputtering process can lead to great differences in the critical values, due to the incorporation of impurities [41].

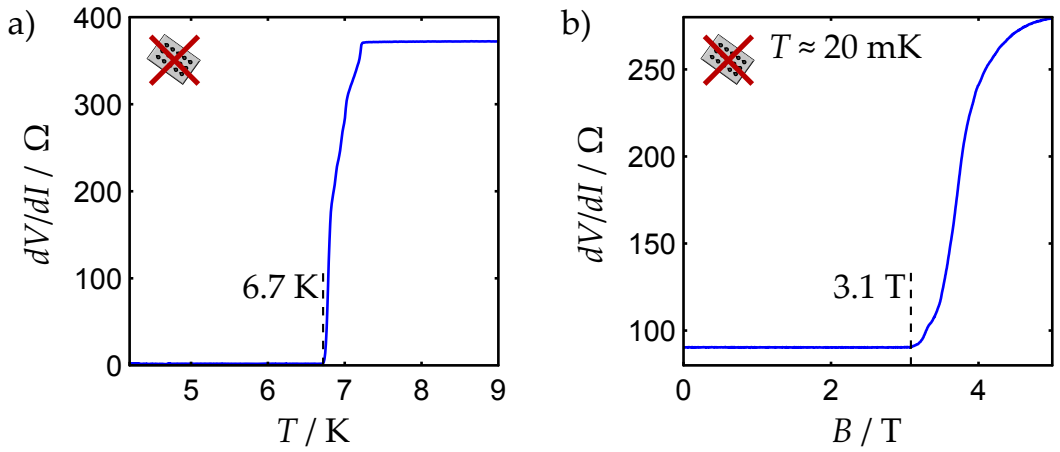

Figure 25: Differential resistance of the superconducting loop on "Frec" close to a) the critical temperature and b) critical magnetic field.

To test for superconductivity "Frec" was cooled down while monitoring the temperature T and collecting the differential resistance dV/dI over the loop in a 4-point measurement [see Fig. 25 a)]. One observes a sharp transition between 8 and 6 K which is not a singular event. The transition into the superconducting regime happens in several steps which can be attributed to different parts of the Nb layer getting superconducting at slightly different temperatures due to their geometrical differences. The complete loop is superconducting at $T_C = 6.7$ K. The literature value of pure Nb is $T_{C,\,lit} = 9.3$ K, but this can vary by up to 1 K due to different impurity concentrations [41]. The extracted T_C is too low and can only be taken as a rough estimate, as this measurement was taken during a continuous cool down of the cryostat. The thermal sensor only records the temperature close to the sample and thus, because the temperature was changed continuously, it is not guaranteed, that sample and sensor are in thermal equilibrium. Nevertheless the JJs are measured at temperatures below 1 K and in this region the Nb is in the superconducting state, far from T_C. During these initial measurements no special filtering was used as indicated by the icon in the upper left corner.

The magnetic measurements in Fig. 25 b) were taken at a temperature of 20 mK. The magnetic field B is oriented perpendicular to the mesa surface. Due to problems with the leads a 4-point measurement was not possible. Therefore the differential resistance was recorded in a 2-point configuration, which explains the offset caused by the lead resistance of 90 Ω at 0 T. It has already been shown that the loop gets superconducting and thus the constant resistance form 0 T to 3.1 T can be taken as the superconducting regime. At a critical field of $B_{C2} = 3.1$ T superconductivity is broken and hence the resistance is rising.

Because Nb it is a type II superconductor one has to be careful regarding the breakdown of SC in a transport measurement. One can only extract the upper critical magnetic field intensity which, converted form B_{C2}, is $H_{C2} = 2.5$ MA/m. This value is huge compared to pure Nb with $H_{C2,lit} = 0.29$ MA/m. The increased magnetic field intensity is a result of defects in the Nb crystal and expected in a sputtered material. The more important value for our experiments is $H_{C1,lit} = 0.13$ MA/m, below which Nb behaves as a type I S. This value can not be extracted from transport measurements, but it also does not change as drastically as H_{C2} with impurity concentration and is expected to be in the same order of magnitude as $H_{C1,lit}$ (values taken from [41]).

Again the important factor is the comparison with a typical JJ measurement, where the applied magnetic field range is ± 20 mT. This is equivalent to a magnetic field intensity of 0.016 MA/m and thus far from $H_{C1,lit}$. If the applied magnetic field intensities reach values above H_{C1} at any point during the experiment, flux tubes can enter the S and get pinned at impurities. If the field is reduced below H_{C1} afterwards and the Nb returns to its type I state, those tubes are still pinned and present in the system. The only way to return to the pure type I state is to warm up the S above T_C and cool down again without applied field. This should be kept in mind while measuring with type II Ss.

In summary it can be said that, as long as one stays within the typical measurement range, the Nb contacts are superconducting and behave like a type I S in the Meissner phase. After having established the functionality of the Nb, one now has to discuss the contacts quality between the sputtered Nb and the HgTe.

5.3 S/N INTERFACE WITH FINITE TRANSPARENCY

Section 3.2 has already introduced the idea of inducing a superconducting band gap in a normal material due to Andreev reflection at the boundary. It is now time to establish a model to quantitatively describe a S/TI interface in terms of transparency.

A basic model for a S/N interface has been proposed by G. E. Blonder, M. Tinkham and T. M. Klapwijk, which is now commonly refered to as BTK model [58]. The generalization of the BCS theory with the BdG equations allowed the definition of a spatially varying pairing potential $\Delta(x)$. The S/N interface is placed at $x = 0$, with $x < 0$ being normally conducting and $x > 0$ being superconducting. The pairing potential is chosen to be

$$\Delta(x) = \Delta_0 \Theta(x), \tag{28}$$

with the Heaviside step function $\Theta(x)$ and a scalar value for the pairing potential Δ_0. In other words, the N has no pairing potential and the S has a constant potential of Δ_0. Additionally the BTK model introduces a repulsive potential

$$V(x) = F\delta(x), \tag{29}$$

which is only present at the interface $x = 0$. The wave functions are once more denoted in Nambu basis as vectors with the upper component describing the electron-like part and the lower component describing the hole-like part of the particle. Only elastic tunneling processes are allowed, meaning that incoming particles with positive group velocities ($dE_k/\hbar dk$) can only generate transmitted particles with positive group velocities or reflected particles with negative group velocities. Starting from an incident electron from the normal conductor $\psi^{\mathrm{N}}_{\mathrm{inc}}$, four processes are possible: The electron is Andreev reflected as a hole, it is reflected as an electron in the N (both described by $\psi^{\mathrm{N}}_{\mathrm{refl}}$), or it is transmitted into the S as a hole-like or electron-like quasiparticle (described by $\psi^{\mathrm{S}}_{\mathrm{trans}}$).

$$\psi^{\mathrm{N}}_{\mathrm{inc}} = \begin{pmatrix} 1 \\ 0 \end{pmatrix} e^{ik_+ x}, \tag{30}$$

$$\psi^{\mathrm{N}}_{\mathrm{refl}} = a \begin{pmatrix} 0 \\ 1 \end{pmatrix} e^{ik_- x} + b \begin{pmatrix} 1 \\ 0 \end{pmatrix} e^{-ik_+ x}, \tag{31}$$

$$\psi^{\mathrm{S}}_{\mathrm{trans}} = c \begin{pmatrix} u^2_{k0} \\ v^2_{k0} \end{pmatrix} e^{ik_+ x} + d \begin{pmatrix} v^2_{k0} \\ u^2_{k0} \end{pmatrix} e^{-ik_- x}. \tag{32}$$

Looking at the vectors, one finds that states in the N are pure electronic or hole states, while the S also allows superpositions of both. To be able to predict the transport behavior of this interface the prefactors a - d of Eqs. (30)-(32) have to be calculated. This is done by looking at the boundary conditions at $x = 0$. The total wave function ψ must be continuous at the interface

$$\psi^{\mathrm{N}}(0) = \psi^{\mathrm{S}}(0) = \psi(0). \tag{33}$$

And the derivative has to satisfy

$$\frac{d\psi^{\mathrm{S}}(0)}{dx} - \frac{d\psi^{\mathrm{N}}(0)}{dx} = \frac{2m}{\hbar} F\psi(0). \tag{34}$$

Using the energy dependence of the wave functions extracted from the BdG equation [58], which is not explicitly shown here, one can calculate the probability current for Andreev reflection $A(E)$ and normal reflection $B(E)$. For energies above the superconducting band gap $|E| > \Delta_0$ the probabilities are

$$A(E) = |a(E)|^2 = \frac{u_0^2 v_0^2}{\gamma^2}, \tag{35}$$

$$B(E) = |b(E)|^2 = \frac{\left(u_0^2 - v_0^2\right)^2 Z^2 \left(1 + Z^2\right)}{\gamma^2}. \tag{36}$$

And below the gap $|E| < \Delta_0$ the result is

$$A(E) = |a(E)|^2 = \frac{\Delta_0^2}{E^2 + \left(\Delta_0^2 - E^2\right)\left(1 + 2Z^2\right)^2}, \tag{37}$$

$$B(E) = |b(E)|^2 = 1 - A(E), \tag{38}$$

with the dimensionless barrier parameter $Z = mF/\hbar^2 k_\mathrm{F}$, the substitution $\gamma = u_0^2 + \left(u_0^2 - v_0^2\right) Z^2$ and the subscript k has been dropped.

The energy dependance of the quasi particle amplitudes is

$$u_0(E) = \sqrt{\frac{1}{2}\left(1 + \sqrt{\frac{E^2 - \Delta_0^2}{E^2}}\right)} \quad \text{and} \quad v_0(E) = \sqrt{1 - \left(u_0(E)\right)^2}. \tag{39}$$

With the probability amplitudes $A(E)$ and $B(E)$ one can calculate the total current $I(V)$ passing through the interface with an applied bias voltage V

$$I(V) \propto \int_{-\infty}^{\infty} \left[f(E - eV) - f(E)\right]\left[1 + A(E) - B(E)\right] dE, \tag{40}$$

with the Fermi distribution $f(E) = 1/\left(\exp\left(\frac{E-\mu}{k_\mathrm{B}T}\right) + 1\right)$. It is directly apparent from Eq. (40) that the Andreev reflection probability $A(E)$ increases the current flow, because in this process a single incident electron transfers the charge of $2e$ over the interface. On the contrary the reflection of a normal electron does not transfer any charge and thus $B(E)$ reduces the current.

For a better understanding of these equations a look at the extrema is helpful. If the energy is below the superconducting band gap Δ_0 and no barrier is present ($Z = 0$) Eq. (37) reduces to $A(E) = 1$, meaning every incoming electron is Andreev reflected, while creating a cooper pair. At the same time $B(E) = 1 - A(E) = 0$. Hence no electrons are reflected and reduce the current flow. In this case the current flow is doubled in the region of the superconducting band gap.

At the other extreme of an infinite barrier ($Z = \infty$) no Andreev reflection is possible ($A(E) = 0$) and all electrons are normal reflected ($B(E) = 0$). Unsurprisingly there is no current flow possible.

With the now known voltage dependence of current I in Eq. (40) one can numerically compute the differential resistance dV/dI of this problem. This is useful as we can directly compare it to dV/dI measurement results on the JJs. Figure 26 shows dV/dI normalized by the normal resistance R_{normal} as function of the applied voltage V (normalized by the gap Δ_0).

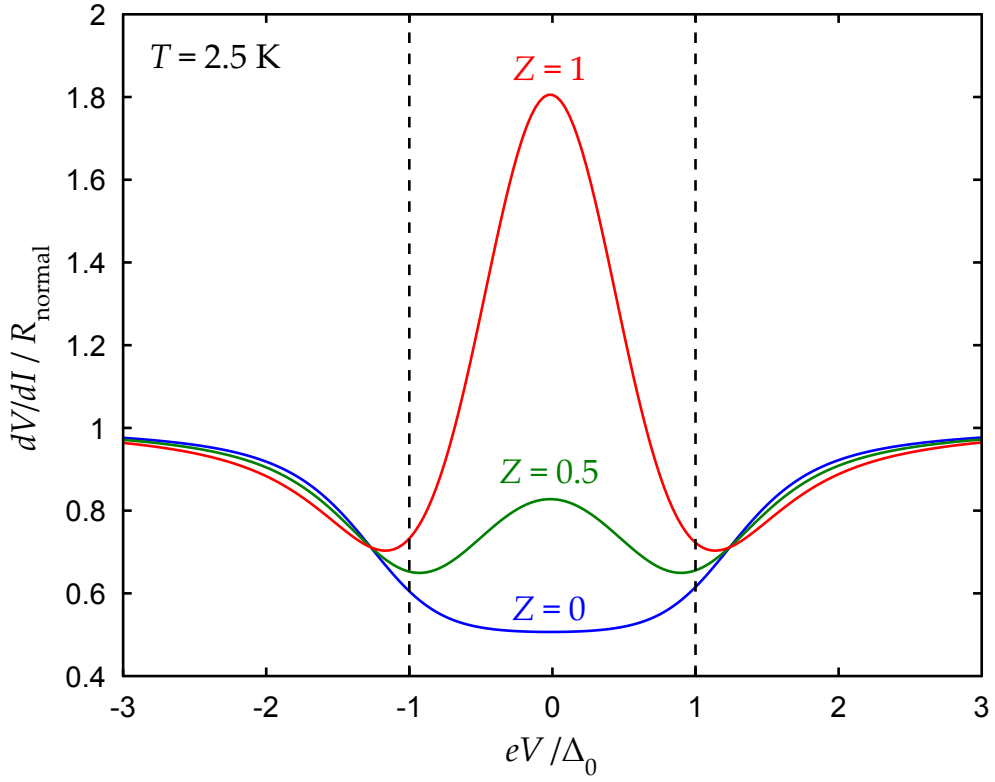

Figure 26: The graph shows a exemplary result of the BTK model. The differential resistance dV/dI over a S/N interface is plotted against the applied voltage V over the interface for different transparencies Z. The dashed lines show the position of the superconducting band gap Δ_0.

R_{normal} is taken at voltages far from the superconducting gap ($|eV| \gg \Delta_0$) and thus is not influenced by Andreev processes at the interface. In this region the resistance is constant and the system behaves like N/N. Approaching the band gap ($|eV| > \Delta_0$), but staying above, the influence of the superconductors increased density of states [see Fig. 9 b) on page 28] reduces the resistance compared to R_{normal} . When reaching values inside the band gap ($|eV| < \Delta_0$) the barriers influence becomes apparent. For a non existent barrier ($Z = 0$) the resistance is halved, because of the current doubling

due to a dominant Andreev reflection, as mentioned above. For higher barriers ($Z > 0$) one sees a sharp increase of the resistance in the gap.

To turn the argumentation around: One can fit measured dV/dI curves with the BTK model to extract the transparency of an interface, which is directly connected to the amount of Andreev reflection events. This helps to optimize devices for maximum induced SC.

Before applying the BTK model it should be verified if it is valid it in the considered case. The major difference between the model and the samples is the following: the former is based on a S/N interface and the latter consists of a S/TI/S interface.

One can argue that as long as no phase coherent transport between the two S in the samples is possible, the structure can be seen as two separate interfaces in a row (S/TI and TI/S). This is true for higher temperatures and low interface transparencies.

The second aspect is the replacement of the N with a TI. There are special effects expected for low transparencies and energies below the superconducting gap [71]. However in this regime other effects start to dominate the double S/TI junction as seen later. For a proper characterization of a single S/TI interface different samples would have been necessary, which unfortunately could not be produced in the scope of this thesis.

After discussing the concept of the BTK model, it should be compared to a first measurement. Figure 27 shows a dV/dI measurement over a 200 nm long S/TI/S junction on sample "Frec" as a function of the applied DC voltage V_{DC}.

The normal resistance $R_{\mathrm{normal}} = 210\ \Omega$ includes the two S/TI interface resistances, as well as the HgTe region resistance. The latter should only vary slightly, as long as the geometries of the compared devices are identical. As a result R_{normal} can also be used as an estimate for the absolute value of the interface resistance.

As we are looking at a double S/TI interface the dip in resistance caused by the increased density of states no longer appears at Δ_0, but at $2\Delta_0$, which in this case is $2\Delta_0/e = 2$ mV. The theoretical value for ultra pure bulk Nb is 2.91 meV [49]. The difference could be due to the layer thickness of only 70 nm and a higher amount of impurities in the sputtered material.

An important factor is the dimensionless barrier height Z extracted from the BTK model, as this value gives an idea of the probability of Andreev reflection $A(E)$. Even without the fitting curve one can see the strong increase of dV/dI in the superconducting band gap by a factor of 1.6 due to the dominance of regular reflection. The

detailed fit yields a value of $Z = 1.83$, which results in a quite small $A(E)$ as it is shown in the comparison in Fig. 30 at the end of this section.

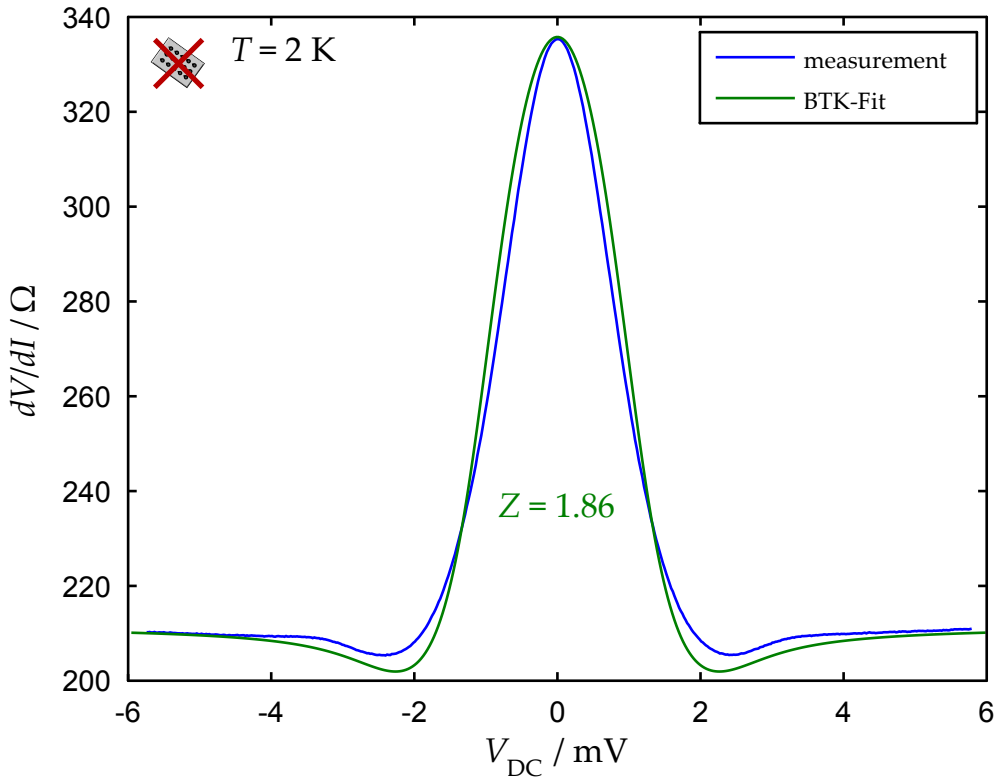

Figure 27: dV/dI measurement on 200 nm S/TI/S junction of sample "Frec" plotted against the applied voltage V_{DC}. The comparison with the BTK model yields a barrier strength of $Z = 1.83$.

The next step of improvement was already mentioned during the sample description, the contacts were cleaned in a short etch step in Ar plasma to remove parasitic contaminations and oxides, resulting in sample "Lonely". The resistance measurement is shown in Fig. 28. The most striking feature is the decrease of R_{normal} to 77 Ω. This is only 37 % of the measured value on the previous sample "Frec" and the relative difference between R_{normal} and the maximum value in the gap has fallen to 1.3 (1.6 in "Frec"). The model yields $Z = 1.3$.

This decrease in barrier strength considerably increases $A(E)$, as displayed in Fig. 30. One also notices that the BTK fit curve is no longer able to fully describe the measurement's behavior. There are two possible explanations for this: Either the assumption that both S/TI interfaces can be treated as identical is not true and one actually has a superposition of two BTK curves with different Z and Δ_0; or the assumption of two separate S/TI junctions is no longer valid and the two separately described superconductors start to interact. Even though the answer can not be clearly derived

from these data the second explanation becomes more plausible, if one consideres the further development of the next sample.

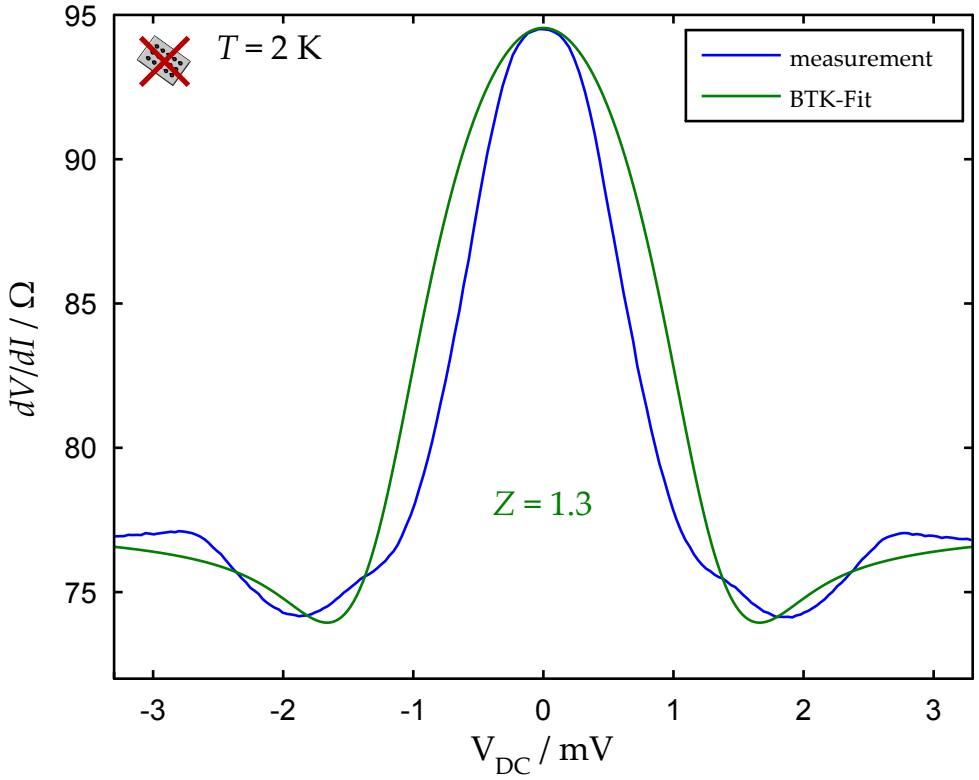

Figure 28: dV/dI measurement on 200 nm S/TI/S junction from sample "Lonely" plotted against the applied voltage V_{DC}. Due to the surface treatment $R_{normal} = 77\ \Omega$ as well as $Z = 1.3$ could be reduced compared to "Frec".

The last sample in this discussion is "Quad", which was characterized in a measurement in a liquid helium can. As a consequence the temperature is fixed at $T = 4.2$ K. Looking at Fig. 29 the curve is much rougher, because the environmental noise in the helium can is bigger than in a cryostat.

The lithographic optimization step concerning this sample was to minimize the exposure to oxygen after the cleaning step by transferring it as fast as possible from cleaning to sputtering. The results show that the obtained data can no longer be explained with the BTK model as the main feature, the resistance in the band gap, no longer fits to the theoretical expectation. For comparison three values for Z are plotted, to demonstrate that also the shape of the graph far off $V_{DC} = 0$ V does not allow to extract any further information.

This behavior however is the desired result. The two superconductors start to interact through the HgTe layer effectively reducing the device's resistance.

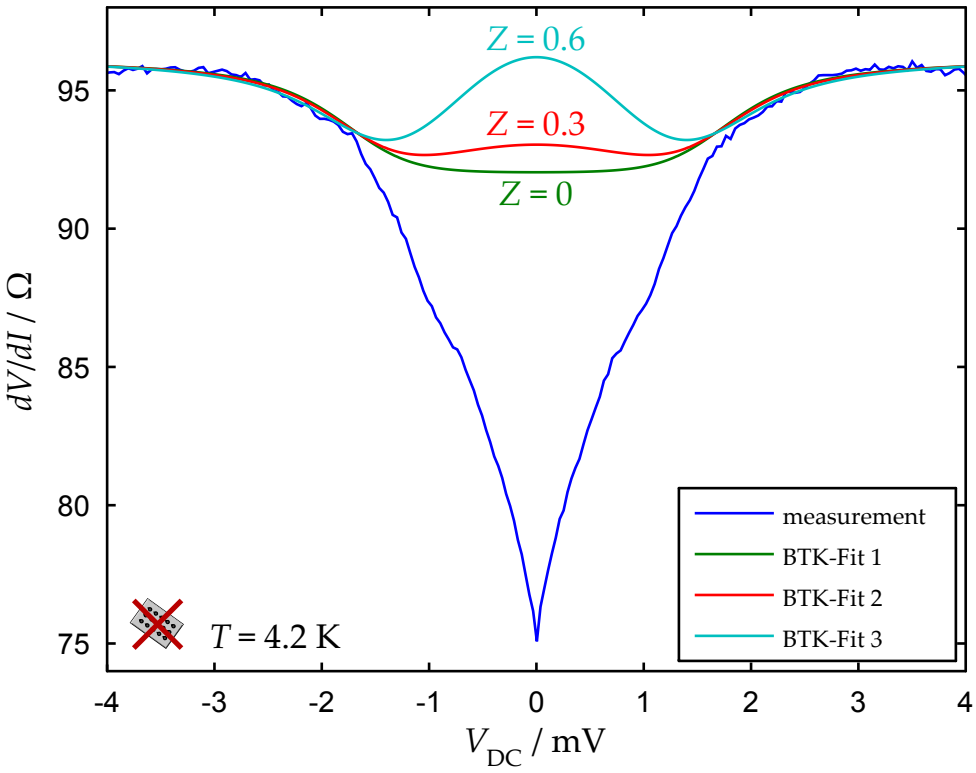

Figure 29: dV/dI measurement on 200 nm S/TI/S junction from sample "Quad" plotted against the applied voltage V_{DC}. The BTK model no longer is applicable within the given parameters.

The presented optimizations were able to continuously increase the amount of Andreev reflection at the interfaces. This is summed up in Fig. 30, where starting with a barrier of $Z = 1.83$ the lithographic development allowed a decrease to 1.3. This is equivalent to more than a doubling of $A(E)$. "Quad" should have a barrier between $Z = 1.3$ and 0, but this could only exactly be extracted in a single S/TI junction with the BTK model. As the goal of these samples was to fabricate a JJ no such sample was built. Another way of extracting the transparency of a complete JJ will be presented later.

So far only measurements in the Kelvin range were shown to lay out the optimization process. All the samples were additionally measured at 25 mK where they also showed signs of interaction between the two S, already. To get an idea how much the optimization helped to reach the goal of a stable JJ the best possible result of each sample will be shortly listed here, without showing detailed measurements.

"Frec" was the first sample to show a small drop in resistance in the center of the gap, indicating a first interaction. "Frec" together with the first measurements

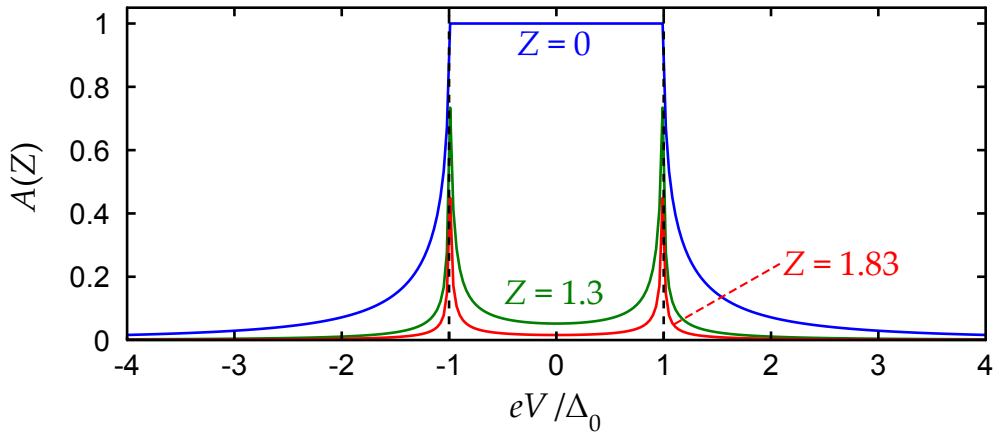

Figure 30: Probability of Andreev reflection $A(Z)$ plotted against the applied voltage V using Eqs. (35) and (38). The voltage is normalized by the superconducting band gap Δ_0/e. The barrier heights Z correspont to the values extracted form the samples "Frec" (1.83), "Lonely" (1.3) and the ideal case (0). The value for "Quad" can not be extracted using the BTK model.

on "Lonely" were used to write a paper [72], were there hints for proximity induced supercurrents were found, but everything was still in the resistive regime.

Only after installing copper powder filters the detection of the tunneling of a supercurrent was possible with the sample "Lonely". "Quad" showed an increase of all critical values and the results were published in Ref. [73].

The question now arising is, how do supercurrents evolve in the non-superconducting part in a S/TI/S junction?

5.4 DEVELOPMENT OF SUPERCURRENT IN A JOSEPHSON JUNCTION

In order to understand the tunneling of supercurrents between two S one first has to extend the discussion on Andreev reflection in Sec. 3.2 on page 30. Therefore the well known theory for a S/N/S junction will be presented first and the introduction of a TI will be addressed later.

In an S/N/S junction, as shown in Fig. 31, with an applied voltage V the two superconductors S_1 and S_2 are at the chemical potentials μ_{S_1} and μ_{S_2} respectively. The voltage shifts the relative chemical potentials by $eV = \mu_{S_1} - \mu_{S_2}$.

If the DC voltage is above $2\Delta/e$ electrons can directly be transferred form the valence band of S_1 through the TI to the conduction band of S_2 without AR having any influence, as seen in the inset in Fig. 31.

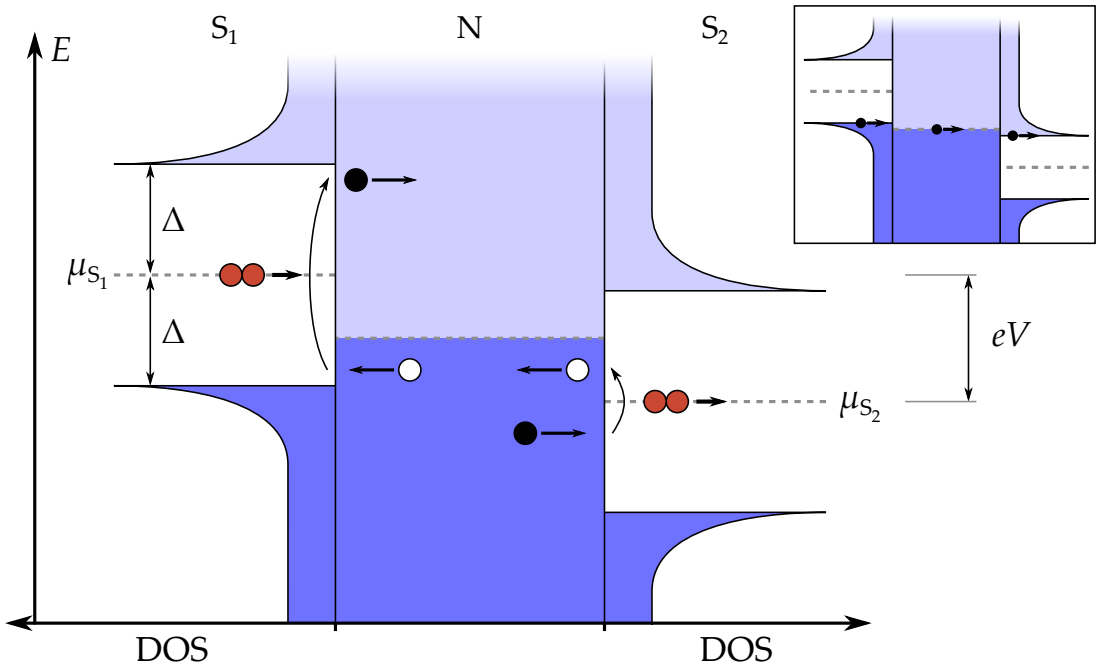

Figure 31: Schematic depiction of twofold Andreev reflection at a S/N/S interface with a voltage V applied. The inset shows the case of normal conduction with $V < 2\Delta$.

The interesting part begins for voltages lower than $2\Delta/e$. Compared to a single Andreev reflection more complex processes are possible due to the introduction of the second S. As shown in the figure, an incident electron (black) can be retroreflected as a hole (white) while creating a cooper pair at S_2 (red). The hole is then again Andreev reflected at S_1 converting it back to an electron, while annihilating a CP. This electron is now energetically above the band gap of S_2 and can enter its conduction band. During this process a charge of $3e$ is transferred with two consecutive Andreev reflections, also called twofold AR. The voltage range of this effect is $2\Delta < eV < \Delta$.

If the voltage is below Δ/e the electron can be reflected a third time or to generalize the effect: If the applied voltage is smaller than

$$V_n = \frac{2\Delta}{e\,(n-1)} \quad n = 2, 3, \ldots \tag{41}$$

n-fold AR can take place, transporting a total charge of $(n+1)\,e$ over the junction. The aspect of increased charge transfer can, e. g. be seen as plateaus in the differential resistance every time the next order of AR becomes possible, by lowering the applied voltage. All types of AR with more than one reflection are called multiple ARs.

It has already been discussed in Sec. 3.2 on page 30, that as long as electrons and holes participating in the AR in the normal conductor are phase coherent they can introduce a superconducting gap. The length dependence of this effect is given by

Eq. (25). If the applied voltage is lowered to a small enough value and the effect is strong enough to begin with, the induced gaps of S_1 and S_2 can overlap and the complete junction gets superconducting.

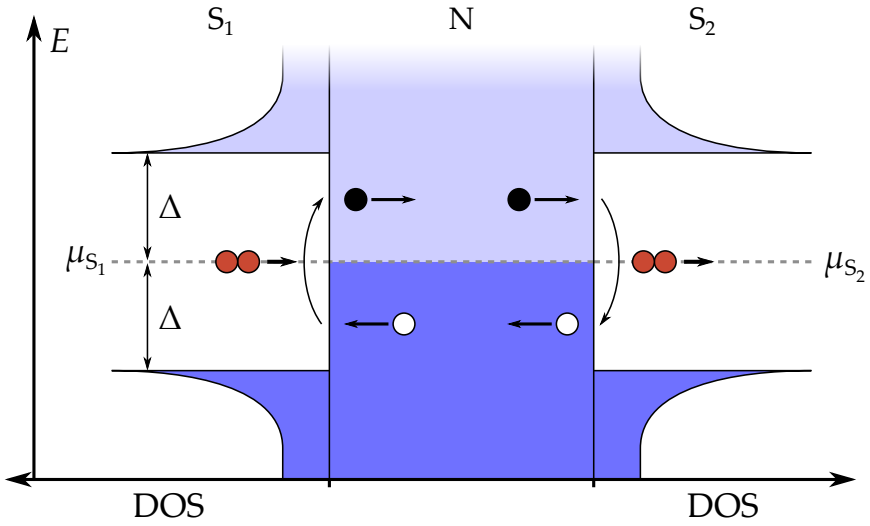

Figure 32: Andreev bound state in a S/N/S junction due to equal potentials $\mu_{S_1} = \mu_{S_2}$

In the superconducting state no voltage drop over the junction is possible and thus the chemical potentials have to be equal $\mu_{S_1} = \mu_{S_2}$. In the context of Andreev reflection this leads to the special situation sketched in Fig. 32. An electron is reflected as a hole, which is then reflected as an electron and ends up in the same state as it started. As a result this process can be repeated infinitely and is called an Andreev bound state. In addition the process is constantly transporting CPs from one S to another.

This effect was predicted by Brian David Josephson in 1962. He assumed, that in the simplest case of a one dimensional weak link the supercurrent I_S carried by the JJ is given by the difference of the macroscopic phase $\Delta\phi = \phi_{S_1} - \phi_{S_2}$ of the two S as [68]

$$I_S = I_{C0} \sin(\Delta\phi) . \tag{42}$$

The above expression is known as the current phase relation of the JJ. I_{C0} is the maximum critical current possible without the influence of any pertubation, e. g. temperature.

Describing the behavior of a device solely by Eq. (42) is far form a realistic junction as the equation only says, that as long as one operates the JJ below I_S, a dissipationless supercurrent is flowing. But what happens above this limit? To reach a more realistic situation the junction can be described as a resistively and capacitively shunted junction (RCSJ) [43]. The equivalent circuit diagram is shown in Fig. 33 a).

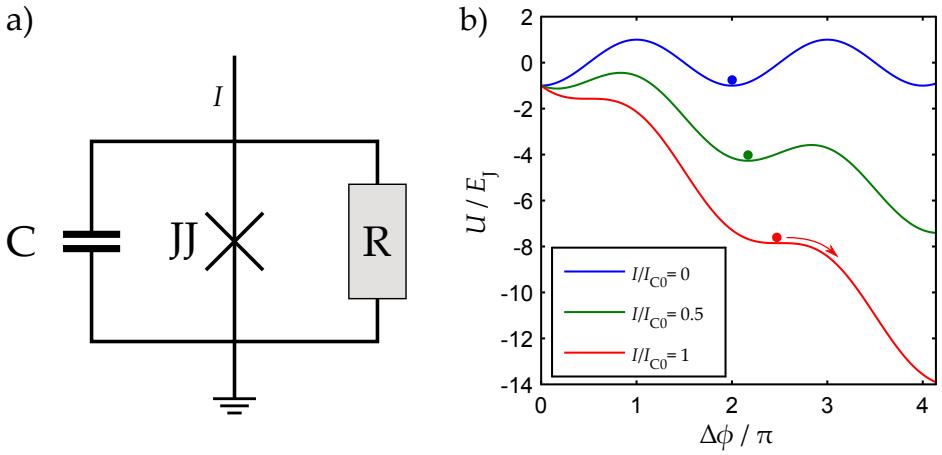

Figure 33: a) Equivalent circuit diagram describing a RCSJ. This extension to a Josephson junction also allows the description in the resistive (non-superconducting) regime. b) tilted washboard model for different currents I

Two more parts are included in the description: The resistance to describe dissipative transport in the non-superconducting regime and the capacitance between the two electrodes, which plays a role in the dynamic behavior of the junction. If all currents in the diagram are added up one receives the following:

$$I = I_{C0} \sin \Delta\phi + \frac{V}{R} + C\frac{dV}{dt}. \tag{43}$$

Using the second Josephson equation $\frac{d(\Delta\phi)}{dt} = \frac{2eV}{\hbar}$ [43], Eq. (43) can be converted to a second order differential equation in $\Delta\phi$ and is then solved by the so called tilted washboard model

$$U(\Delta\phi) = -E_J \cos(\Delta\phi) - \frac{\hbar I}{2e}\Delta\phi, \tag{44}$$

with the Josephson energy $E_J = (\hbar/2e)\, I_{C0}$. This model can be interpreted as a mechanical analogy of a particle being trapped in a potential. The potential $U(\Delta\phi)$ is shown in Fig. 33 b) for different currents flowing through the JJ. If no current is flowing ($I/I_{C0} = 0$) the "particle" is trapped in the potential and the JJ is superconducting. If however a current as high as the maximum critical current I_{C0} is flowing the "particle" can escape the potential and the supercurrent in the JJ is lost. Moreover if one includes the effect of temperature the additional thermal energy might allow the "particle" to escape the potential well even before I_{C0} is reached. As a result the measured critical current can also be smaller than the maximum critical current in the model $I_C \leqq I_{C0}$.

With this basic understanding of JJs the next section will focus on the measurement results of "Quad".

5.5 CURRENT BIASED JOSEPHSON JUNCTION

The simplest way to extract information from a JJ is to apply a current I and measure the corresponding voltage drop V, which is then called V-I measurement. The following curves have been recorded at a magnetic field of $B = 0$ T and a temperature of $T = 25$ mK, which is much lower than the temperatures in the discussion of the BTK model before.

In contrast to prior measurements the graphs shown in Fig. 34 are taken with extensive filtering, as indicated by the icons in the upper left corner. Now, with the important copper powder filters installed among others, the environmental noise is finally at a level, where induced superconductivity can develop. This can easily be seen in the center part, where current flow over the S/TI/S junction does not lead to a voltage drop. In the outher parts one observes the linear dependance of $V(I)$ as expected form a TI without the influence of the S.

In Fig. 34, there are two measurements superimposed: the red curve was recorded going from negative to positive currents and the blue curve was taken in the opposite direction. Both curves are point symmetric regarding ($I = 0$ A,$V = 0$ V). One obtains two critical values here. The switching current $I_C = 3.8$ µA, which is often just referred to as *the* critical current, is the maximum current value carried by the JJ, when going from the superconducting to the normal state. And the retrapping current $I_R = 2.5$ µA, which is the critical current value when going the other way round from the normal to the superconducting state.

Hysteresis can normally be found in underdamped JJs, which have a high resistance and capacitance. To check if this is actually the case one can have a look at the quality factor and plasma frequency [43]

$$Q = \omega_P R_n C, \quad \omega_P = \sqrt{\frac{2eI_{C0}}{\hbar C}} \tag{45}$$

in the RCSJ model. The capacitance can be estimated assuming a plate capacitor for the geometry of the Nb contacts. The height of the Nb contacts is $h_{Nb} = 90$ nm and the width is $w_{Nb} = 8.5$ µm. This also includes the part of the contacts, which is not on the mesa, but is still laying parallel on the device [see sample overview in Fig. 22 a)].

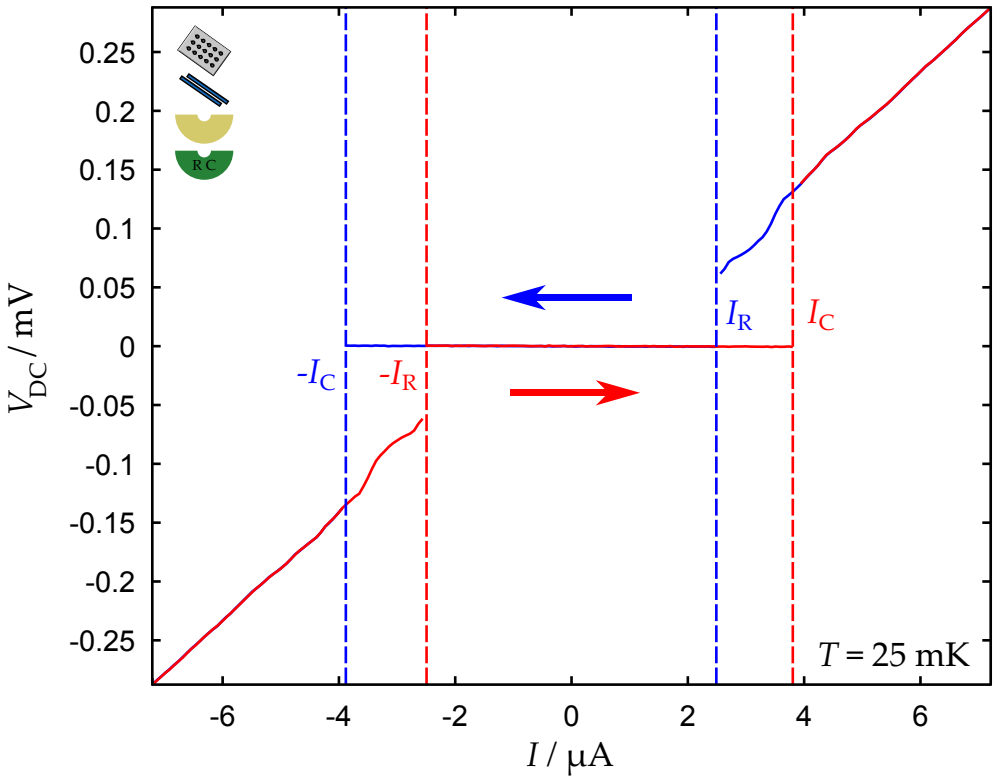

Figure 34: V-I curve of a 200 nm long JJ on "Quad" at a temperature of 25 mK. As indicated by the arrows the measurement has been taken in both directions. The hysteresis allows to extract the switching current I_C and the retrapping current I_R.

Together with the distance of the contacts $l_{JJ} = 130$ nm, which is the measured JJ length, including overexposure effects, the total capacitance is $C \approx \epsilon_0 h_{Nb} w_{Nb} / l_{JJ} = 52$ aF. In order to calculate Q one still has to extract the normal state resistance R_n. This can most accurately be done far away from the superconducting area with $V_{DC} = 0$ V. A wider current range is plotted in Fig. 35. Two linear fits to the V-I curve result in an average slope, and thus equivalently in a resistance of $R_N = 52\ \Omega$. With the assumption that the switching current does not deviate much from the theoretical maximum critical current $I_C \approx I_{C0}$ one can calculate the quality factor $Q = 0.016$. An underdamped and thus hysteretic JJ needs to satisfy $Q > 1$, which is not the case here. As a consequence the hysteresis must have a different origin.

The next step is to look at the temperature. The thermal energy of the lattice is $E_{Th}(25\,\text{mK}) = 2\,\mu\text{eV}$. One can compare this to the potential size, which is given by the Josephson energy $E_J = (\hbar/2e)\, I_{C0} = 49$ meV. The ambient temperature is not high enough to have a significant influence on the JJ, but the current flow in the resistive regime leads to self heating, which can increase the electronic temperature. The power density of the junction is estimated to $p = P/V_{Surf} = I_R V_R / V_{surf} \approx 10$ nW, with the

retrapping voltage V_R and the volume occupied by the surface states $V_{surf} \approx 0.01\ \mu m^3$. Compared to Ref. [74] this suggests that the reason for the hysteresis is indeed the self heating of the junction. This additional thermal energy leads to a delayed transition into the superconducting state at I_R instead of I_C.

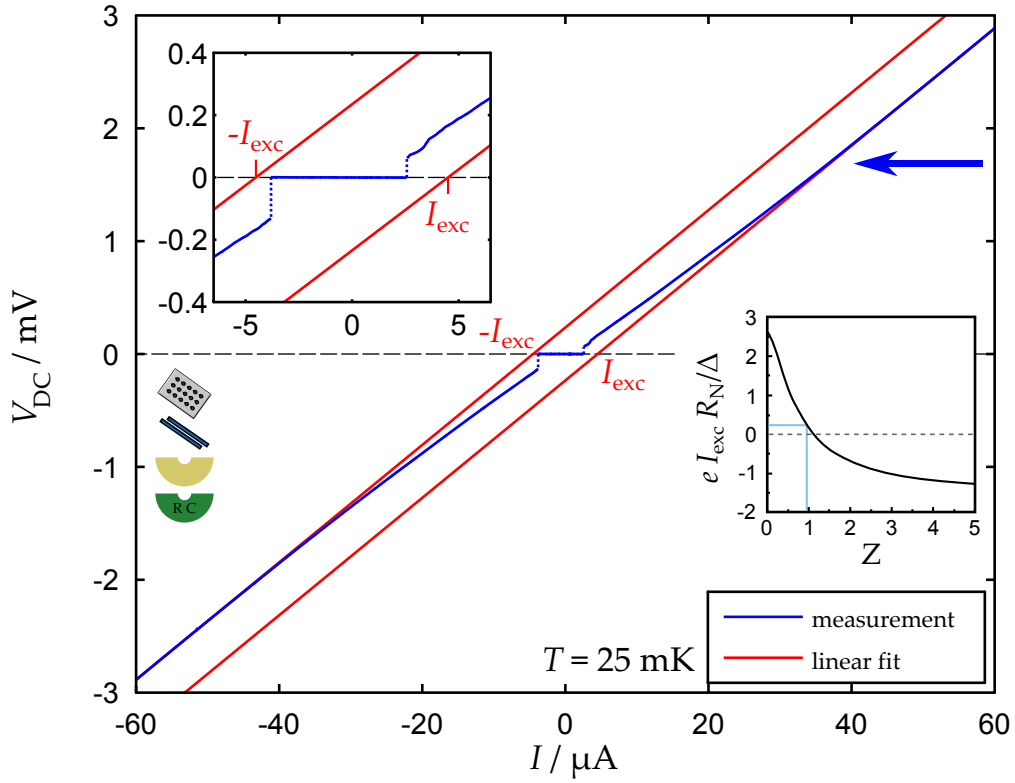

Figure 35: V-I curve of a 200 nm long JJ on "Quad" plotted over a wider current range. The upper left inset shows a magnified plot of the central part showing the size of the excess current I_{exc} more clearly. The lower right inset is redrawn after [75] and displays the conversion between the normalized insufficient voltage $eI_{exc}R_N/\Delta$ and the barrier Z.

Due to the occurrence of induced superconductivity in "Quad" one could not estimate a barrier parameter Z from the basic BTK model. However alternatively the same value can be extracted using the excess current I_{exc} (see Fig. 35). This current is obtained by linearly fitting the V-I curve of a JJ far off the critical current $I \gg I_C$ and extrapolating the result back to $V = 0$ V. This procedure yields $I_{exc} = 4.5\ \mu A$ and, as mentioned above, the normal resistance $R_N = 52\ \Omega$. By combining both and normalizing them to the band gap of Nb one can calculate the normalized insufficient voltage $eI_{exc}R_N/\Delta = 0.23$. This value can be converted into the barrier strength with the calculations done in [75]. The needed graph is shown in Fig. 35 on the right. The resulting barrier is $Z = 0.9$ and thus the smallest of the barriers so far. This establishes,

that "Quad" is the lithographically most advanced sample, with the highest Andreev probabilities, as expected from the prior discussions of the BTK model.

Another characteristic value used to qualify JJs is the $I_C R_N$-product. For short junctions one expects the value of $I_C R_N$ to be in the range of Δ/e. For longer junctions the product is limited by the Thouless energy E_{Th} [see Eq. (26)] [76]. Here one recieves $I_C R_N = 0.2$ mV, which is five times smaller compared to the superconducting gap of Nb $\Delta/e = 1$ mV. As a conclusion the long junction limit might be appropriate for the present case with the superconducting coherence length ξ being smaller than the actual junction length of $l = 130$ nm. Alternatively the the $I_C R_N$-product can also be reduced due to limited interface transparency [77].

To be able to resolve changes in the resistance of the JJ with a higher resolution dV/dI measurements are conducted. The inset in Fig. 36 shows the transition from the normal conducting state to the superconducting state and back again in the narrower current range (comparable to Fig. 35). As the discussion will now focus on the energies in the system the main curve in Fig. 36 is plotted against the DC-voltage drop V_{DC} over the junction instead of the current. To separate the different transport regions the plot is divided into several colored parts, which are, neglecting the hysteretic effect in the superconducting regime, symmetric around $V_{DC} = 0$ V.

The most outer region in red develops a slightly decreasing resistance, which is due to the increased density of states just above the superconducting band gap Δ. Due to the layer structure S/TI/S, meaning two S/TI interfaces in a row, one expects this effect to show up at a voltage close to and above $V_{gap} = 2\Delta/e$.

Below V_{gap}, in the so called sub-gap region, the resistance is falling faster (green), which indicates an enhanced transport mechanism. Because of the high transparency Andreev reflection probability increases and hence transfers more charge over the interface. Interestingly one observes a plateau at the value of Δ/e, which can be associated with the appearance of a 3-fold Andreev reflection by applying Eq. (41) [78, 79]. Higher multiple Andreev reflections are not properly resolved as a plateau, but show a decreasing resistance. The appearance of this effect indicates, that the HgTe moderating the superconductivity between the two Nb contacts has a phase coherence length longer than the junction length.

The next regime is marked in blue and reveals a strongly oscillating behavior. These oscillations will be discussed in detail later in Sec. 5.7. Finally at low bias voltages the system reaches the superconducting regime, where the resistance drops to zero. Com-

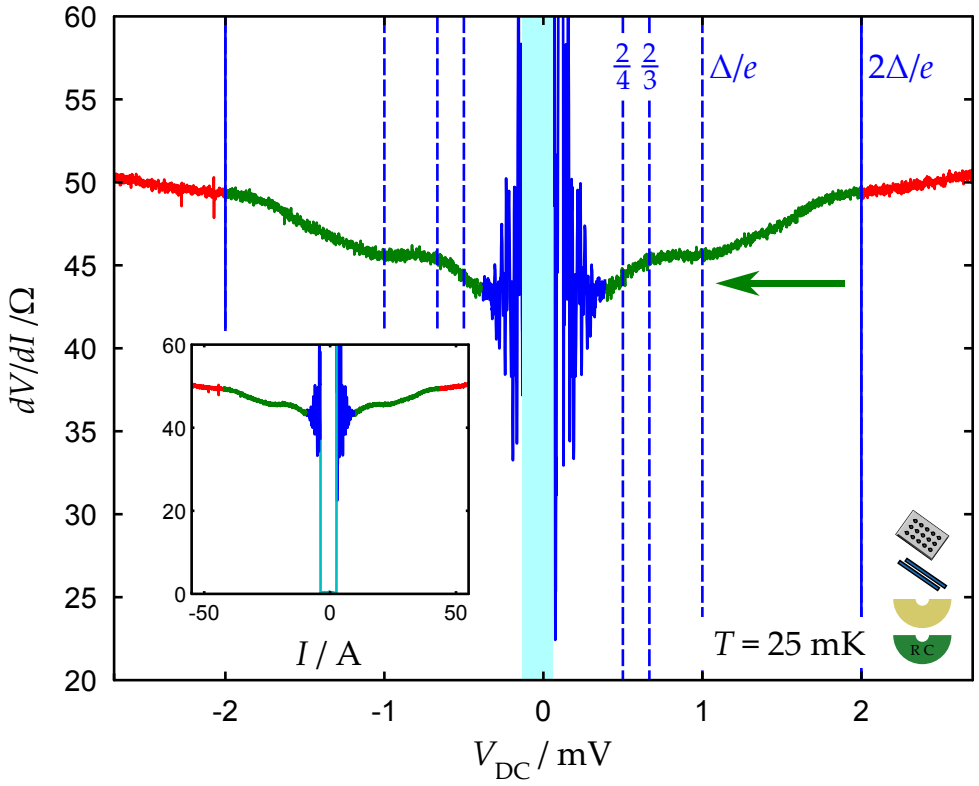

Figure 36: dV/dI measurement plotted against the applied DC-voltage V_{DC}. For better visibility the graph is color coded into four sections: above the gap of Nb (red), below the gap in the region of Andreev reflections (green), the oscillations (blue) and the superconducting region (cyan). The inset shows the same data plotted against the current for better visualization of the superconducting region.

pared to the previous DC-measurements, no additional information can be gained here.

However one can extract more information from temperature dependent measurements as seen in Fig. 37. With increasing temperature the switching current I_C decreases much faster than the retrapping current I_R. This is to be expected, as the increase of thermal energy is a major contribution to the overall energy at I_C, while the thermal energy at I_R is already enhanced due to Joule heating at the interfaces, as described above.

This behavior is even more visible if I_C and I_R are plotted against the temperature (see Fig. 38).The induced superconductivity starts to appear at 4.5 K, where both critical currents are equal. Only after reaching a temperature below 1.2 K the two values start to differ, indicating that the overall thermal energy in the system is now low enough and the Joule heating is becoming the dominant thermal effect limiting I_R.

When compared to Ref. [80] the shape of the temperature dependent critical current indicates that the transport over the junction is in the clean or Eilenberger limit [81]

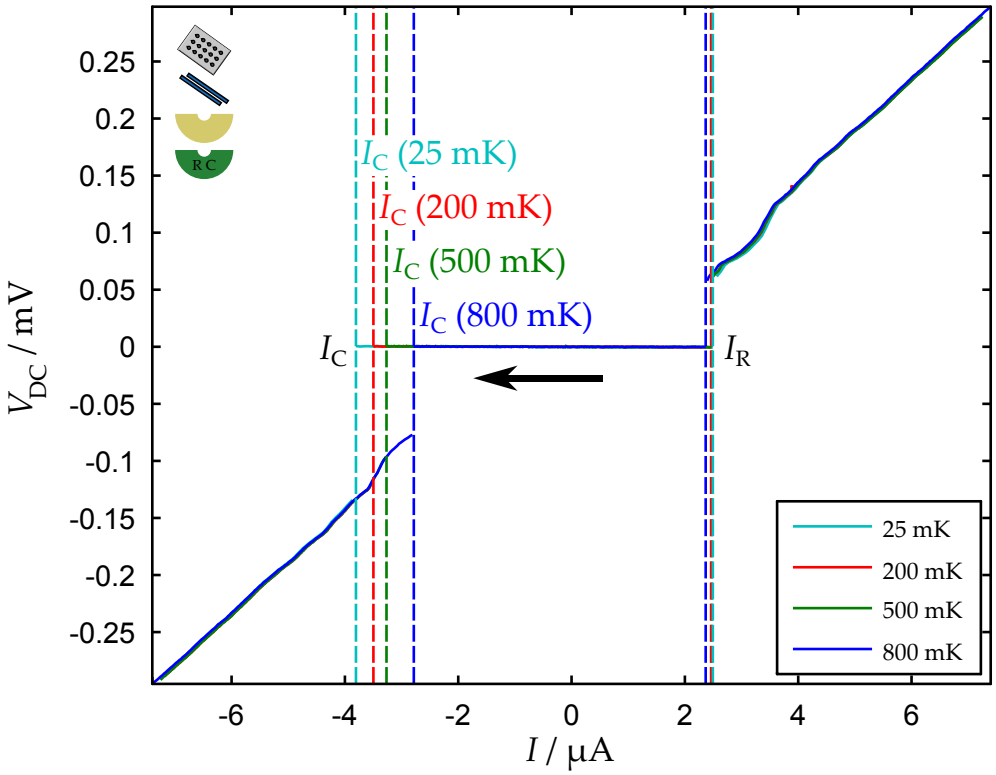

Figure 37: *V-I* curve of a 200 nm long JJ on "Quad" shown for four different lattice temperatures. The switching current I_C is falling much faster with increasing temperatures.

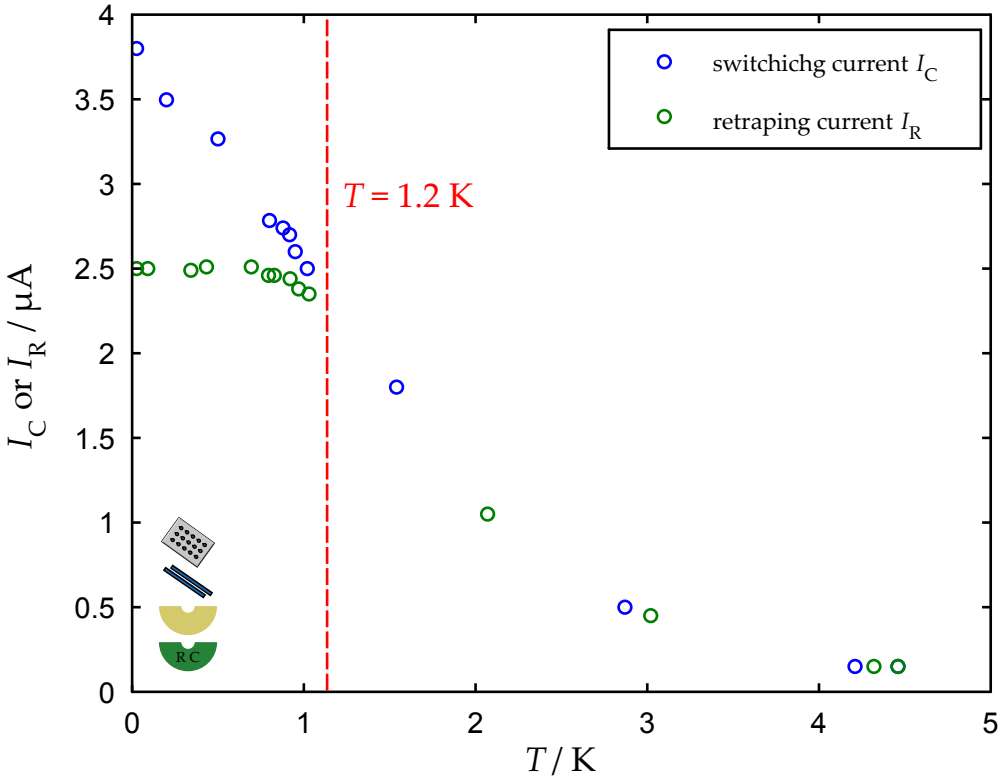

Figure 38: The switching current I_C and the retrapping current I_R plotted against temperature T.

where $l_e \gg \xi, L$, with the mean free path l_e, the coherence length ξ and the JJ length L. To estimate l_e one can use the transport data gathered from measurements on a sample in Hall geometry made from the same HgTe layer. The Drude model allows to calculate [82]

$$l_e = v_F \tau = \frac{\hbar k_F}{m_e} \frac{m_e \mu}{e} = \frac{\hbar k_F \mu}{e} \tag{46}$$

from the Fermi velocity v_F and the mean scattering time τ. The Fermi momentum $k_F = \sqrt{4\pi n}$ can be calculated from charge carrier density n. The values for sample "Quad" are $n = 5.5 \cdot 10^{11}$ cm^{-2} and the mobility $\mu = 26 \cdot 10^3$ cm^2/(Vs). This results in a mean free path $l_e = 451$ nm, which is indeed bigger than the JJ length. Nevertheless one has to be careful, as this value does not properly consider all topological features of the HgTe layer as well as the different lithographic treatment of the superconducting sample. Both those effects could change l_e and therefore this result can only be seen as a rough estimate.

The measurements presented so far can clearly establish, that it is possible to induce superconductivity in the 2-dimensional surface state of the 3-dimensional TI HgTe. This is a first big step towards the realization of a zero energy Majorana mode. In order to be able to verify the presence of such a mode the junction has to be studied further.

5.6 MAGNETIC DEPENDANCE

For a closer investigation of the properties of a S/TI/S junction the magnetic dependance will be studied in this section. In order to include the effect of the magnetic field one has to generalize Eq. (42), which is only valid if the area of the JJ itself is neglected.

Figure 39 shows the layout of the JJ with the two Nb electrodes A and B, which are separated by the JJ length l. The field is applied in y-direction and the current I is flowing in z-direction.

To calculate the total critical current I_C the critical current density J_C needs to be integrated over the junction area [43]:

$$I_C = \iint J_C(x,y) \sin(\gamma(x))\, dxdy. \tag{47}$$

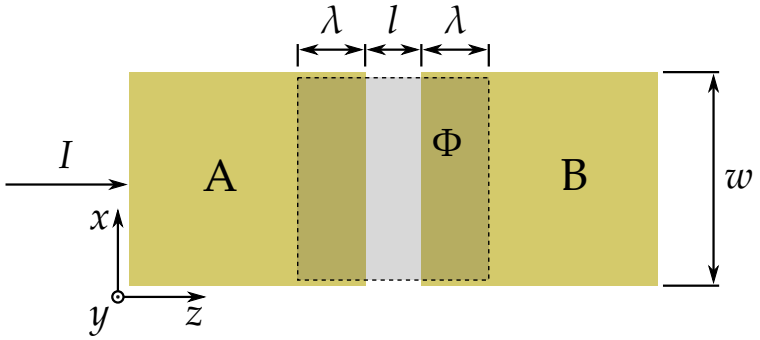

Figure 39: Schematic drawing of the dimensions of a JJ with the magnetic flux Φ penetrating the effective junction area.

The term $\sin(\gamma)$ assumes a usual current phase relation normally visible in non-TI materials. The effect of the TI will be discussed later.

As the system at hand only has a 2-dimensional conducting area in the xz-plane the integration in y-direction only reduces the dimension of the problem, with $\tilde{J}_C(x) = \int J_C(x,y)dy$.

To solve Eq. (47) the influence of the magnetic field B has to be included in the phase additionally to $\Delta\phi$ in the form of $\gamma(x) = \Delta\phi + \gamma_B(x)$. If the electrodes are thicker than the London penetration depth of bulk Nb $\lambda_{Nb} = 39$ nm [83], which is the case here, the phase difference between two current paths can be directly calculated from the enclosed flux of these paths. The complete flux in the junction is $\Phi = \boldsymbol{BA}$, with the effective area of $|\boldsymbol{A}| = w(l + 2\lambda)$. This not only includes the geometric area, but also the additional size due to the penetration of the magnetic field into the Nb by a length of λ on both sides (See Fig. 39).

If there are two parallel tunneling paths in z-direction separated by a distance Δx, then only a part $\Delta\Phi$ of the total flux is enclosed resulting in a phase shift

$$\gamma_B(\Delta x) = \frac{\Delta x}{w} 2\pi \frac{\Phi}{\Phi_0}, \tag{48}$$

with the magnetic flux quantum $\Phi_0 = h/2e$. Using the information listed so far one can solve Eq. (47) by assuming a homogeneous current density $J_C(x,y) = J_C$ over the JJ. The resulting distribution of the maximum critical current is then given by

$$\frac{I_C(\Phi)}{I_C(0)} = \left| \frac{\sin(\pi\Phi/\Phi_0)}{\pi\Phi/\Phi_0} \right|. \tag{49}$$

Because of the similarity to the optical phenomenon of passing light through a narrow single slit, this intensity distribution is referred to as Fraunhofer diffraction pattern. Eq. (49) is visualized in Fig. 40 a).

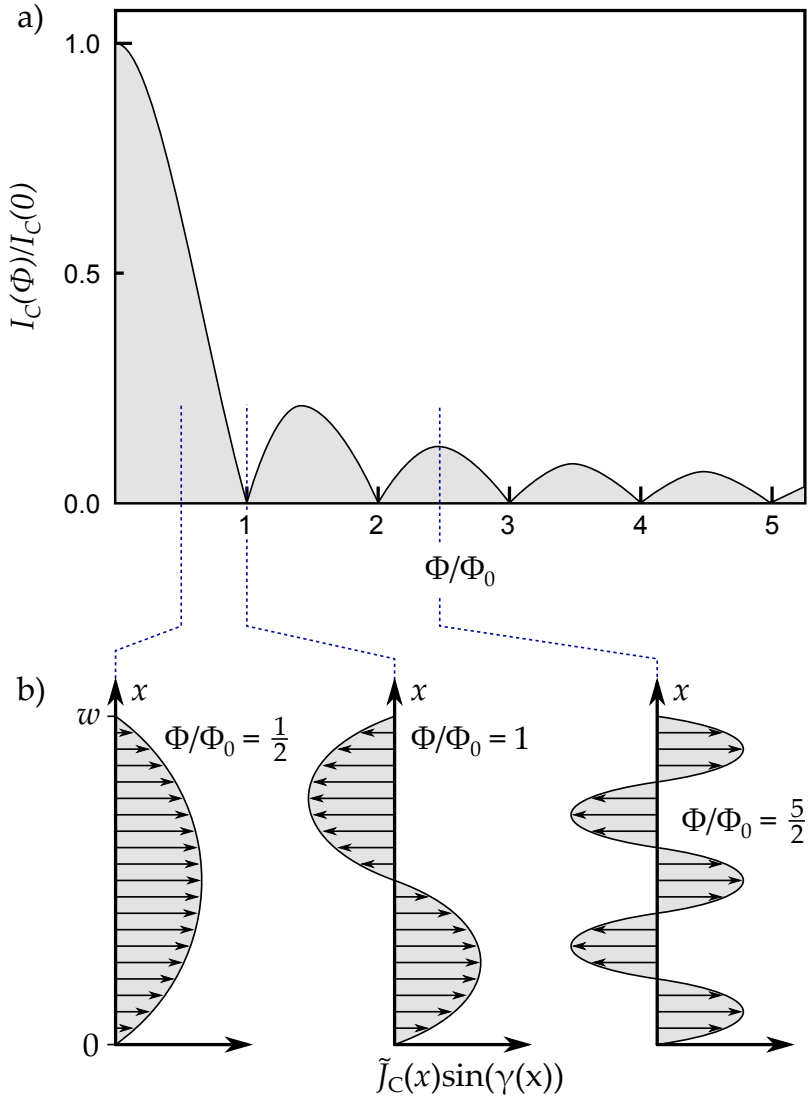

Figure 40: a) Fraunhofer pattern expected from a S/N/S junction dependent on the penetrating flux Φ. b) spacial current distribution in the junction for $\Phi/\Phi_0 = \frac{1}{2}$, 1 and $\frac{5}{2}$.

One can see, that the critical current is at its maximum when the flux $\Phi/\Phi_0 = 0$ and thus the y-component of magnetic field $B_y = 0$ T. This property has been used to find the maximum critical current of the devices, without being able to exactly detect the zero field value, due to the hysteretic behavior of the superconducting magnetic coil. With this technique, it can not be ruled out, that there are small field contributions in the xz-plane, as the JJ only picks up the field component in y-direction. Still the influence should be small enough to be negligible.

For a deeper understanding of the current flow in the JJ with an applied flux, it is helpful to look at the spatial distribution $\tilde{J}_C(x)\sin(\gamma(x))$. In the case, where half a flux quantum is present in the junction the phase shift due to the field lies between 0 and π in the range from $x = 0$ to $x = w$ [see Fig.40 b) left], giving a positive, but already reduced current compared to no flux. Every time the flux reaches $\Phi = n\Phi_0$, with $n = 1, 2, 3, \ldots$ the total critical current is zero, as the spacial current has equal amounts running in both directions [see case $\Phi = \Phi_0$ in Fig. 40 b) middle]. In between those regions the net current is positive as shown for $\Phi = \frac{5}{2}\Phi_0$ in Fig. 40 b) right, but the maximal reachable current becomes smaller due to a higher amount of current running in the opposite direction. This visual picture of current distribution will later help to interpret the changes in the ideal Fraunhofer diffraction pattern.

The samples examined consist of S/TI/S junctions and the topological insulator is expected to influence the behavior of the junction in comparison to a S/N/S junction. The most prominent publication on this subject by Fu and Kane [15] suggests that the s-wave superconductor in combination with the TI changes the transport properties of the junction, allowing it to host zero energy Majorana modes. The actual Andreev bound state spectrum in the JJ geometry was calculated by [69], which shows that the zero energy mode has an unusual current phase relation with a periodicity of 4π instead of the usual 2π coming from the sine function in Eq. (42). This should stretch the appearing Fraunhofer pattern [see Eq. (49)] by a factor of two compared to the regular occurring pattern. These theoretical predictions can now be analyzed in comparison to the measurements.

In order to extract the magnetic dependance of the system the I-V-measurement conducted in Fig. 34 is repeated in one direction at different field values. The measurement direction is indicated by the red arrow in Fig. 41. The measured data is processed further to enable better visualization as a 2D color plot. Each single I-V-curve at a fixed magnetic field is convolved with the function

$$y(x, \sigma) \propto x \exp\left(\frac{x^2}{2\sigma^2}\right). \tag{50}$$

This function is point symmetric to $(0, 0)$ and has a negative maximum below $x = 0$ as well as a positive one above. The convolution with a Gaussian multiplied by x has two effects. The measurement is on the one hand smoothed and on the other differentiated at the same time. The strength of the smoothing is controlled by the parameter σ. This operation results in the numerically calculated differential resistance.

The absolute value of it is then plotted in Fig. 41 as the gray scale. In black areas the differential resistance is zero. This can be seen equivalently as areas where the JJ is superconducting, whereas in all other areas the system is in the resistive regime.

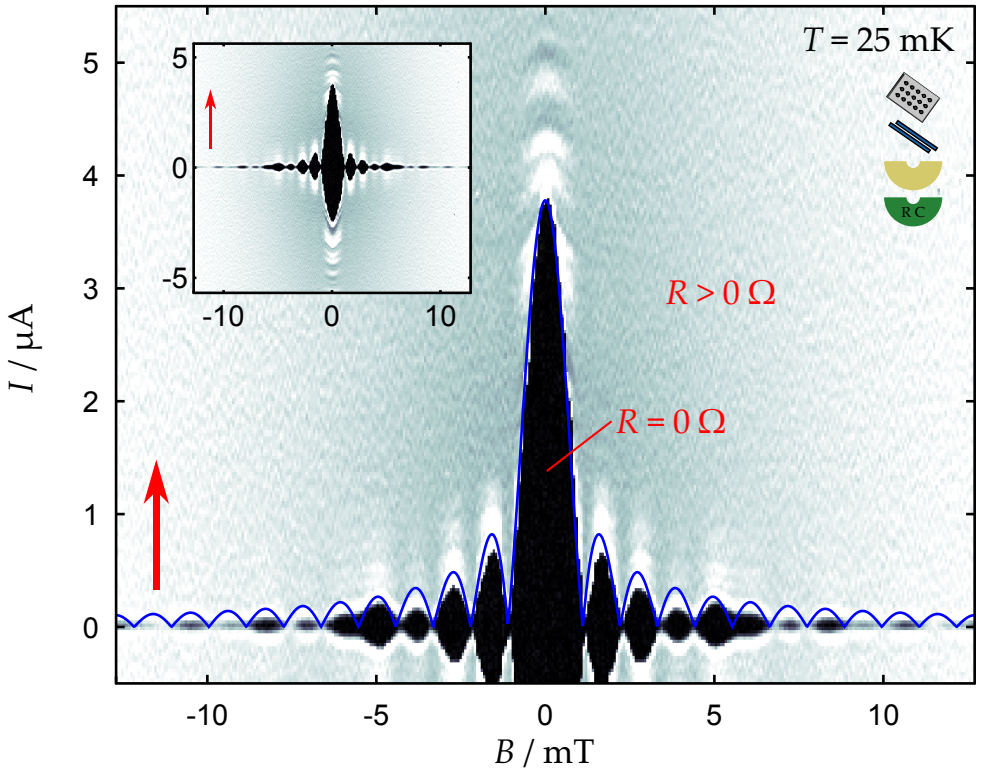

Figure 41: Magnetic and current bias dependance of the JJ. The color scale shows the absolute of the numerically calculated differential resistance. Superconducting areas ($R = 0\ \Omega$) are shown in black. The red arrows indicate the measurement direction. The inset shows the whole measurement range, which allows the comparison between the switching and retrapping current. The blue fit in the main plot is the ideal Fraunhofer pattern as described by Eq. (49).

The inset in Fig. 41 shows the whole current range with the difference between switching and retrapping current visible. To compare the measured data to the theoretical predictions made so far, the switching current is fitted with an ideal Fraunhofer pattern in the main plot (see Fig. 41 blue curve). The fitting parameters used are $I_C = (3.8 \pm 0.1)$ μA and the periodically appearing distance between two neighboring minima $B_P = (1.08 \pm 0.03)$ mT. The critical current extracted here is equivalent to the single measurement shown in Fig. 34. The periodicity of the Fraunhofer fit seems to be consistent with the measurement, but the amplitudes are not. Still the amplitudes are symmetric around $B = 0$ mT, which shows that there is no problem with unwanted strong magnetic disturbances, like flux trapping, as seen in other measurements, not shown here.

The periodicity allows to extract the effective area of the junction by using $\Phi = \boldsymbol{AB}$, which in scalar form and at the first minimum can be written as $A_{\mathrm{JJ}} = \Phi_0 / B_{\mathrm{P}} = (1.91 \pm 0.05)\ \mu\mathrm{m}^2$. The width of the JJ is well defined by the etched mesa and has a value of 2 µm (the overexposure is to small to have an effect). Assuming a rectangular area one obtains a length of $l_{\mathrm{JJ}} = (0.96 \pm 0.03)$ µm. The length is divided into the geometrical length $l = 130$ nm (with overexposure taken into account) and the London penetration depth λ on both sides, as shown in Fig. 39. This would lead to $\lambda = (l_{\mathrm{JJ}} - l)/2 = (0.42 \pm 0.02)$ µm for the periodicity of the field. Compared to the thin films measured in [84] this is higher, but explainable due to the dirtier environment during sputtering, caused e.g by carbon impurities from the PMMA resist. The oscillations visible in Fig. 36 are also visible here, as areas of strongly changing slopes (white areas) above each maximum. For further discussion see Sec. 5.7.

So far a 2π periodicity was assumed in the phase dependence of the JJ [see Eq. (47)]. Due to the theoretical predictions [15, 18] one could also be looking at a measurement with 4π periodicity. In this case the first minimum would be at $2\Phi_0$ and consequently the effective area would be $A_{\mathrm{JJ},4\pi} = 2\Phi_0 / B_{\mathrm{P}}$. Following the calculations above, this would give a London penetration depth of $\lambda_{4\pi} = (0.89 \pm 0.03)$ µm, which would be more than half of the 1 µm long Nb contacts. Therefore the contact could no longer be superconducting. As a result the measurement has to have a 2π period. This rises two questions: Why are there deviations from the ideal Fraunhofer pattern and why is there no 4π periodicity?

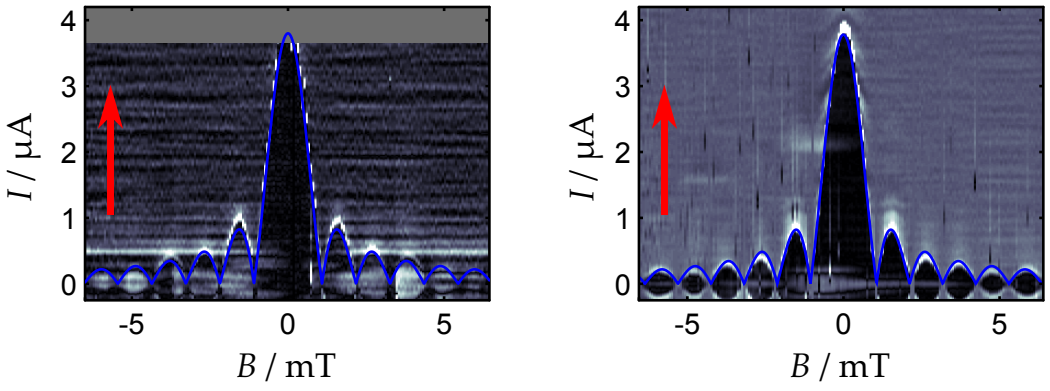

Figure 42: Fraunhofer pattern of two JJs measured in 3-point geometry on sample "Quad". The additional, unwanted resistance has been subtracted. The red arrow indicates the measurement direction and the blue curve is a fit of an ideal Fraunhofer pattern. The left measurement does not fully reach the tip of I_{C} (upper gray part missing).

In order to further study the deviations it is useful to have a look at several JJs. In the case of sample "Quad" there were four geometrically identical Josephson junctions

manufactured and three of those were functional. Due to disconnected wires, two of those three could only be measured in a 3-point configuration, which resulted in a big additional resistance in the wiring. The graphs in Fig. 42 show the results after the additional resistance is subtracted. Due to this treatment the color coding can no longer be properly interpreted as in Fig. 41. But despite the higher noise level in these measurements one can still clearly identify the Fraunhofer pattern. As the measurements are recorded in the same direction (red arrows) these shapes can be directly compared to the measurement above. The values of all three fits are compared in Table 1. They are all almost identical, allowing to deduce that all three JJs are comparable in geometry, as well as in transparency, which is needed for this critical currents. The increased uncertainty of the critical current in Fig. 42 left can be explained, by the cutoff of the Fraunhofer pattern at $B = 0$ T, which does greatly increase the uncertainty of its value. This comparison shows that the lithographic process, even if not in the ideal state, allows very reproducible, uniform results.

	$I_C/\mu m$	B_P/mT
Fig. 41	3.8 ± 0.1	1.08 ± 0.03
Fig. 42 left	3.8 ± 0.4	1.09 ± 0.02
Fig. 42 right	3.8 ± 0.1	1.06 ± 0.01

Table 1: Comparison of critical current I_C and magnetic periodicity B_P of three JJs on sample "Quad"

If one also compares the amplitudes of the minor maxima of all three measurements in Figs. 41 and 42 all three devices show different variations. As an example, the local maximum at $B = 5$ mT can be bigger than its neighbors (Fig. 41), comparable to the fit (Fig. 42 left) or smaller than expected (Fig. 42 right). This variations can be explained by a non uniform distribution of the current density, which then in turn leads to the resulting deviations from an ideal Fraunhofer pattern [see Eq. (47)]. The variations could stem from crystalline imperfections in the HgTe layer or local variations of the contact transparency over the contact area.

The second question was the missing 4π periodicity. Looking at the Andreev bound state spectrum calculated in Ref. [69] the wanted 4π periodicity can be reverted to a 2π periodicity by several factors. The first is the momentum k_x perpendicular to the junction, which needs to be exactly zero. Otherwise the Andreev spectrum gets gapped and the zero energy state no longer exists. The size of this gap depends on the junction length. Accordingly longer junctions are more easily and more strongly gapped

than shorter ones. Another factor is the temperature, which has to fulfill $k_B T \ll e\Delta$, which holds true at 25 mK for the lattice temperature. The electronic temperature is expected to be higher and still could constitute a problem, that should be solved by further developing the filtering system. One also has to take into account that even if a Majorana mode is present in the system, depending on the size, several other 2π periodic modes with $k_x \neq 0$ are present at the same time. The amount of modes N allowed in the system due to the JJ width w_{JJ} can be estimated with the following two equations [82]:

$$k_F = \sqrt{4\pi n} \quad \text{and} \quad k = \frac{2\pi N}{w_{JJ}}. \tag{51}$$

Assuming that the momentum of the highest occupied state fulfills $k = k_F$, one gets $N = 60$, with $w_{JJ} = 2$ µm and the density $n = 2.8 \cdot 10^{11}$ cm^{-2} (see Appx. A.1). The density used here is estimated as half the density of the full system, due to the upper surface of the TI being expected to dominate the transport in the JJ. This shows that there might even be a zero energy mode present, but is not detectable due to the amount of other modes being responsible for the majority of the transport over the junction.

In conclusion one can say that in order to increase the chances of detecting a Majorana mode in future samples the width of the junction should be reduced, to decrease the total amount of modes. The length of the JJ has to be decreased or alternatively the coherence length needs to be increased to reduce the chance of a gap formation. The possibility of increasing the coherence length by using capped HgTe will be dicussed in Sec. 5.8.

5.7 OSCILLATORY BEHAVIOR ABOVE THE CRITICAL CURRENT

The appearance of the induced superconductivity in the JJ was accompanied by a oscillatory behavior in the resistive regime just above the superconducting state. This effect was already visible in the voltage bias measurement shown in Fig. 36 as well as the magnetic dependent voltage bias measurement in Fig. 41.

The situation for $B = 0$ T is shown in Fig. 43. In order to be able to compare the symmetry of the phenomenon in voltage drop over the junction V_{DC} the data are displayed for decreasing voltages in Fig. 43 a) (see black arrow) and increasing voltages in Fig. 43 b). It is clearly visible that, even though the oscillations do not show

a clear periodicity, they are symmetric around $V_{DC} = 0$ V. Temperatures in the range from 25 mK to 800 mK do not influence the amplitude or position of the oscillations. This is not too surprising as the Joule heating in the junction was the dominant source of heat in the resistive regime below 1.2 K (see Fig. 38). As a result the increase in lattice temperature is not the main influence. However one can see the effect of the lattice temperature on the switching current in Fig. 43 b).

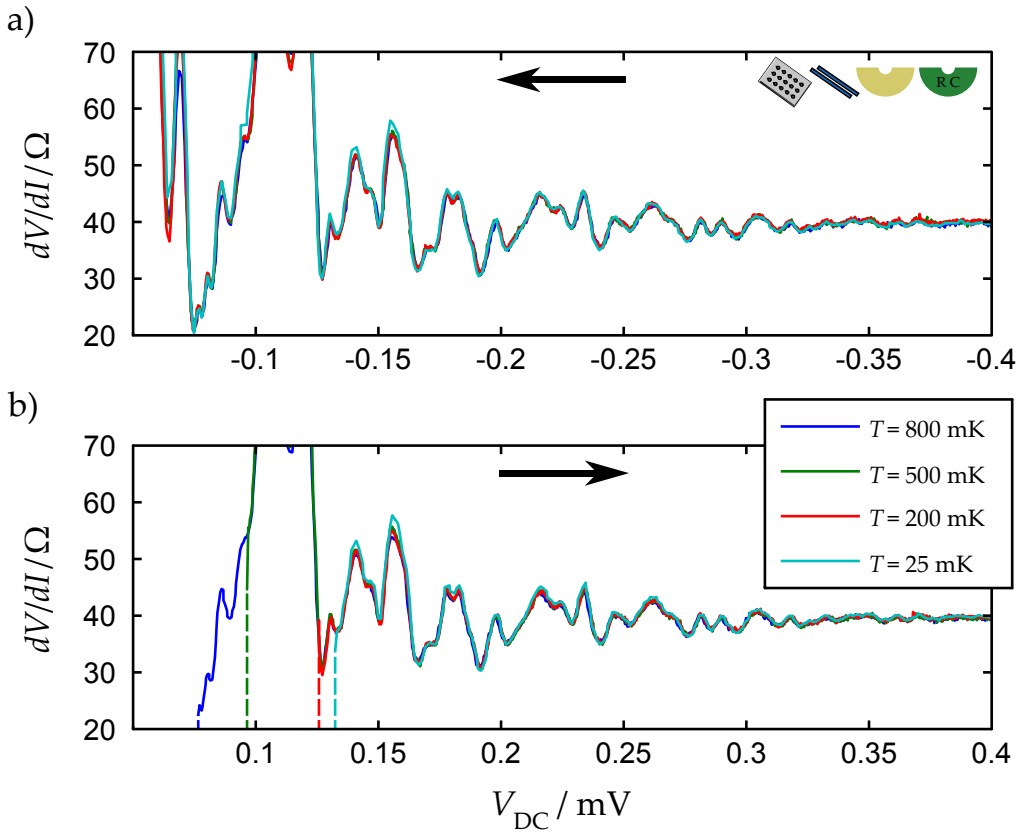

Figure 43: dV/dI measurement over the 200 nm JJ at zero magnetic field for different temperatures. The positive and negative side is compared for symmetry. The measurement direction is indicated by the black arrow. Temperature influence can only be seen in the change of the switching current in b).

The influence of a magnetic field can be clearly observed in Fig. 44. Here the development of the system from $B = 0$ mT, with maximum critical current, to $B = 1.1$ mT, the first minimum with zero critical current, is presented. Once more the position of the peaks does not move and thus the defining energy scale seems not to be influenced by magnetic field.

What however does change, is the amplitude. Figure 45 a) displays the development of the amplitude of the peak at $V_{DC} = 0.146$ mV (see Fig. 44) with increasing magnetic field. Right next to it the development of the critical current is plotted in Fig. 45 b)

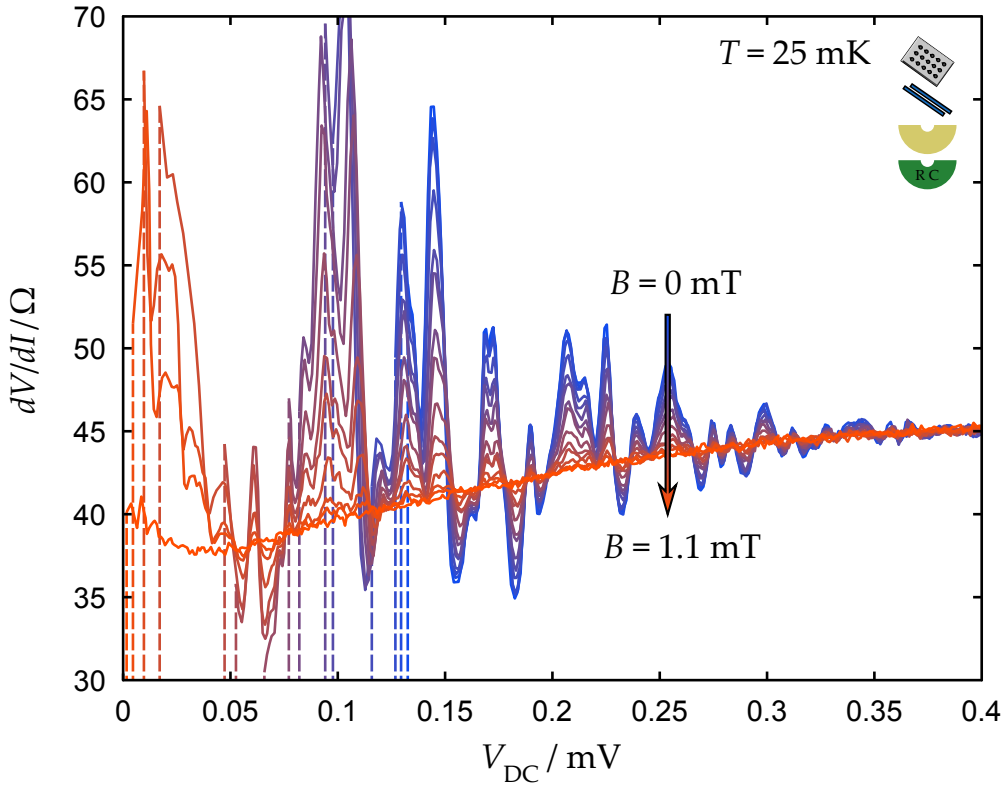

Figure 44: Magnetic dependance of the junction shown in Fig. 43. The amplitude of the oscillations is maximal at the maximum of $I_C(B = 0\ \mathrm{mT})$ and vanishes if $I_C(B = 1.1\ \mathrm{mT})$ vanishes.

for comparison. One can see that, neglecting the baseline of 41 Ω, both graphs show a similar decreasing behavior.

Periodic oscillatory behavior has been detected in Sn based tunnel JJ in 1964, and was attributed to the AC Josephson effect [85]. A more detailed analysis has been done in Ref. [86], where similar oscillations in Al microbridges could be attributed to the electromagnetic coupling of the AC Josephson effect to the sample surrounding, which in turn led to self induced Shapiro steps. This could also be the case here.

In a system closer related to ours, a Nb/InAs-2DEG/Nb Josephson junction, similar oscillations have been observed [79]. A InAs-2DEG has no inverted band structure and thus is no topological insulator. The appearance in a topological as well as a non-topological semiconducting 2-dimensional system additionally suggests that it is not related to the special properties of a TI and thus does not help for the deeper understanding of the properties of a S/TI/S junction.

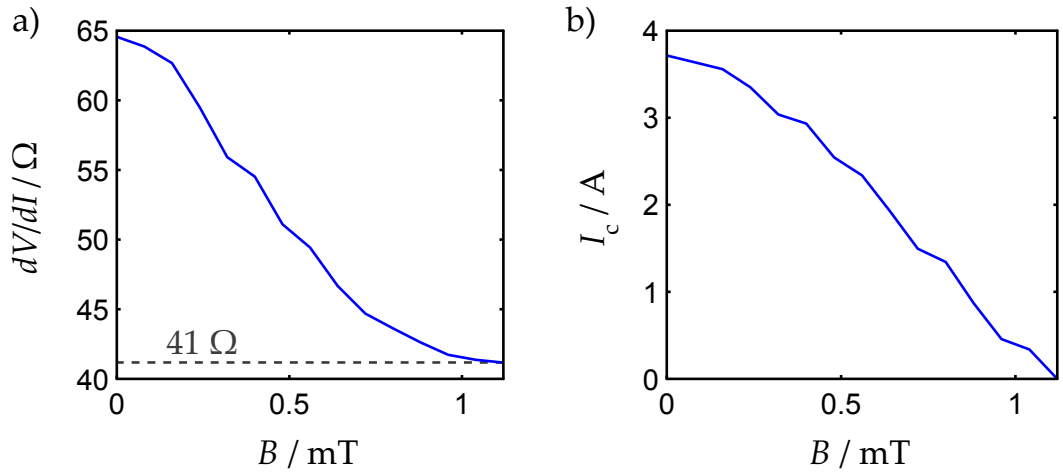

Figure 45: a) amplitude of the peak at $V_{DC} = 0.146$ mV in Fig. 44 for increasing magnetic field. b) maximum critical current in the equivalent field range.

5.8 JOSEPHSON JUNCTIONS WITH CAPPED HGTE

Finally the aspect of capped HgTe in a Josephson junction is discussed. The sample Q2573 #1 SQUID_V "Shade" consists of two JJs and two SQUIDs. It would have been better to directly compare different Josephson junctions with each other, but in this case both produced JJs were damaged and not usable for measurements. Consequently the SQUID, which acts as two parallel JJs at zero magnetic field, was used for comparison.

The motivation to use a 5 nm HgCdTe layer as cap on top of the conducting HgTe layer originates in the observation of an overall cleaner system due to this protective layer and thus in a reduction of unwanted influencing factors. These factors are oxidization of the upper surface as well as contamination by lithographic treatment. The statement of a cleaner system due to the cap is reflected in the strong increase of mobility ($188 \cdot 10^3$ cm^{2}V^{-1}s^{-1} compared to $26 \cdot 10^3$ cm^{2}V^{-1}s^{-1} in "Quad") of the HgTe layer allowing to measure samples which are clearly in the Eilenberger limit ($l_e \gg L$). Of course assuming that the preparation of the Nb contacts does not influence the crystalline quality of the sample.

The critical current of this device is $I_C = 0.5$ µA, which is carried by the two parallel JJs with a width of 500 nm each. In comparison to that sample "Quad" had a critical current of $I_C = 3.8$ µA and a junction width of 2 µm. This means, taking junction widths into account, one should expect a critical current of 1.9 µA for "Shade". To better understand the decreased critical current of this double junction a more detailed discussion is needed.

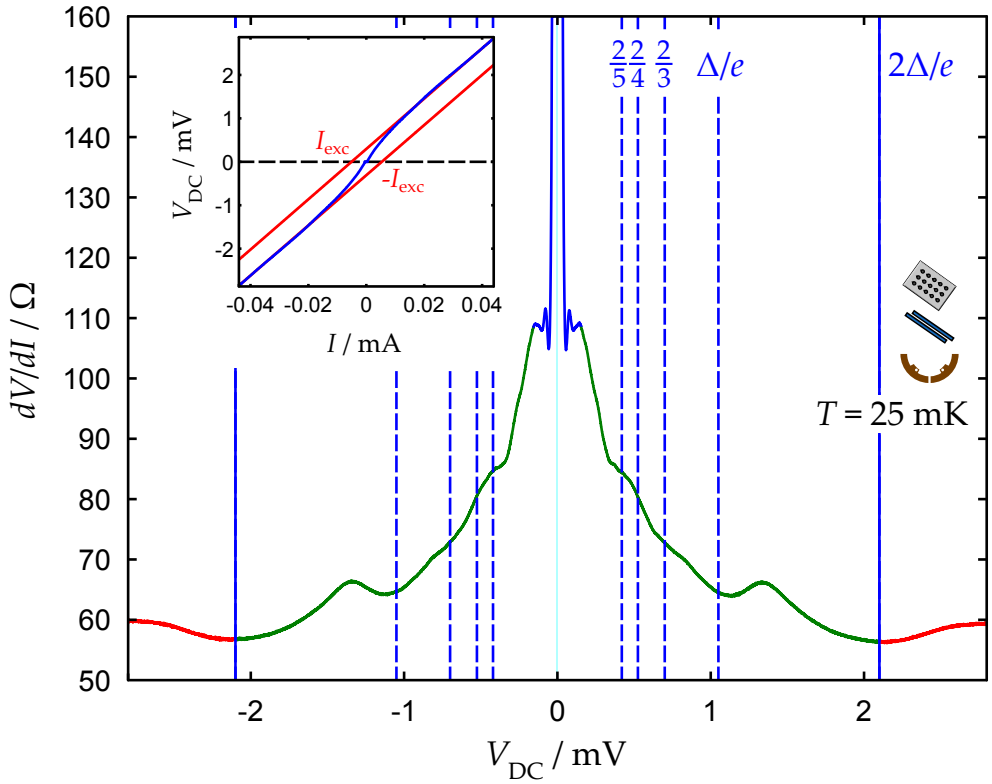

Figure 46: dV/dI measurement plotted against the applied DC-voltage V_{DC}. The color coding is equivalent to Fig. 36. Due to the small critical current the superconducting area is almoust not visible at the plotted scale. The inset shows the excess current of the device, which in this case is negative.

A voltage dependent dV/dI measurement is shown in Fig. 46. This graph is equivalent to Fig. 36 of sample "Quad". In the sub gap structure (green) not only the plateau for the 3-fold Andreev reflection at Δ/e is visible, as it was in the uncapped sample "Quad", but also higher order reflections. This shows that the phase coherence length is significantly increased due to the introduction of the cap.

But in contrast to "Quad" the differential resistance increases below the superconducting band gap of $2\Delta/e$. One would expect that the transparency of the contacts is worse than "Quad". To verify this, the calculations using the excess current are repeated. The inset in Fig. 46 gives the needed I-V graph. The extracted value is $I_{exc} = -5.2\ \mu V$, which is negative, already showing the low transparency of the junction. Using the normal resistance $R_N = 58\ \Omega$ and the gap size $\Delta = 2.1$ meV one can calculate the normalized insufficient voltage $eI_{exc}R_N/\Delta = -1.5$. This value is identical for a single as well as a double JJ, because the resistance doubles, while the current is half of its original value. Equivalent to sample "Quad", one can use the inset in Fig. 35 to extract the dimensionless barrier height Z. The calculated normalized insufficient

voltage is too small to extract a value for Z as the needed range is not plotted in the original Ref. [75]. What can be said with certainty, however, is, that Z is much higher than the value obtained with "Quad".

The multiple Andreev reflections show a high transport quality of the HgTe layer, even though the excess current has a very low interface transparency. This result hints, that even though the transport quality of the capped HgTe is better, the lithographic process in this case was not able to create contacts comparable to "Quad". The most plausible explanation is, that the cap layer was not fully removed and the remaining CdHgTe acts as a thin insulating barrier at the HgTe/Nb interface. This problem could be solved, by developing a lithographic recipe which allows for deeper etching. Even though this junction only has a very low transparency the results on the Andreev reflections reveal that it is feasible to work with capped HgTe layers in the future. The increased phase coherence length will allow for stronger induced superconductivity as soon as the contact transparency is lowered to that of uncapped HgTe samples.

Due to shortcomings of the JJs on the capped sample the basic geometry of a SQUID has already been mentioned. The next chapter will further discuss these devices and especially have a look at their behavior in a magnetic field.

6

SUPERCONDUCTING QUANTUM INTERFERENCE DEVICES (SQUIDS)

A SQUID is a superconducting ring structure with at least one weak link, i.e. a Josephson junction. There a two main categories: RF-SQUIDs[1] have a single weak link and need to be inductively coupled to a RF-source. DC-SQUIDs on the other hand need two weak links, but can be used with just an applied DC-voltage [43]. Both variants are commonly applied to measure magnetization and provide a very high resolution, compared to other techniques like Hall sensors.

In this thesis only DC-SQUIDs with two weak links are investigated. A known magnetic field is applied externally to the SQUIDs in order to manipulate the phase difference between the two sides of the weak links and study the resulting modulation of current flow. By using different layouts of the Nb contacts one is able to analyze the symmetry of the superconducting order parameter [53, 87, 88] and thus evaluate the expected uniformity [15].

6.1 THEORETICAL CONCEPT

The basic geometrical layout of a SQUID fabricated on HgTe is shown in Fig. 47 a). The superconducting ring built from Nb has two integrated JJs and is contacted on either side. For simplicity the SQUID will first be described as a ring structure with two JJs as weak links. This allows to neglect all influences of magnetic field on the JJs itself due to their finite size.

The following description is taken from Refs. [43, 89]. The magnetic flux Φ_{tot} inside the superconducting ring consists of two components. The first component is the external supplied flux Φ_a, which depends on the area A of the ring and the magnetic

1 RF is short for radio frequency. Those SQUIDs are commonly used at frequencies around 25 MHz.

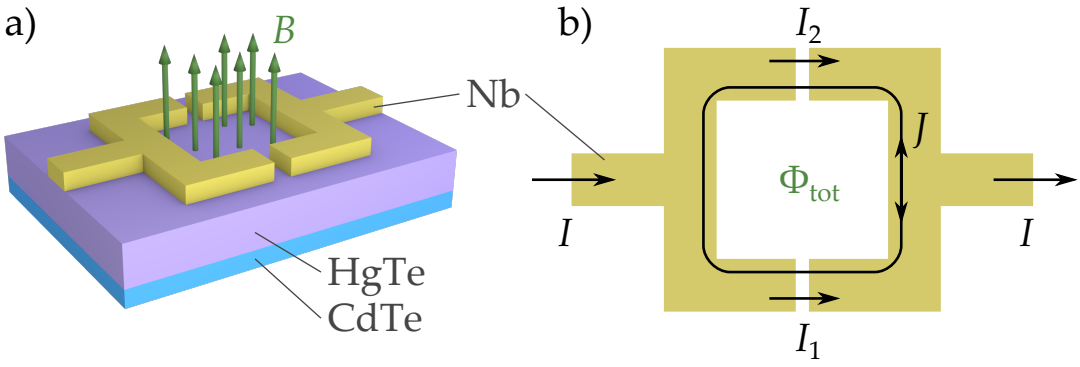

Figure 47: a) Superconducting Nb ring on top of a bulk HgTe layer. The ring has two Josephson junctions and each side is connected to external contacts. A magnetic field B is applied perpendicular to the ring structure. b) top view of the SQUID with the relevant currents in the system. The currents $I_{1,2}$ and the ring current J flowing over the JJs define the critical current behavior of the full structure, with the flux Φ_{tot} present inside the ring.

field B applied perpendicular to the device [see Fig. 47 a)]. The second part is the self induced flux Φ_{ind} generated by the superconducting ring, in order to fulfill flux quantization in the system [90]. This means as long as the ring is superconducting the total flux will always be $\Phi_{tot} = n\Phi_0$ with n being an integer and Φ_0 the flux quantum. The induced flux is generated by a shielding current J which is related to the generated flux by the self inductance L of the SQUID. J can be positive or negative, depending on the induced flux being added or subtracted. In short, this means

$$\Phi_{tot} = \Phi_a + \Phi_{ind} = BA + LJ. \tag{52}$$

Due to the flux quantization, J will generate the smallest necessary flux Φ_{ind} to round Φ_a to the next integer part of Φ_0, which in turn means that the size of the self induced flux always has to be $|\Phi_{ind}| \leq \Phi_0/2$. This can later be used to estimate the inductance of the system. The interesting questions now is how much current is passed over each JJ, as they limit the possible total critical current of the SQUID. Figure 47 b) gives an overview of all currents in the system. The current I applied externally splits equally and runs through each JJ. As a result the currents through the JJs, taking the ring current J into account, are

$$I_1 = I/2 + J \quad \text{and} \quad I_2 = I/2 - J. \tag{53}$$

In chapter 5 the phase dependent behavior of a JJ, neglecting its finite area, was described by Eq. (42), which in this case applies to both JJs separately, i.e. $I_n = I_{C,n}\sin(\gamma)$,

with $n = 1, 2$ referring to the two JJs. Integrating over the ring structure one can calculate the phase difference γ between both superconducting regions separated by the JJs to

$$\gamma = \gamma_2 - \gamma_1 = \frac{2\pi}{\Phi_0}(\Phi_a + \Phi_{ind}). \tag{54}$$

Rewriting Eqs. (53) and inserting Eq. (54) as well as the current phase relations for the JJs one achieves the current

$$I = (I_{C,1} + I_{C,2}) \sin(\delta) \cos\left(\pi \frac{\Phi_{tot}}{\Phi_0}\right) + (I_{C,1} - I_{C,2}) \cos(\delta) \sin\left(\pi \frac{\Phi_{tot}}{\Phi_0}\right) \tag{55}$$

with $\delta = \gamma_1 + \pi\Phi_{tot}/\Phi_0$. The last expression shows, that the relative phase between the two superconducting regions is defined by the applied flux, but the absolute phase of the system is still free. γ_1 will adjust itself in order to allow the highest possible critical current to flow over the SQUID device. As a result one can maximize Eq. (55) with regard to γ_1 to get the expression for the critical current of the SQUID [91]

$$I_{C,SQUID} = \sqrt{(I_{C,1} - I_{C,2})^2 + 4 I_{C,1} I_{C,2} \cos\left(\pi \frac{\Phi_{tot}}{\Phi_0}\right)}, \tag{56}$$

which only depends on the critical currents of the JJs and the applied flux in the ring. This more complex treatment of using different critical currents for both JJs was done, as it will be needed later. In a simpler case of a symmetric SQUID, meaning $I_C = I_{C,1} = I_{C,2}$, Eq. (56) reduces to the commonly known formula

$$I_{C,SQUID,sym} = 2 I_C \left| \cos\left(\pi \frac{\Phi_{tot}}{\Phi_0}\right) \right|. \tag{57}$$

The results so far are plotted in Fig. 48. In all cases the oscillations have maxima at integer multiples of Φ_0 and minima at half integer values in between. The simplest result is the case of a symmetric SQUIDs, where the oscillations start at $I_{C,SQUID} = 0$ A and have the amplitude $2I_C$. Introducing an asymmetry in the critical currents of the two weak links, in Fig. 48 shown for $I_{C,1} = 1.5 I_{C,2}$, leads to the minima shifting to a value of $|I_{C,1} - I_{C,2}|$ and the maxima to $|I_{C,1} + I_{C,2}|$.

So far the area of the JJs has been neglected. In order to include the influence of their finite size the critical current $I_{C,n}$ needs to be replaced by the flux dependent critical current $I_{C,n}(\Phi_{JJ,n})$, with the flux $\Phi_{JJ,n}$ in JJ number n. The critical current in each JJ is then described by Eq. (49), this Fraunhofer shape was already discussed

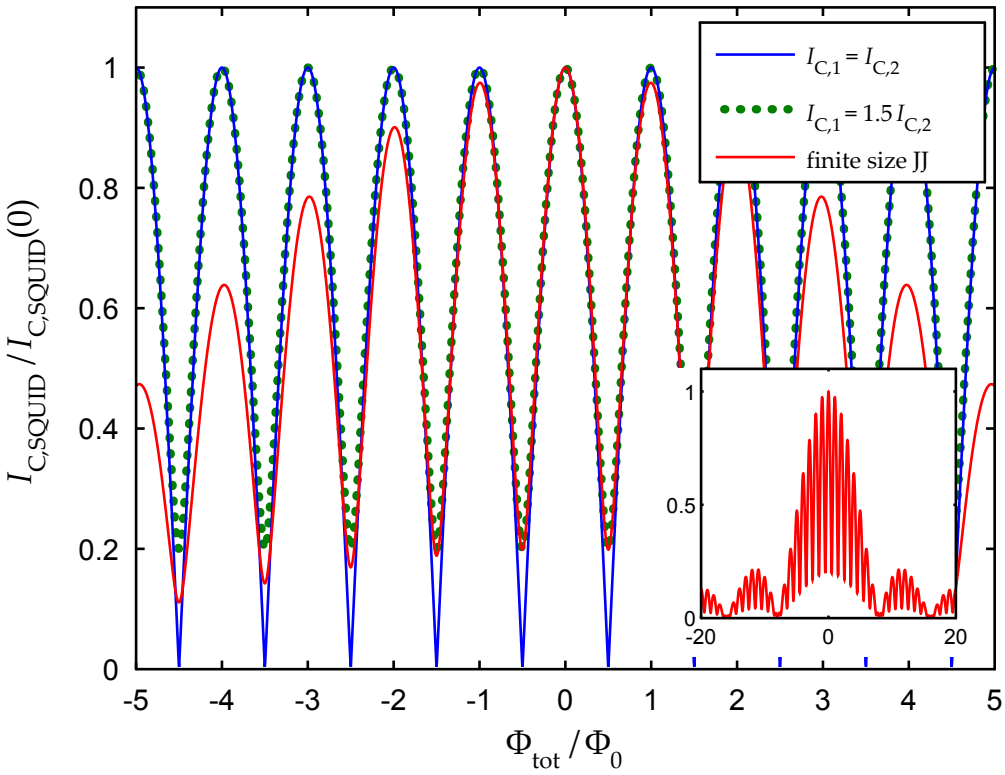

Figure 48: Graphs showing the theoretical expectations for symmetric ($I_{C,1} = I_{C,2}$), asymmetric ($I_{C,1} \neq I_{C,2}$) SQUIDs, as well as the influence of finite size JJs on the oscillation pattern.

in detail in the previous chapter. The resulting SQUID oscillations additionally show the Fraunhofer oscillations, but due to the smaller area and thus smaller amount of flux in the JJs the oscillation period is much smaller than the SQUID period itself. As a result in the main plot in Fig. 48 only the central Fraunhofer peak is visible. For better understanding a wider flux range is plotted in the inset of Fig. 48. After this introduction to general SQUID behavior the actual sample layout will be discussed.

6.2 SQUID SAMPLE DESIGN

A microscope picture of the first SQUID sample "Shot" is shown in Fig. 49 a). It consists of three symmetrical SQUIDs, as seen in the colored SEM picture in Fig. 49 b). These are symmetric in the sence, that the two JJs have the same geometrical dimensions and thus should have the same behavior with regards to the critical current they can carry. The next three devices on sample "Shot" are asymmetrical SQUIDs [Fig. 49 c)], who have one JJ comparable to the symmetrical case and one JJ is at the

corner and has a 90° angle between the two adjacent contacts. The last device on this sample is a single JJ, which was intended to be a reference, but unfortunately was damaged and therefore unusable.

Those two types of SQUIDs allow to investigate the symmetry of the superconducting band gap. In the case of a S/TI interface a non angle-dependent superconducting order parameter is expected, as seen in the Hamiltonian of the system [Eq. (27)], and thus both types of SQUIDs would be in phase. If however the superconducting order parameter is mainly p- or d-like a phase shift is expected [53, 87, 92].

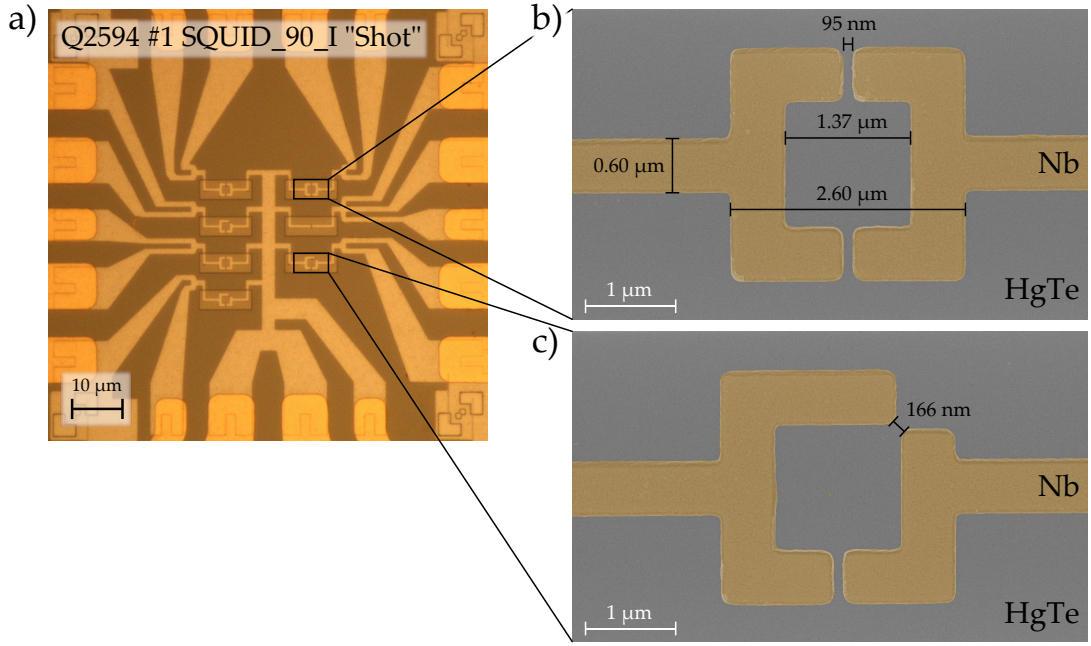

Figure 49: a) Microscope picture of sample "Shot" showing the following devices: three symmetric SQUIDs, three asymmetric SQUIDs with a 90° angle in one JJ and one single JJ. b) colored SEM picture of a symmetric SQUID including the measured distances and c) an asymmetric SQUID.

In order to be able to have the highest amount of devices on a single sample one contact of each device is connected to the central Nb area. One however has to be aware of that unwanted interactions could arise between the devices, due to the shared superconducting contact. All measurements were analyzed for such interactions but none were observable. A second important aspect is, that each device has a separate rectangular HgTe mesa over the complete device area. This means the current is not forced into each arm of the Nb ring, but guided by the path of smallest resistance. This is of course true for the superconductor and additionally it is expected, that the current will only flow through the weak links, as they have the smallest distance in the HgTe and thus should have the smallest resistance. However, this might no longer

be the case for high Nb/HgTe interface resistance or ballistic transport in the HgTe layer. As a result it still could be possible to conduct current in the other regions of the HgTe as well. Following this introduction it is time to discuss the measurement results.

6.3 SYMMETRIC AND ASYMMETRIC SQUID

The current bias dependance of a symmetric SQUID, without an applied magnetic field, is not very different from a JJ as seen in Sec. 5.8, where it was possible to interpret it as two JJs in parallel. Thus one can directly start the discussion with the magnetic dependance shown in Fig. 50. The current oscillates periodically between a maximum value and zero. In comparison with the theoretical behavior presented above, this directly suggests, that the maximum critical currents of both JJs are identical (see Fig. 48). The measurement intentionally only records one side of the magnetic axis as it is symmetric around $B = 0$ T. The symmetry of the magnetic behavior was tested, by measuring a single trace in the resistive regime. To get an idea for the timescale: in this case the measurement took three days.

The measurement data from Fig. 50 was fitted with the theoretical expectations from Eq. (56) (green line). This allows the extraction of the oscillation period in magnetic field B_P, the critical current of each JJ $I_{C,n}$ and the relation between the flux penetrating the SQUID and the flux penetrating each JJ. This relation equivalently describes the ratios of the oscillation periods and the effective areas the flux is penetrating:

$$t_n = \Phi_{JJ,n}/\Phi_{SQUID} = B_{JJ,n}/B_P = A_{JJ,n}/A_{SQUID} \tag{58}$$

.

The resulting values are listed in Table 2.

Before discussing these values the validity of the model has to be established, namely the assumption that the induced flux Φ_{ind} is negligible and thus $\Phi_{tot} = \Phi_a$. This is only true if the inductance of the device is small. Looking closer at the values around zero current, shown in Fig. 51, one can see that a non superconducting region develops at the minima, which grows with increasing field. This region arises, because the system tries to fulfill flux quantization by generating the ring current J. If this current becomes higher than the maximum possible critical current of both JJs, they enter the resistive regime. The first minimum already seems to show a resistive gap, but

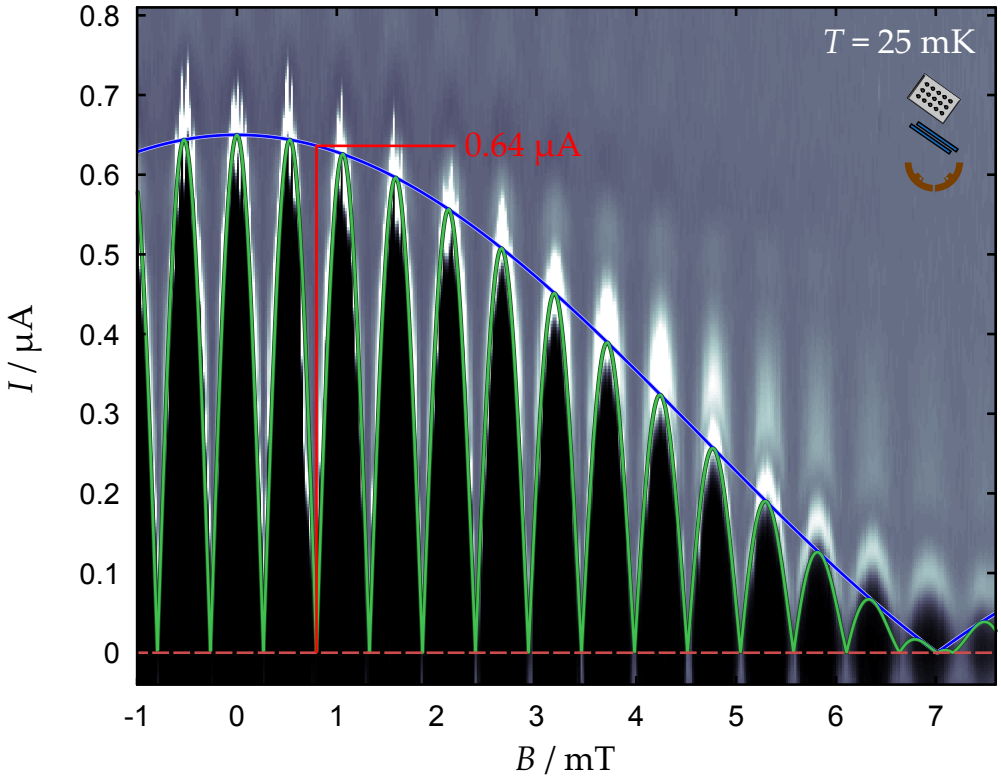

Figure 50: Magnetic and current dependence of a symmetric SQUID [for geometry see Fig. 49 b)]. The color scale shows the absolute of the numerically calculated differential resistance, which was calculated in the same way as for the Fraunhofer patterns in Figs. 41 and 42 in the previous chapter. The green line is a fit of the maximum critical current, including the finite size of the JJs. The blue envelope shows the maximum current, while disregarding the effect of the induced ring current J. The marker at 0.78 mT gives the current value of the envelope used in the estimation of L

one can not be certain due to the resolution of the measurement. However it is clear that the second minima at 0.78 mT is wider and has a finite width. To estimate the maximum inductance one can use the above mentioned relation for the induced flux $|\Phi_{\text{ind}}| \leq \Phi_0/2$, which can be converted to $L \leq \Phi_0/(2\,|J|)$. Due to the appearance of the effect one can already assume that L is quite small, as a high ring current is needed to generate the compensating flux Φ_{ind}. With the estimation that $J \approx I_{\text{C,n}}(0.78\,\text{mT})$ the value can be either calculated from the theoretical formula for the JJs or in this symmetric case extracted from the envelope of the SQUID oscillations (blue in Fig. 50), which describes the maximum current of both JJs without the influence of the self induced ring current: $I_{\text{C,n}}(0.78\,\text{mT}) = I_{\text{envelope}}(0.78\,\text{mT})/2 = 0.32\ \mu\text{A}$. This results in an upper limit for the inductance $L_{\text{max}} = 3.1$ nH.

The values extracted from the fit (see Table 2) can now be used to further investigate the properties of the device. Analogous to the calculations performed with the area

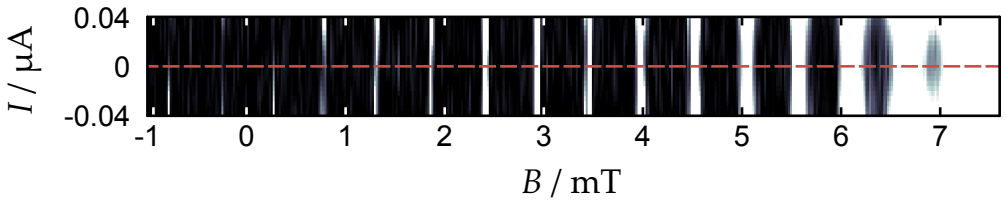

Figure 51: Cutout of Fig. 50 around zero current. The non superconducting regions at the minima are increasing, when going to higher magnetic fields. The color axis has been multiplied by 16 in comparison to Fig. 50 in order to increase the visibility of the minima.

of the JJ, one can employ the magnetic periodicity to calculate the effective area of the SQUID $A_{\mathrm{SQUID}} = \Phi_0 / B_{\mathrm{P}} = 3.9\ \mu\mathrm{m}^2$. As the SQUID is designed as a square one side of the effective area is $l_{\mathrm{SQUID}} = \sqrt{A_{\mathrm{SQUID}}} = 2.0\ \mu\mathrm{m}$, which fits very well to the sizes measured in Fig. 49 b), with the assumption that the supercurrent is mostly flowing in the center of the current path. This is justified, when taking the penetration depth into account. Both critical currents of the JJs are of equal size. This is of course expected as the symmetry of the geometrical layout is mirrored in the measurement of the device. The factors t_1 and t_2, which are also equal in the symmetric SQUID, allow to calculate the periodicity of the JJs as $B_{\mathrm{JJ},n} = B_{\mathrm{P}} t_{\mathrm{n}} = 6.9\ \mathrm{mT}$. This corresponds to an area of $A_{\mathrm{JJ},n} = 0.30\,\mu\mathrm{m}^2$. Using the same approach as in Sec. 5.6 one receives a London penetration depth of $\lambda_{\mathrm{JJ}} = 0.20\ \mu\mathrm{m}$. This is quite small compared to the single JJ on sample "Quad" ($\lambda = 0.41\ \mu\mathrm{m}$) discussed earlier. It is however explainable, because, as seen from the effective area of the SQUID, the supercurrent in the Nb is forced to the center and thus the actual width of the JJ is smaller than the geometrical extent. The reduction of the width consequently increases the length and hence λ_{JJ} in the calculation, as the effective area stays the same. This effect is not as dominant in the JJ on "Quad" as it is four times wider.

The fit deviates from the measurement for values greater than 6 mT. In this area the effect of the SC does still strongly reduce the resistance of the SQUID, but the system no longer becomes fully superconducting. As a result Eq. (56), describing the system in the superconducting state, is no longer applicable.

	symmetric SQUID	asymmetric SQUID
$B_{\mathrm{P}}/\mathrm{mT}$	0.53	0.56
$I_{\mathrm{C},1}/\mu\mathrm{A}$	0.33	0.081
$I_{\mathrm{C},2}/\mu\mathrm{A}$	0.33	0.30
t_1, t_2	13	21, 11

Table 2: Fit parameters of symmetric and asymmetric SQUID devices on sample "Shot".

The asymmetric SQUID will now be presented in comparison to the symmetric one. The measurement in Fig. 52 shows the behavior for the case of $I_{C,1} \neq I_{C,2}$ as presented in Fig. 48. This already indicates the different critical currents of both JJs. The resolution in this measurement is reduced compared to the prior one, yet it is still high enough to be able to compare it. This measurement only took one day instead of the three days of Fig. 50.

The values obtained from the fit using Eq. (56) are listed in Table 2 next to the results of the symmetric SQUID. $I_{C,2}$ has almost the same value for both SQUIDs. Consequently it can be attributed to the two identical JJs in the compared devices [lower JJ in Fig. 49 a) and b)]. The other critical current $I_{C,1}$ is much smaller, which can be explained by the increased distance of the contacts in the bent JJ. This interpretation is also reinforced, when looking at t_n. In the case of t_2 the values are comparable for both SQUIDs, while t_1 clearly shows that the effective area for the bent JJ in the asymmetric SQUID is much bigger, likewise due to the larger JJ length.

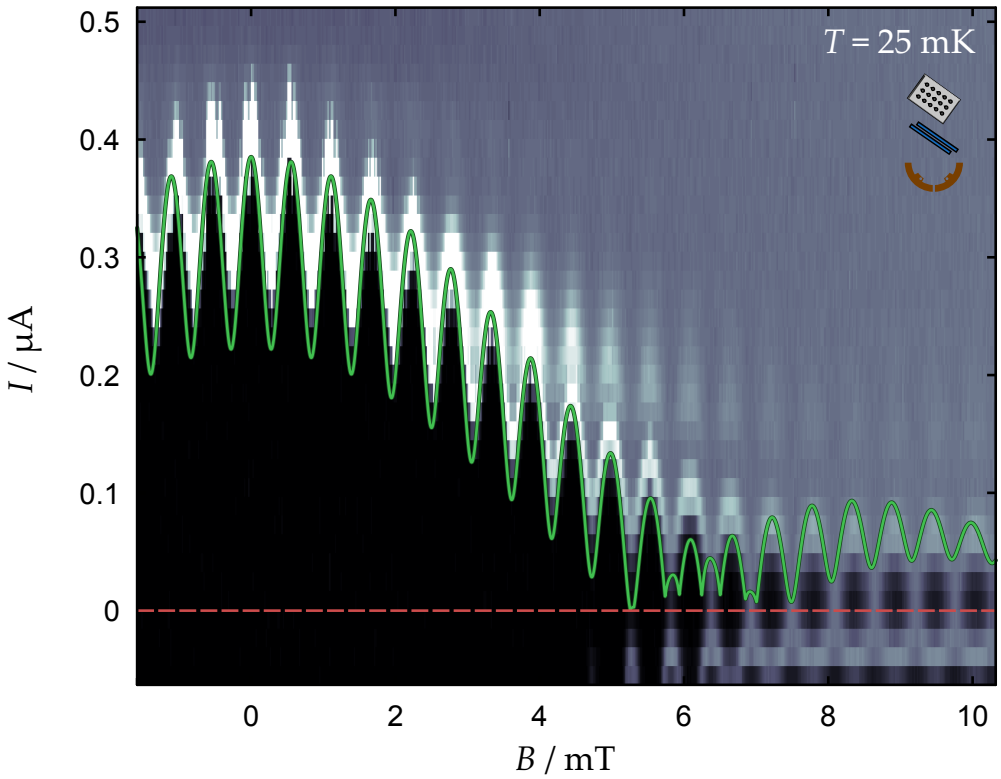

Figure 52: Magnetic and current dependence of an asymmetric SQUID [see Fig. 49 c)]. The green line is a fit of the maximum critical current, including the finite size of the JJs, after Eq. (56).

Just as in the symmetric SQUID the device is no longer fully superconducting above 6 mT and the model starts to deviate from the measurement. Unfortunately, as in this

region a beating, due to the different oscillation periodicities of the two JJs appears in the fit, it can no longer be compared to the measurement.

So far the oscillation pattern of both SQUIDs can be explained with Eq. (56) and thus do not reveal unusual behavior, which would be seen as an influence of the topological surface states in the system. However, due to the hysteresis in the superconducting magnet, the position of zero magnetic field could actually be slightly different in both measurements, hiding a relative shift. If both measurements (Figs. 50 and 52) are in phase, meaning that at $B = 0$ T both measurements show a maximum, then the results are in agreement with the S/TI Hamiltonian [Eq. (27) discussed in Sec. 3.3]. This is the expected behavior and would prove that the HgTe layer does not have a dominant p- or d-wave symmetric band gap. However, if a phase shift could be detected, one would be looking at an unusual pairing, not consistent with the proposed non angle-dependent Hamiltonian.

To be able to make the distinction between those two cases, the next chapter will discuss the possibility to reliably extract the shift between two measurements. This allows to eliminate the need to exactly know the position of zero magnetic field, if the symmetric SQUID is used as reference.

6.4 PHASE RELATION BETWEEN DIFFERENT DEVICES

To be able to properly compare the position of different measurements in magnetic field, one firstly needs to establish the reproducibility as well as the stability over time. To examine this parameters a symmetric SQUID, geometrically identical to the one shown in Fig. 49 b), from sample Q2594 #4 SQUID_IV "Flat" was measured repeatedly over time. The current bias was chosen high enough to keep the sample in the resistive regime and low enough to still be able to detect some signal of the SQUID.

The result is shown in Fig. 53. Every two consecutive measurements are grouped and plotted as one color. These are recorded in opposite directions to be able to tell if any hysteretic effects in the superconducting magnet are visible. This seems not to be the case in this small magnetic range. However, a shift of the pattern over time is clearly visible. The whole measurement cycle took 16 hours to complete and the total shift in magnetic field was $\Delta B = 45$ µT, giving a magnetic shift rate of 2.8 µT/h. This behavior was not consistently observed in all measurements and was even completely

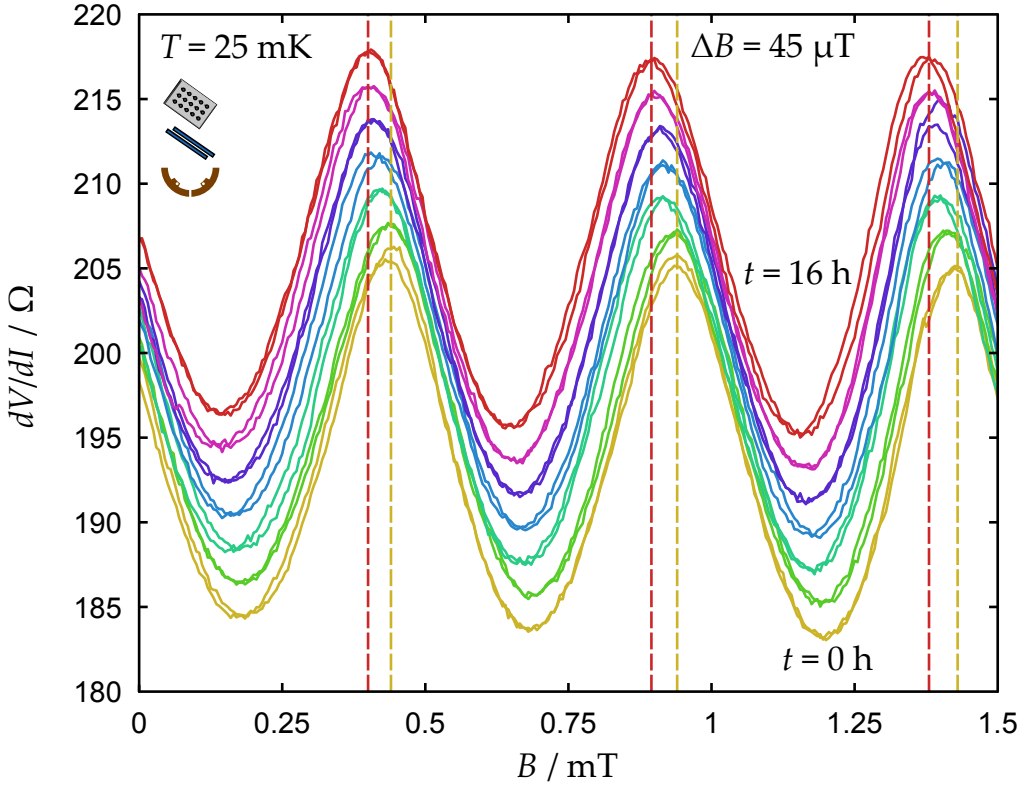

Figure 53: Magnetic dependence of a SQUID oscillation in the resistive regime. One color always consists of two consecutive measurements, one in positive and one in negative direction. The measurement is continuously repeated over 16 hours.

absent in some. Nevertheless this effect limits the maximum resolution if one wants to compare the relative position of two separate measurements in magnetic field.

As mentioned above, the usual measurements to extract the critical current are conducted in the timescale of days and thus can not be compared at the given drift rate. In order to deal with that situation the measurement system presented in Sec. 4.3.3 on page 46 was developed, which is able to perform a critical current measurement over the same magnetic range as in Figs. 50 and 52 in about one hour.

To test the new system several devices are compared. Sample Q2594 #5 SQUID_V "Dots", consisting of two JJs and two symmetric SQUIDs and, to have a different material type, two graphene based JJs were included on the second sample probe. In the latter the weak link material is a sheet of graphen contacted by Nb electrodes. The area of this JJs was chosen to be comparable to the HgTe based devices, making the oscillation period and thus the comparison easier. Both samples were built into the setup simultaneously and as a result all devices could be measured one after another in a short time period.

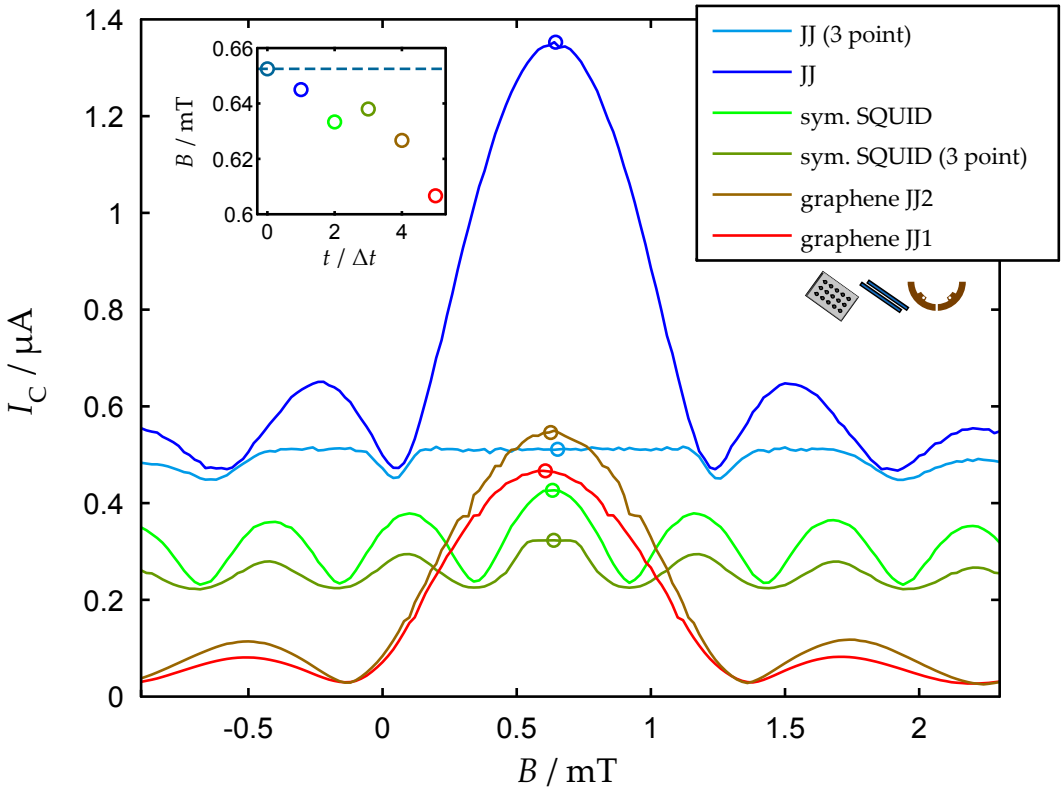

Figure 54: Comparison of magnetic position of SQUIDs and JJs on HgTe as well as JJs based on graphene. The center position is marked as circle. The inset in the top left corner shows the positions of the center dependent on the time they were recorded normalized by the average time between two measurements is $\Delta t \approx 41$ min.

All measurements are plotted in Fig. 54 and were recorded in the order listed in the legend from top to bottom. The results are plotted with an offset on the I_C-axis for better visibility. Two devices could only be measured in 3-point geometry, which means, that no adequate values for I_C could be extracted. This is visible as flattened peaks, as the threshold value of the measurement is reached prematurely, due to the additional contact resistance. However, it is still possible to use the positions of the minima to extract the relative shift to the other measurements. Every device is present twice in order to examine if the behavior is consistent between identical structures, which was not always the case in earlier measurements, due to superconducting residues close to and on the back of the samples. Additionally the shared Nb contact was abandoned reducing the number of devices per sample from seven to four. With these restrictions there was no room left for an asymmetric SQUID at this point.

To compare the position of the measurements the center point of all graphs was calculated. This was done by taking two corresponding extrema (minima or maxima) on the left and right side of the center and averaging them: $B_{\text{center},n} = (B_{\text{ext, left},n} +$

$B_{\text{ext, right}, n})/2$. The center for one measurement is then $B_{\text{center}} = \frac{1}{n}\sum_n B_{\text{center}, n}$, which is marked as circle in Fig. 54. As one can see the centers are shifted with respect to each other. The shift is plotted in the top left corner of Fig. 54 from the beginning of the first measurement at $t = 0$ min to the beginning of the last measurement at $t = 200$ min. This gives a mean time difference of $\Delta t \approx 41$ min between a point measured in one graph compared to a point measured in the next graph. The center position is shifting in one direction over time, just as the previous measurement showed. The difference in magnetic field from the first to the last center is $\Delta B_{\text{center}} = 18$ µT, which results in a shift rate of 5.5 µT/h. This is slightly higher, but still comparable to the previous value. Because the shift can be attributed to the environmental conditions of the magnetic field, the centers are aligned within the error margins of the system.

Additionally the graphene JJs were chosen for a comparison with a different material group. Graphene is a 2-dimensional system with a linear band structure, but in comparison to HgTe has multiple Dirac cones. These JJs have already been studied and the expected results are available in literature [93]. This allows to conclude that the main maximum of the JJ in graphene and due to the information gathered in Fig. 54 also the main maximum in HgTe based junctions coincide and both are appearing at zero magnetic field. As a result HgTe based JJs can be used as a reference device to cancel out the problem of determining the absolute field value, due to the hysteresis of a superconducting magnet.

It is clearly visible in Fig. 54 that both symmetric SQUIDs and all JJs show a maximum at the same field value, which has to be at zero magnetic field after taking account of the hysteresis. The interesting question asked in the previous section however was the relation between a symmetric and an asymmetric SQUID. For this sample only symmetric SQUIDs were used to be able to test the reproducibility and all samples with both types of SQUIDs were measured before all optimizations were finished and thus their position in magnetic field can not directly be compared, as done here. As a result it is not possible to give a definite answer whether the symmetric and asymmetric SQUIDs produced here are in phase. Still prior measurements have hinted, that this is the case and now all preparations are made to be able to make this comparison in the next step.

6.5 ZERO MAGNETIC FIELD ANOMALY

A special feature, that was observed in several SQUIDs, is an increased peak at $B = 0$ T, which will be referred to as zero magnetic field anomaly (ZMFA). Because this central peak is very pronounced it can be used to correct the hysteresis. But this feature is not always present and thus can not consistently be used as a zero field indicator. In a SQUID without the ZMFA, the amplitude difference between neighboring peaks is too small to reliably pick the center peak. The phenomenon appeared, e.g., in sample "Dots" shown in Fig. 55. To give a graphical idea of the deviation, the expected amplitude of the central peak relative to its neighbors is marked as a red dashed line in the graph for the lowest temperature of 30 mK. This deviation from the ideal theoretical expected pattern as shown in Fig. 48 in Sec. 6.1 can not be explained by a variation in the effective areas of the SQUID's JJs and thus a variation of the envelope of the SQUID oscillations. The effect has to originate from an aspect not considered in the presented model.

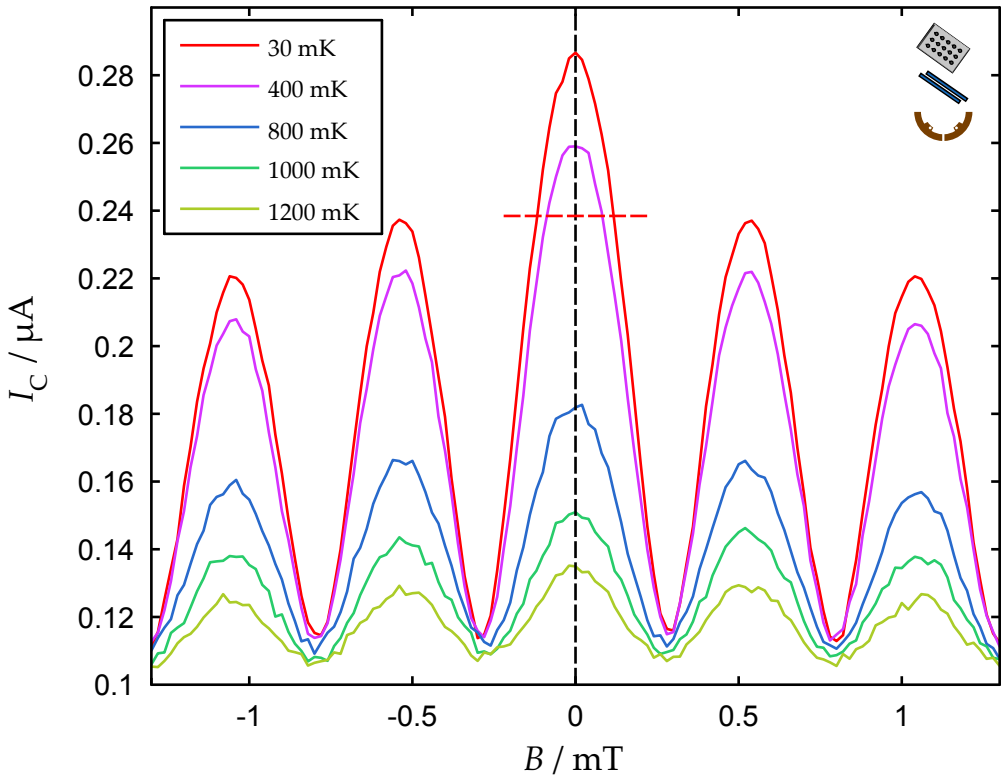

Figure 55: ZMFA for several temperatures of a symmetric SQUID on sample "Dots". The expected height at zero magnetic field for $T = 30$ mK is shown as red dashed line.

To estimate an energy range of this effect the curves have been recorded at several temperatures. Due to the reduction of the critical current with increasing temperature the absolute amplitudes are becoming smaller. To be still able to compare different temperatures the relative heights of the off-center peaks $I_{C,i=2,3}$ normalized to the central peak $I_{C,1}$ have to be considered (see Table 3). For the model parameters the effective JJ areas extracted from the symmetric SQUID of sample "Shot" were used (see Fig. 50) as they have the same geometry as "Dots". The relative heights are approaching the model values as the temperature rises. In this case the ZMFA is consequently faster suppressed than the maximum critical current, showing that the energy scale of the ZMFA is slightly smaller than those of the critical current of the JJs.

Temperature T	$I_{C,1}/I_{C,1}$	$I_{C,2}/I_{C,1}$	$I_{C,3}/I_{C,1}$
30 mK	1	0.83	0.76
400 mK	1	0.85	0.80
800 mK	1	0.91	0.87
1000 mK	1	0.96	0.91
1200 mK	1	0.95	0.94
model	1	0.99	0.96

Table 3: Relative height of off-center peaks $I_{C,i=2,3}$ normalized to the height of the central peak $I_{C,1}$ of sample "Dots". With increasing temperature the values are approaching the models parameters.

Both SQUIDs on sample "Shot" and on sample "Dots" are geometrically identical, but only the latter shows the ZMFA. Thus the effect can not be related to geometrical differences. In addition both samples are build from the same HgTe layer "Q2594" (see Appx. A.1 for more information). What however can be different is the interface barrier parameter Z. As there are no long range dV/dI curves recorded on these SQUIDs one can not extract I_{exc} and consequently Z. Still it is possible to compare the total critical currents in the symmetric SQUIDs of both devices, which is 0.6 µA for "Shot" and 0.29 µA for "Dots". As the only difference between the two samples lies in the lithographic process it has to be assumed, that the lower critical current in Dots can be attributed to a higher Z parameter.

It was stated earlier, that the current path in the system is defined by the lowest resistance. If the resistance of the interface between the HgTe and the Nb is the dominant contribution, which is the case for a high enough barrier Z, the length dependent resistance in the HgTe layer itself becomes less relevant. As a result current paths apart from the obvious ones in the two JJs become more plausible. These longer paths, most

probably running through the center of the SQUID, would be more susceptible for an increase with temperature, because the binding energies are smaller due to the greater distance the induced superconductivity has to bridge [see Eq. (26)]. This is consistent with the thermal behavior seen in sample "Dots" (see Table 3). Additional current paths could distort the idealized SQUID pattern described by Eq. (56) and hence lead to the observed measurement. This distortion of an idealized pattern due to a different current distribution is similar to the effects seen in the Fraunhofer pattern in the JJ earlier. A detailed analysis as well as an example for the influence of a change in the local current distribution can be found in Ref. [94] and its supplementary material.

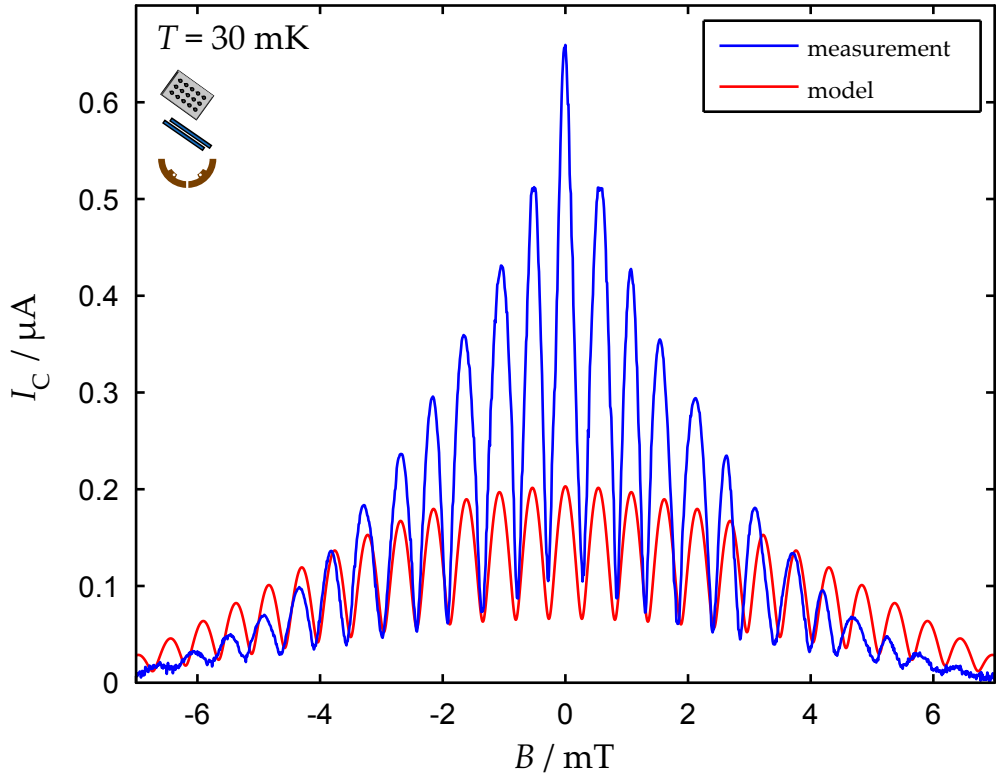

Figure 56: The SQUID pattern is strongly deviating from the model on the capped sample "Shade", which showed an exceptionally high BTK barrier strength Z.

If the above argumentation is valid, then the effect should be more pronounced for samples with higher Z values and lower resistivity of the HgTe layer. This example can be found in the capped HgTe sample "Shade", where the barrier strength was exceptionally high compared to "Shot" and "Dots" and the resistivity of the HgTe itself is reduced, because of the increased mobility enabled by the capping layer. A curve of the critical current for a symmetric SQUID, which is also geometrically identical to the above mentioned samples, is shown in Fig. 56. In this case the deviations to the

model (red graph) are much stronger and are not only localized at the central peak. It is no longer possible to find suitable parameters for the model to match the shape of the measurement graph, as it was done to analyze the data of the symmetric and asymmetric SQUIDs in Figs. 50 and 52. It seems as if the deviation due to additional current paths is a justified concern and has to be investigated further.

The next step would be the development of a lithographic process to be able to fabricate a sample without HgTe in the center of the SQUID hole, in order to properly define the possible current paths. Furthermore a optimizations of the capped HgTe sample production would help to produce interfaces with a small barrier strength Z. In comparison to the presented measurements both options would give an idea of the influence of these additional current paths and how they could be avoided. In the following chapter a summary of the results presented in this thesis is given.

7

SUMMARY

The combination of a topological insulator (TI) and a superconductor (S), which together form a TI/S interface, is expected to influence the possible surface states in the TI. It is of special interest, if the theoretical prediction of zero energy Majorana states in this system is verifiable. This thesis presents the experimental realization of such an interface between the TI strained bulk HgTe and the S Nb and studies if the afore mentioned expectations are met.

As these types of interfaces were produced for the first time the initial step was to develop a new lithographic process. Optimization of the S deposition technique as well as the application of cleaning processes allowed for reproducible fabrication of structures. In parallel the measurement setup was upgraded to be able to execute the sensitive measurements at low energy. Furthermore several filters have been implemented into the system to reduce high frequency noise and the magnetic field control unit was additionally replaced to achieve the needed resolution in the µT range.

Two kinds of basic geometries have been studied: Josephson junctions (JJs) and superconducting quantum interference devices (SQUIDs). A JJ consists of two Nb contacts with a small separation on a HgTe layer. These S/TI/S junctions are one of the most basic structures possible and are studied via transport measurements. The transport through this geometry is strongly influenced by the behavior at the two S/TI interfaces. In voltage dependent differential resistance measurements it was possible to detect multiple Andreev reflections in the JJ, indicating that electrons and holes are able to traverse the HgTe gap between both interfaces multiple times while keeping phase coherence. Additionally using BTK theory it was possible to extract the interface transparency of several junctions. This allowed iterative optimization for the highest transparency via lithographic improvements at these interfaces. The increased transparency and thus the increased coupling of the Nb's superconductivity to the HgTe

results in a deeper penetration of the induced superconductivity into the HgTe. Due to this strong coupling it was possible to enter the regime, where a supercurrent is carried through the complete HgTe layer. For the first time the passing of an induced supercurrent through strained bulk HgTe was achieved and thus opened the area for detailed studies. The magnetic dependence of the supercurrent in the JJ was recorded, which is also known as a Fraunhofer pattern. The periodicity of this pattern in magnetic field compared to the JJ geometry allowed to conclude how the junction depends on the phase difference between both superconducting contacts. Theoretical calculations predicted a phase periodicity of 4π instead of 2π, if a TI is used as weak link material between the contacts, due to the presence of Majorana modes. It could clearly be shown that despite the usage of a TI the phase still was 2π periodic. By varying further influencing factors, like number of modes and phase coherence length in the junction, it might still be possible to reach the 4π regime with bound Majorana states in the future. A good candidate for further experiments was found in capped HgTe samples, but here the fabrication process still has to be developed to the same quality as for the uncapped HgTe samples.

The second type of geometry studied in this thesis was a DC-SQUID, which consists of two parallel JJs and can also be described as an interference device between two JJs. The DC-SQUID devices were produced in two configurations: The symmetric SQUID, where both JJs were identical, and the asymmetric SQUID, where one JJ was not linear, but instead has a 90° bent. These configurations allow to test, if the predicted uniformity of the superconducting band gap for induced superconductivity in a TI is valid. While the phase of the symmetric SQUID is not influenced by the shape of the band gap, the asymmetric SQUID would be in phase with the symmetric SQUID in case of an uniform band gap and out of phase if p- or d-wave superconductivity is dominating the transport, due to the 90° junction. As both devices are measured one after another, the problem of drift in the coil used to create the magnetic field has to be overcome in order to decide if the oscillations of both types of SQUIDs are in phase. With an oscillation period of 0.5 mT and a drift rate in the range of 5.5 µT/h the measurements on both configurations have to be conducted in a few hours. Only then the total shift is small enough to compare them with each other. For this to be possible a novel measurement system based on a real time micro controller was programmed, which allows a much faster extraction of the critical current of a device. The measurement times were reduced from days to hours, circumventing the drift prob-

lems and enabling the wanted comparison. After the final system optimizations it has been shown that the comparison should now be possible. Initial measurements with the old system hinted that both types of SQUIDs are in phase and thus the expected uniform band gap is more likely. With all needed optimizations in place it is now up to the successors of this project to conclusively prove this last point.

This thesis has proven that it is possible to induce superconductivity in strained bulk HgTe. It has thus realized the most basic sample geometry proposed by Fu and Kane in 2008 for the appearance of Majorana bound states. Based on this work it is now possible to further explore induced superconductivity in strained bulk HgTe to finally reach a regime, where the Majorana states are both stable and detectable.

8

ZUSAMMENFASSUNG

Aus theoretischen Betrachtungen geht hervor, dass die Kombination eines topologischen Isolators (TI) und eines Supraleiters (S) zu einer TI/S Grenzfläche die möglichen Oberflächenzustände im TI beeinflussen kann. Von besonderem Interesse ist dabei die Vorhersage der Ausbildung von Majorana Zuständen bei Null-Energie. Diese Arbeit beschäftigt sich mit der experimentellen Realisierung einer solchen Grenzfläche zwischen dem TI verspanntes HgTe und dem S Nb und analysiert, ob die oben genannten Effekte tatsächlich in diesem System auftreten.

Da diese Grenzflächen zum ersten Mal produziert wurden, musste zunächst ein neuer lithographischer Prozess dafür entwickelt werden. Nach der Optimierung der Depositionstechnik des S sowie der Anwendung von Reinigungsschritten, war eine reproduzierbare Fertigung von Probenstrukturen möglich. Parallel dazu wurde das Messsystem ausgebaut, damit die sensitiven Messungen bei geringer Energie durchgeführt werden konnten. So wurden mehrere Frequenzfilter eingebaut, um Hochfrequenzrauschen zu reduzieren und die Magnetfeldsteuerung ersetzt, damit die benötigte Auflösung im µT Bereich ereicht werden konnte.

Es wurden zwei grundlegende Geometrien untersucht: Josephson Kontakte (engl. Josephson junctions, JJ) und supraleitende Quanteninterferenzeinheiten (engl. superconducting quantum interference devices, SQUIDs). Eine JJ besteht aus zwei Nb Kontakten mit einem kleinen Abstand zueinander, die auf einer HgTe Schicht aufgebracht werden. Diese S/TI/S Kontakte bilden eine der grundlegendsten Strukturen, die möglich sind und wurden mit Hilfe von Transportmessungen untersucht. Der Ladungstransport in dieser Geometrie wird stark durch die beiden S/TI Grenzflächen beeinflusst. In spannungsabhängigen Messungen des differenziellen Widerstandes konnten mehrfache Andreev Reflexionen in den JJ nachgewiesen werden, was zeigt, dass Elektronen und Löcher die HgTe Lücke zwischen beiden Nb Kontakten wiederholt

phasenkoherent überwinden können. Zusätzlich konnte mit Hilfe der BTK Theorie die Transparenz der Grenzflächen bestimmt werden. Dies erlaubte eine iterative Optimierung zum Erreichen der höchst möglichen Transparenz durch lithographische Verbesserungen an den Grenzflächen. Eine verbesserte Transparenz erlaubt eine stärkere Kopplung der Supraleitung des Nb an das HgTe und somit ein tieferes Eindringen der induzierten Supraleitung in die HgTe Schicht. Aufgrund der verbesserten Ankopplung war es möglich, das Regime zu erreichen, in dem ein Suprastrom durch die HgTe Schicht zwischen den Nb Kontakten getragen werden kann. Erstmals konnte ein induzierter Suprastrom durch verspanntes HgTe geleitet werden und ermöglichte es, in diesem Forschungsbereich mit detaillierten Analysen zu beginnen. Es wurde die magnetische Abhängigkeit des Suprastroms in der JJ aufgenommen, auch bekannt als Fraunhofer Muster. Die Periodizität dieses Musters im Magnetfeld im Vergleich zur geometrischen Ausdehnung der JJ erlaubt Rückschlüsse darüber, wie der Suprastrom der JJ von der Phasendifferenz zwischen beiden supraleitenden Kontakten abhängt. Theoretische Berechnungen haben vorhergesagt, dass die Periodizität dieser Phasenbeziehung von ursprünglich 2π auf 4π wechselt, falls ein TI als Material zwischen den beiden Nb Kontakten verwendet wird, da Majorana Moden auftreten. Es konnte jedoch klar gezeigt werden, dass trotz Verwendung eines TI die Phasendifferenz immer noch 2π periodisch war. Durch die Variation weiterer Einflussfaktoren, wie die Anzahl der möglichen Moden oder die Phasenkohärenzlänge in der JJ könnte es in Zukunft trotz allem immer noch möglich sein, einen Bereich zu erreichen, in dem eine 4π Periodizität mit Majorana Zuständen vorliegt. Ein erfolgversprechender Kandidat für diese Experimente konnte in verspanntem HgTe mit CdHgTe Deckschicht gefunden werden, jedoch muss der Fabrikationsprozess für diese Material erst noch entwickelt werden, um in der Lage zu sein, Strukturen zu produzieren, die qualitativ vergleichbar mit denen ohne Deckschicht sind.

Der zweite Geometrie-Typ, der untersucht wurde, ist ein DC-SQUID, das aus zwei parallelen JJs besteht und analog auch als Interferometer zweier JJs gesehen werden kann. Es wurden zwei Arten von DC-SQUIDs produziert: Das symmetrische SQUID, bestehend aus zwei identischen JJs und das asymmetrische SQUID, bei dem eine JJ nicht linear aufgebaut ist, sondern beide Nb Kontakte statt dessen einen Winkel von $90°$ zueinander aufweisen. Diese beiden Arten erlauben es die fehlende Winkelabhängigkeit der supraleitenden Bandlücke zu überprüfen, die für induzierte Supraleitung in einem TI prognostiziert wurde. Die Phase des symmetrischen SQUIDs wird nicht

durch die Form der supraleitenden Bandlücke beeinflusst. Daher kann es als Referenz verwendet werden, um eine eventuelle Phasenverschiebung des asymmetrischen SQUIDs zu erkennen. Ist keine Phasenverschiebung vorhanden, ist dies eine Bestätigung der Uniformität der Bandlücke. Falls jedoch eine Phasenverschiebung aufgrund des 90° Kontaktes auftritt, würde der Transport hauptsächlich durch p- oder d-artige Supraleitung getragen werden. Da beide SQUIDs nacheinander vermessen werden, muss sichergestellt werden, dass Drifteffekte in der magnetfelderzeugenden Spule keinen Einfluss auf den Vergleich haben. Die typische Oszillationsfrequenz der SQUIDs beträgt 0.5 mT und die Driftrate der Spule liegt im Bereich von 5.5 µT/h. Um einen aussagekräftigen Vergleich durchführen zu können, müssen die Messungen an beiden SQUIDs in wenigen Stunden durchgeführt werden, damit der Gesamtdrift klein genug bleibt. Um diese Messgeschwindigkeit zu erreichen, wurde ein neues Messsystem zur Aufnahme des kritischen Stroms, basierend auf einem Echtzeit Microcontroller, entwickelt. Dies reduziert die Zeitskala der benötigten Messungen von Tagen auf Stunden und erlaubt es so, den gewünschten Vergleich durchzuführen. Nachdem alle Optimierungen im Messsystem realisiert wurden, konnte gezeigt werden, dass der Vergleich nun tatsächlich möglich ist. Erste Testmessungen mit dem alten Messsystem legen nahe, dass das asymmetrische SQUID ein Maximum bei $B = 0$ T zeigt und somit die homogene Bandlücke das wahrscheinlichere Resultat ist. Da nun alle messspezifischen Optimierungen abgeschlossen sind, sollte es den Nachfolgern dieses Projektes zukünftig möglich sein, die finale Messung durchzuführen.

Diese Arbeit hat gezeigt, dass es möglich ist, Supraleitung in verspanntem HgTe zu induzieren. Es wurde somit die grundlegendste Probengeometrie realisiert, die von Fu und Kane in 2008 für das Auftreten von Majorana Zuständen vorgeschlagen wurde. Ausgehend von dieser Vorarbeit kann nun das Regime der induzierten Supraleitung in verspanntem HgTe weiter erforscht werden, um schlussendlich in einen Bereich vorzustoßen, in dem Majorana Zustände zugleich stabil und messbar sind.

A

USED MATERIALS AND PRODUCED SAMPLES

A.1 USED MATERIALS

The MBE grown hetero-structures used in this thesis were bulk materials, meaning the functional HgTe layer was thicker than 50 nm and thus well above the limit for a 2-dimensional layer. In the following table waver number Q#, HgTe layer thickness d(HgTe), carrier density n and mobility μ are listed.

Q#	d(HgTe)/nm	$n/10^{11}\mathrm{cm}^{-2}$	$\mu/10^{3}\mathrm{cm}^{2}\mathrm{V}^{-1}\mathrm{s}^{-1}$	comment
Q2321	66	20	23	
Q2446	52	5	27	
Q2461	70	5.5	26	
Q2462	78	4.6	32	
Q2573	64	2.5	188	5 nm cap
Q2594	76	3.4	53	

A.2 PRODUCED SAMPLES

This section should give an idea of the development of superconducting contacts on HgTe over time. Here the more important samples are listed, including their biggest achievement or letdown.

Sample name	Date	Result/Problem
Q2321 Nb-SL_IV "Stripe"	20.08.2010	first contacts on HgTe mesa; superconductivity not stable at mesa step
Q2446 Nb-SL_VI "Frec"	15.07.2011	superconductor sputtered with angle but low transparent contact to mesa; indication of induced superconductivity and Andreev reflection
Q2462 Nb-SL_VI "Trans"	12.08.2011	even lower transparent contact to mesa

Sample name	Date	Result/Problem
Q2461 #1 Nb-SL_VIII "Lonely"	21.11.2011	contact area cleaning (Ar); induced superconductivity and Fraunhofer pattern; one cool-down with new filters
Q2461 #4 Nb-SL_IX "Quad"	20.03.2012	contact cleaning and fast transfer; separated structures; increased critical currents
Q2594 #1 SQUID_90_I "Shot"	19.10.2012	first SQUID and 90° SQUID; recognition of Nb aging problem
Q2594 #4 SQUID_IV "Flat"	05.03.2013	first use of AD-Win measurement system
Q2573 #1 SQUID_V "Shade"	31.10.2013	capped bulk; detection of oxford power supply as source of magnetic asymmetries
Q2594 #5 SQUID_V "Dots"	31.10.2013	removal of solder droplet (was a problem for flux trapping); comparison to graphene Josephson junction

B

LITHOGRAPHIC RECIPES

B.1 REMOVAL OF SUPERCONDUCTING RESIDUE

MBE grown samples are glued with Ga or In to the substrate holder during growth. This means one has superconducting residues on the backside of samples that need to be removed in order to exclude problems from interactions in magnetic field. The following process describes this procedure:

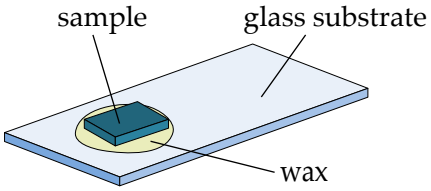

Figure 57: Sample mounted on glass substrate with wax. The functional layer is facing down and thus is protected by the wax layer.

- Clean glass substrate with acetone, isopropanol, deionized (DI)-water
- Melt wax on the glass substrate @ 80 °C
- After wax is cold, put the sample (front first) on it
- Heat up to 50 °C to melt the wax. Do not press on sample to keep spacing to glass.
- Put the glass substrate with the sample in HCl (37 %) solution and etch as long as bubbles are forming (~15 minutes). Repeatedly remove and dip the sample back into the solution to remove bubbles during etching.
- Rinse in DI-water
- Put in Trichloroethylene @ 50 °C to remove wax until sample drops from glass.
- Use metal tweezers to pick up the sample.
- Rinse in isopropanol and continue with a normal cleaning step.
- Clean in acetone (use ultrasonic (US)), isopropanol and DI-water.

B.2 SUPERCONDUCTING CONTACTS ON UNCAPPED BULK HGTE

This recipe was used to produce most samples in this thesis. Here only the final version will be presented.

Definition of mesa

- Cleave a sample piece (3 mm x 3 mm)
- Clean in acetone (use US), isopropanol and DI-water.
- Remove the superconducting residue as described in B.1 above.
- Deposit 10 nm of SiO in the PECVD (sacrificial layer)
- Spincoat with PMMA 950K 3 % in ethyl lactate
  - 7000 rpm (1) for 40 s
  - bake for 15 min @ 80 °C
- Expose with 2.5 kV and a dose of 70 $\mu C/cm^2$
  - 30 µm aperture
  - 805 x magnification; 81.92 µm writefield
  - 8 px $\longleftrightarrow$ 10 nm
- Development in isopropanol for 60 s
- Rinse in water and dry with nitrogen
- Evaporation of 20 nm of Ti
- Lift-off in acetone @ 50 °C for 25 min + 5 min (after having removed majority of metal with a spray of acetone)
- Rinse in isopropanol and DI-water.
- Remove SiO-layer in RIE (15 s SiN etch; 10 s mini clean)
- Ar etch through bulk layer (1 kV/1 kV/8 mA; ~30 nm/min)
- Remove etch mask with HF:H_2O = 1:10 solution for 50 s
- Rinse in DI-water; dry in nitrogen and continue with cleaning step.
- Clean in acetone (use US), isopropanol and DI-water.

Deposition of superconducor

The deposition of the superconductor and hence the creation of the S-TI interface is the most crucial step in the creation of such a sample.

- Repeat the steps of spincoating, exposure and development as mentioned above with the superconducting structure.
- Fit the sample onto the sample holder, that will be used for sputtering. Take care of the correct orientations needed for angled sputtering!
- Cleaning of the contact area with 6 s of Ar plasma. (up to 12 s possible with this resist, but lift-off quality will already suffer greatly)
- Fastest possible transfer to the sputter chamber to minimize oxidation time. (should be between 30 s and 40 s)
- Let the system pump down and open the plate valve of the load-lock to the main chamber. Wait for several minutes.
- Close the plate valve, still keeping the sample in the load-lock, and presputter Nb to clean the target and the chamber.
  - Nb – 400 W – Setpoint A – 100 s (~48 nm)
- Transfer the sample to the main chamber and angle it to $\alpha = 20°$. (WARNING: Angle on chamber is a *relative* scale!)
- Sputter the functional layer while keeping the angle relative to the target. The first layer is the most important and should be started as soon as possible to have the minimum amount of contamination.
  - Nb – 400 W – Setpoint A – 142 s (~68 nm)
  - Al – 50 W – Setpoint A – 113 s (~10 nm)
  - Ru – 100 W – Setpoint A – 50 s (~10 nm)
- Lift-off in acetone @ 50 °C for 25 min + 5 min (after having removed majority of metal with a spray of acetone)
- Rinse in isopropanol and DI-water.

Metallic contacts

In this step the bond pads are created and contacted to the e-beam written superconductor.

- Position sample in spincoater.
- Put HMDS on the sample surface and wait 20 s.
- Spin at 6000 rpm for 20 s
- Spincoat with ARN 4340 at 6000 rpm for 20 s
- Bake for 2 min @ 80 °C
- Expose for 20 s (8 W)
- Post-bake for 6 min at 80 °C

- Develop in AR 300-47 for 35 s to 50 s (normally 50 s was used)
- Clean contact area with 10 s of Ar plasma etching
- Evaporate the following layers
  - AuGe – 50 nm
  - Ti – 5 nm
  - Au – 50 nm
- Lift-off in acetone @ 50 °C for 7 min + 3 min (after having removed majority of metal with a spray of acetone)
- Rinse in isopropanol and DI-water.

The sample is now finished and can be bonded normally.

B.3 SUPERCONDUCTING CONTACTS ON HGTE-2DEG

This is the initial recipe for creating contacts to a 2DEG. The process described here will probably change in the future and should not be taken directly from here without talking to any successor.

Definition of mesa

- Cleave a sample piece (3 mm x 3 mm)
- Clean in acetone (use US), isopropanol and DI-water.
- Remove the superconducting residue as described in B.1 above.
- Deposit 10 nm of SiO in the PECVD (sacrificial layer)
- Spincoat with PMMA 950K 3 % in ethyl lactate
  - 7000 rpm (1) for 40 s
  - bake for 15 min @ 80 °C
- Expose with 2.5 kV and a dose of 70 $\mu C/cm^2$
  - 30 µm aperture
  - 805 x magnification; 81.92 µm writefield
  - 8 px $\longleftrightarrow$ 10 nm
- Development in isopropanol for 60 s
- Rinse in water and dry with nitrogen
- Evaporation of 20 nm of Ti
- Lift-off in acetone @ 50 °C for 25 min + 5 min (after having removed majority of metal with a spray of acetone)

- Rinse in isopropanol and DI-water.
- Remove SiO-layer in RIE (15 s SiN etch; 10 s mini clean)
- Ar etch through bulk layer (1 kV/1 kV/8 mA; ~30 nm/min)
- Remove etch mask with HF:H_2O = 1:10 solution for 50 s
- Rinse in DI-water; dry in nitrogen and continue with cleaning step.
- Clean in acetone (use US), isopropanol and DI-water.

Deposition of superconducor

The following PMMA resist layer is intended to endure an etch process of up to 1 minute and can afterwards still be used as a lift-off resist.

- Spin *two layers* of PMMA 200K 4 % in ethyl lactate
  - 6500 rpm (1) for 40 s
  - bake for 1 min/15 min @ 80 °C
- Spincoat with PMMA 950K 5 % in ethyl lactate
  - 5000 rpm (1) for 40 s
  - bake for 15 min @ 80 °C
- Expose with 6 kV and a dose of 150 µC/cm^2
  - 30 µm aperture
  - 845 x magnification; 81.92 µm writefield
  - 8 px $\longleftrightarrow$ 10 nm
- Ar etch through top cap (1 kV/1 kV/8 mA; ~30 nm/min)
- Fastest possible transfer to the evaporation chamber to minimize oxidation time. (should be between 30 s and 40 s)
- Evaporate:
  - 10 nm Ti
  - 180 nm Al
  - 5 nm Ti
  - 20 nm Au
- Lift-off in acetone @ 50 °C for 25 min + 5 min (after having removed majority of metal with a spray of acetone)
- Rinse in isopropanol and DI-water.

Metallic contacts

In this step the bond pads are created and contacted to the e-beam written superconductor.

- Position sample in spincoater.
- Put HMDS on the sample surface and wait 20 s.
- Spin at 6000 rpm for 20 s
- Spincoat with ARN 4340 at 6000 rpm for 20 s
- Bake for 2 min @ 80 °C
- Expose for 20 s (8 W)
- Post-bake for 6 min at 80 °C
- Develop in AR 300-47 for 35 s to 50 s (normally 50 s was used)
- Clean contact area with 10 s of Ar plasma etching
- Evaporate the following layers
  - AuGe – 50 nm
  - Ti – 5 nm
  - Au – 50 nm
- Lift-off in acetone @ 50 °C for 7 min + 3 min (after having removed majority of metal with a spray of acetone)
- Rinse in isopropanol and DI-water.

Insulator

- Deposition of 110 nm SiN/SiO superlattice in PECVD
- Spincoat with ECI 3027 at 6000 rpm for 20 s
- Bake for 2 min @ 80 °C
- Expose for 17 s (8 W)
- Develop in AZ 726-47 for 16 s.
- Dip in BOE (buffered oxide etch; HF:$NH_4F = 1 : 7$) for 13 s.
- Rise in DI-water for 2 min.
- Removal of resist in aceton.
- Rinse in isopropanol and DI-water.

Gate

The deposition of the gate metal is a repetition of the *Metallic Contacts* process step, with a different mask and without the contact cleaning with Ar.

The sample is now finished and can be bonded normally.

C

SOURCE CODE

C.1 SOURCE CODE FOR ADWIN 16 LIGHT THRESHOLD MEASUREMENT TECHNIQUE

Complete source code of threshold measurement on ADwin 16 light written in the basic dialect ADbasic.

```
'<region> comment
' written by Luis Maier
' August 2013
'
' This program is intended to measure the critical current in a superconductor.
'
' To do so this programm outputs a voltage ramp that drives a current through the
    superconductor.
'
' Parameters of the voltage ramp:
'    * Start Voltage
'    * End Voltage
'    * Slope
'
' At the same time the voltage drop over the sample is measured. As soon as one
   measures a voltage bigger
' than the threshold value the current (voltage at the reference resistance) as
   well as the output voltage
' is recorded. This measurement can be repeated many times very fast to extract
   the statistical
' properties of the current.
'
' Extra features:
'
'    * To ensure the thermal relaxation of the sample
'      after one cycle a pause time can be set.
'    * To protect the sample the start and end values are
'      not directly set, but the device sweeps at a defined speed.
'
'<endregion>

#include ADWL16.Inc

'<region> define block
'####################
```

```
'### Define block ###
'####################

' event is called every * cycles (25 ns per cycle)
#define PROCESS_DELAY 200

' time the system stays at RAMP_PAUSE_VOLTAGE (0 V) in s
#define DELAY_TIME 0.0002

#define RAMP_SLOPE_INIT 65535 ' slope of ramp to drive to start and from end
    parameter in V/s
#define RAMP_PAUSE_VOLTAGE 0  ' voltage that is used in breaks/at beginning/at
    end

#define INPUT_VOLTAGE_SAMPLE 1 ' channel of the sample voltage (threshold
    comparison)
#define INPUT_VOLTAGE_REF 3    ' channel of the reference voltage (current
    measurement)

' state of the measurement
#define STATE_PAUSE 0 ' 0 = pause
#define STATE_BEGIN 1 ' 1 = sweep to begin
#define STATE_RAMP  2 ' 2 = ramp voltage up
#define STATE_END   3 ' 3 = return to pause

#define MAX_ITERATIONS 100000 ' maximum amount of iterations needs to be known
    for memory assignment

' create aliases for input and output variables
#define Par_Running      Par_1 ' 1 if programm is still running; 0 else

#define Par_iterations         Par_2 ' number of measurement iterations
#define Par_measurement_number Par_3 ' number of successful measurements (
    threshold value reached)

#define FPar_ramp_start  FPar_1 ' start of ramp in volts
#define FPar_ramp_end    FPar_2 ' end of ramp in volts
#define FPar_ramp_slope  FPar_3 ' slope of ramp in V/s

#define FPar_threshold   FPar_4 ' maximum (minimum) voltage where the ramp stops
    and the programm returns the measured value

#define FPar_measurement    FPar_5 ' result of the measurement
#define FPar_output_voltage FPar_6 ' output voltage

#define Data_measurement    Data_1 ' measurement data
#define Data_output_voltage Data_2 ' output voltage data
'<endregion>

'<region> Variable definitions
'############################
' ### Variable definitions ###
'############################
```

```
dim output_voltage_1 as long ' voltage at output 1

' ramp parameters in long for internal use
dim ramp_start_l as long
dim ramp_end_l as long
dim ramp_slope_l as long
dim ramp_slope_init_l as long

dim ramp_pause_voltage_l as long ' long representation of RAMP_PAUSE_VOLTAGE
dim delay_time_l as long         ' long representation of DELAY_TIME

dim voltage_threshold_l as long ' long representation of threshold value
dim voltage_measure_l as long   ' shortly store measurement data

dim state as long         ' holds the momentary state of the measurement
dim state_counter as long ' how many cicles should the state be kept? (Used in
    STATE_PAUSE)

dim measure as long                                ' 1 the threshold is reached and
     a measurement should be taken, 0 continue
dim Data_measurement[MAX_ITERATIONS] as float    ' holds the measurement data
dim Data_output_voltage[MAX_ITERATIONS] as float ' holds the output voltage data
dim sum as float                                   ' sum of all measurement values
    (for average)

dim index as long ' used in for loops
'<endregion>

'<region> Functions
'#################
'### Functions ###
'#################

''' converts a voltage (+10 V to -10 V) given in float to the corresponding long
    value
''' volts: voltage to convert
function voltage_to_long( volts ) as long
  voltage_to_long = round((volts / 10.0 + 1)*32768)
endfunction

''' Converts a long value to its corresponding voltage in float (+10 V to -10 V).
''' volts_l: voltage value in long
function long_to_voltage( volts_l ) as float
  long_to_voltage = (volts_l/32768.0 - 1) * 10
endfunction

''' Convert slopes from V/s to voltage steps/cycle
''' volts_per_second: slope to convert to machine numbers
function vs_to_sc( volts_per_second ) as long
  vs_to_sc = round(voltage_to_long(volts_per_second)*25.0E-9*PROCESS_DELAY)
endfunction
'<endregion>
```

```
Init:
  Par_running = 1 ' programm is still running

  processdelay = PROCESS_DELAY ' set processdelay
  delay_time_l = round(DELAY_TIME/25.0E-9/PROCESS_DELAY) ' convert real time to
      cycles (25 ns equals one cycle)
  ramp_pause_voltage_l = voltage_to_long(RAMP_PAUSE_VOLTAGE) ' calculate
      RAMP_PAUSE_VOLTAGE as long

  ' Set voltage at output 1 to RAMP_PAUSE_VOLTAGE (0 V)
  output_voltage_1 = ramp_pause_voltage_l
  DAC(1, output_voltage_1)

  state = STATE_PAUSE           ' set initial state
  state_counter = delay_time_l  ' amount of wait cycles
  measure = 0                   ' only measure as threshold is reached
  Par_measurement_number = 0    ' start at 0 measurements

  ' convert voltages from float to long
  ramp_start_l = voltage_to_long(FPar_ramp_start)
  ramp_end_l = voltage_to_long(FPar_ramp_end)

  voltage_threshold_l = voltage_to_long(FPar_threshold)

  ' convert slopes from V/s to voltage steps/cycle
  ramp_slope_l = vs_to_sc(absf(FPar_ramp_slope))
  ramp_slope_init_l = vs_to_sc(absf(RAMP_SLOPE_INIT))


Event:
  ' end measurement after all iterations
  if( Par_iterations = 0 ) then
    end
  endif

  selectcase state
    case STATE_PAUSE ' wait until state change
      dec state_counter
      if(state_counter <= 0) then
        state = STATE_BEGIN
      endif


    case STATE_BEGIN ' change voltage to 'ramp_start_l'
      if(absi(output_voltage_1 - ramp_start_l) < ramp_slope_init_l) then
        ' set voltage to wanted value if the distance is samller than
            ramp_slope_init_l
        ' and enter the next state
        output_voltage_1 = ramp_start_l
        state = STATE_RAMP
      else
```

```
    ' go one step torwards 'ramp_start_l'
    if(output_voltage_1 - ramp_start_l < 0) then
      output_voltage_1 = output_voltage_1 + ramp_slope_init_l
    else
      output_voltage_1 = output_voltage_1 - ramp_slope_init_l
    endif
  endif
  DAC(1, output_voltage_1)


case STATE_RAMP ' change voltage torwards 'ramp_end_l'
  ' get voltage at sample channel
  voltage_measure_l = ADC(INPUT_VOLTAGE_SAMPLE)

  ' check if threshold is met
  if (ramp_end_l - ramp_start_l > 0) then
    ' going in positive direction
    if( voltage_measure_l > voltage_threshold_l) then
      measure = 1 ' take measurement
    endif
  else
    ' going in negative direction
    if( voltage_measure_l < voltage_threshold_l) then
      measure = 1 ' take measurement
    endif
  endif

  ' if threshold is reached take measurement and continue to STATE_END
  if( measure = 1 ) then
    ' take and store measurement
    FPar_measurement = long_to_voltage(ADC(INPUT_VOLTAGE_REF))
    FPar_output_voltage = long_to_voltage(output_voltage_1)

    inc Par_measurement_number

    Data_measurement[Par_measurement_number] = FPar_measurement
    Data_output_voltage[Par_measurement_number] = FPar_output_voltage

    dec Par_iterations ' one measurement cycle finnished
    state = STATE_END
    measure = 0
  endif

  ' continue voltage ramp
  if(absi(output_voltage_1 - ramp_end_l) < ramp_slope_l) then
    ' set voltage to wanted value if the distance is samller than
        ramp_slope_init_l
    ' and enter the next state
    output_voltage_1 = ramp_end_l
    dec Par_iterations ' one measurement cycle finnished, no measurement was
        possible
    state = STATE_END
  else
```

```
        ' go one step torwards 'ramp_end_l'
        if(output_voltage_1 - ramp_end_l < 0) then
          output_voltage_1 = output_voltage_1 + ramp_slope_l
        else
          output_voltage_1 = output_voltage_1 - ramp_slope_l
        endif
      endif
      DAC(1, output_voltage_1)


    case STATE_END ' change voltage to ramp_pause_voltage_l (0 V)
      if(absi(output_voltage_1 - ramp_pause_voltage_l) < ramp_slope_init_l) then
        ' set voltage to wanted value if the distance is samller than
            RAMP_SLOPE_INIT
        ' and enter the next state
        output_voltage_1 = ramp_pause_voltage_l
        state = STATE_PAUSE
        state_counter = delay_time_l
      else
        ' go one step torwards 'ramp_pause_voltage_l'
        if(output_voltage_1 - ramp_pause_voltage_l < 0) then
          output_voltage_1 = output_voltage_1 + ramp_slope_init_l
        else
          output_voltage_1 = output_voltage_1 - ramp_slope_init_l
        endif
      endif
      DAC(1, output_voltage_1)

  endselect


Finish:
  ' Set voltage to ramp_pause_voltage_l (0 V)
  do
    ' go stepwise torwards 'ramp_pause_voltage_l'
    if(output_voltage_1 - ramp_pause_voltage_l < 0) then
      output_voltage_1 = output_voltage_1 + ramp_slope_init_l
    else
      output_voltage_1 = output_voltage_1 - ramp_slope_init_l
    endif
    DAC(1, output_voltage_1)
    sleep(100)
  until(absi(output_voltage_1 - ramp_pause_voltage_l) < ramp_slope_init_l)

  ' set final voltage
  output_voltage_1 = ramp_pause_voltage_l
  DAC(1, output_voltage_1)

  ' calculate average voltage at threshold
  if( Par_measurement_number = 0 ) then
    ' no measurements possible
    FPar_measurement = 1E30
  else
```

```
  ' calculate average value
  sum = 0.0
  for index = 1 to Par_measurement_number
    sum = sum + Data_measurement[index]
  next index
  FPar_measurement = sum / Par_measurement_number

  ' calculate average maximum output voltage
  sum = 0.0
  for index = 1 to Par_measurement_number
    sum = sum + Data_output_voltage[index]
  next index
  FPar_output_voltage = sum / Par_measurement_number
endif

Par_running = 0 ' programm has finnished and the result can be collected
```

LIST OF FIGURES

LIST OF TABLES

BIBLIOGRAPHY

[1] I. B. Cohen. *Howard Aiken: Portrait of a Computer Pioneer*. MIT Press, second prinitng edition, October 2000. (Cited on page 11.)

[2] D. W. Jorgenson, M. S. Ho, and J. D. Samuels. World klems conference. In *Long-term Estimates of U.S. Productivity and Growth*, 2014. (Cited on page 11.)

[3] J. Held, J. Bautista, and S. Koehl. From a few cores to many: A tera-scale computing research overview. *White Paper Research at Intel*, 2005. (Cited on page 11.)

[4] J. Owens, M. Houston, D. Luebke, S. Green, J. Stone, and J. Phillips. Gpu computing. *Proceedings of the IEEE*, 96(5):879–899, May 2008. (Cited on page 11.)

[5] P. Shor. Polynomial-time algorithms for prime factorization and discrete logarithms on a quantum computer. *SIAM Journal on Computing*, 26(5):1484–1509, 1997. (Cited on page 12.)

[6] I. L. Chuang, R. Laflamme, P. W. Shor, and W. H. Zurek. Quantum computers, factoring, and decoherence. *Science*, 270(5242):1633–1635, 1995. (Cited on page 12.)

[7] W. G. Unruh. Maintaining coherence in quantum computers. *Phys. Rev. A*, 51:992–997, Feb 1995. (Cited on page 12.)

[8] A. Peres. *Quantum Theory: Concepts and Methods (Fundamental Theories of Physics)*, volume 72. Kluwer Academic Publishers, 2002. Chap. 9-4. (Cited on page 12.)

[9] D. Gottesman. An introduction to quantum error correction and fault-tolerant quantum computation. *ArXiv*, 0904.2557, Apr. 2009. (Cited on page 12.)

[10] P. W. Shor. Scheme for reducing decoherence in quantum computer memory. *Phys. Rev. A*, 52:R2493–R2496, Oct 1995. (Cited on page 12.)

[11] A. Imamoglu, D. D. Awschalom, G. Burkard, D. P. DiVincenzo, D. Loss, M. Sherwin, and A. Small. Quantum information processing using quantum dot spins and cavity QED. *Phys. Rev. Lett.*, 83:4204–4207, Nov 1999. (Cited on page 12.)

[12] D. L. Moehring, P. Maunz, S. Olmschenk, K. C. Younge, D. N. Matsukevich, L.-M. Duan, and C. Monroe. Entanglement of single-atom quantum bits at a distance. *Nature*, 449(7158):68–71, Sept. 2007. (Cited on page 12.)

[13] L. M. K. Vandersypen, M. Steffen, G. Breyta, C. S. Yannoni, M. H. Sherwood, and I. L. Chuang. Experimental realization of Shor's quantum factoring algorithm using nuclear magnetic resonance. *Nature*, 414(6866):883–887, Dec. 2001. (Cited on page 12.)

[14] C. Nayak, S. H. Simon, A. Stern, M. Freedman, and S. Das Sarma. Non-abelian anyons and topological quantum computation. *Rev. Mod. Phys.*, 80:1083–1159, Sep 2008. (Cited on page 12.)

[15] L. Fu and C. L. Kane. Superconducting proximity effect and majorana fermions at the surface of a topological insulator. *Phys. Rev. Lett.*, 100:096407, Mar 2008. (Cited on pages 12, 15, 25, 30, 32, 33, 51, 79, 81, and 89.)

[16] C. Brüne, C. X. Liu, E. G. Novik, E. M. Hankiewicz, H. Buhmann, Y. L. Chen, X. L. Qi, Z. X. Shen, S. C. Zhang, and L. W. Molenkamp. Quantum hall effect from the topological surface states of strained bulk HgTe. *Phys. Rev. Lett.*, 106:126803, Mar 2011. (Cited on pages 13 and 24.)

[17] L. Fu and C. L. Kane. Topological insulators with inversion symmetry. *Phys. Rev. B*, 76:045302, Jul 2007. (Cited on page 13.)

[18] C. Beenakker. Search for majorana fermions in superconductors. *Annual Review of Condensed Matter Physics*, 4(1):113–136, 2013. (Cited on pages 15, 29, 33, and 81.)

[19] D. J. Chadi, J. P. Walter, M. L. Cohen, Y. Petroff, and M. Balkanski. Reflectivities and electronic band structures of CdTe and HgTe. *Phys. Rev. B*, 5:3058–3064, Apr 1972. (Cited on pages 16 and 133.)

[20] M. Martyniuk, J. M. Dell, and L. Faraone. *in: Mercury Cadmium Telluride*. A John Wiley and Sons, Ltd., 2011. Editors: Peter Capper and James W. Garland. (Cited on page 15.)

[21] J. F. Nye. *Physical properties of crystals Their representation by thensors and matrices*. Oxford University Press, 1957. (Cited on page 16.)

[22] G. L. Bir and G. Pikus. *Symmetry and strain-induced effects in semiconductors*. John Wiley & Sons, 1974. (Cited on page 17.)

[23] S. Adachi. *Properties of Semiconductor Alloys: Group-IV, III-V and II-VI Semiconductors*. John Wiley & Sons, Ltd, 2009. (Cited on page 17.)

[24] R. I. Barabash, J. S. Chung, and M. F. Thorpe. Lattice and continuum theories of huang scattering. *Journal of Physics: Condensed Matter*, 11(15):3075, 1999. (Cited on page 17.)

[25] O. A. Pankratov. Electronic properties of band-inverted heterojunctions: supersymmetry in narrow-gap semiconductors. *Semiconductor Science and Technology*, 5(3S):S204, 1990. (Cited on page 18.)

[26] M. Z. Hasan and C. L. Kane. Topological insulators. *Rev. Mod. Phys.*, 82:3045–3067, Nov 2010. (Cited on page 18.)

[27] C. Ames, P. Leubner, C. Brüne, C. Schumacher, H. Buhmann, and L. W. Molenkamp. Critical thickness and relaxation behavior of the topological insulator material HgTe. *In preparation*, 2014. (Cited on page 19.)

[28] C. Brüne, C. Thienel, M. Stuiber, J. Böttcher, H. Buhmann, E. G. Novik, C.-X. Liu, E. M. Hankiewicz, and L. W. Molenkamp. Dirac-screening stabilized surface-state transport in a topological insulator. *Phys. Rev. X*, 4:041045, Dec 2014. (Cited on pages 19 and 24.)

[29] K. von Klitzing. The quantized hall effect. *Rev. Mod. Phys.*, 58:519–531, Jul 1986. (Cited on page 20.)

[30] C. Brüne, C. X. Liu, E. G. Novik, E. M. Hankiewicz, H. Buhmann, Y. L. Chen, X. L. Qi, Z. X. Shen, S. C. Zhang, and L. W. Molenkamp. Supplemental material: Quantum hall effect from the topological surface states of strained bulk HgTe. *Phys. Rev. Lett.*, 106:126803, Mar 2011. (Cited on page 20.)

[31] K. S. Novoselov, A. K. Geim, S. V. Morozov, D. Jiang, M. I. Katsnelson, I. V. Grigorieva, S. V. Dubonos, and A. A. Firsov. Two-dimensional gas of massless dirac fermions in graphene. *Nature*, 438(7065):197–200, Nov. 2005. (Cited on page 21.)

[32] K. v. Klitzing, G. Dorda, and M. Pepper. New method for high-accuracy determination of the fine-structure constant based on quantized hall resistance. *Phys. Rev. Lett.*, 45:494–497, Aug 1980. (Cited on page 22.)

[33] C. Thienel. *Exploring the transport properties of the three-dimensional topological insulator material HgTe*. PhD thesis, Experimentelle Physik 3, Universität Würzburg, 2014. (Cited on page 24.)

[34] P. A. M. Dirac. The quantum theory of the electron. *Proceedings of the Royal Society of London. Series A*, 117(778):610–624, 1928. (Cited on page 25.)

[35] E. Majorana. Teoria simmetrica dell'elettrone e del positrone. *Il Nuovo Cimento*, 14(4):171–184, 1937. (Cited on page 25.)

[36] A. R. Akhmerov, J. Nilsson, and C. W. J. Beenakker. Electrically detected interferometry of majorana fermions in a topological insulator. *Phys. Rev. Lett.*, 102:216404, May 2009. (Cited on page 25.)

[37] J. Alicea. New directions in the pursuit of majorana fermions in solid state systems. *Reports on Progress in Physics*, 75(7):076501, 2012. (Cited on page 25.)

[38] H. K. Onnes. The resistance of pure mercury at helium temperatures. *Commun. Phys. Lab. Univ. Leiden*, 12:120+, 1911. (Cited on page 25.)

[39] W. Meissner and R. Ochsenfeld. Ein neuer Effekt bei Eintritt der Supraleitfähigkeit. *Naturwissenschaften*, 21(44):787–788, 1933. (Cited on page 26.)

[40] C. Kittel. *Introduction to Solid State Physics*. John Wiley & Sons, 2004. (Cited on page 26.)

[41] J. A. Thompson. Characterization of niobium films and a bulk niobium sample with RRR, SIMS and a SQUID magnetometer. *Journal of Undergraduate Research*, v3 #1, 2004. (Cited on pages 26, 56, and 57.)

[42] L. N. Cooper. Bound electron pairs in a degenerate fermi gas. *Phys. Rev.*, 104:1189–1190, Nov 1956. (Cited on page 26.)

[43] M. Tinkham. *Introduction to superconductivity*. McGraw-Hill Book Co., 1996. (Cited on pages 26, 27, 28, 68, 69, 70, 76, and 89.)

[44] M. Leijnse and K. Flensberg. Introduction to topological superconductivity and majorana fermions. *Semiconductor Science and Technology*, 27(12):124003, 2012. (Cited on page 27.)

[45] E. Maxwell. Isotope effect in the superconductivity of mercury. *Phys. Rev.*, 78:477–477, May 1950. (Cited on page 27.)

[46] C. A. Reynolds, B. Serin, W. H. Wright, and L. B. Nesbitt. Superconductivity of isotopes of mercury. *Phys. Rev.*, 78:487–487, May 1950. (Cited on page 27.)

[47] A. Mourachkine. Determination of the coherence length and the cooper-pair size in unconventional superconductors by tunneling spectroscopy. *Journal of Superconductivity*, 17(6):711–724, 2004. (Cited on page 27.)

[48] N. W. Ashcroft and N. D. Mermin. *Solid State Physics*. Saunders College, 1976. (Cited on page 27.)

[49] V. Novotny and P. Meincke. Single superconducting energy gap in pure niobium. *Journal of Low Temperature Physics*, 18(1-2):147–157, 1975. (Cited on pages 27 and 62.)

[50] S. Hunklinger. *Festkörperphysik*. Oldenbourg Verlag, 3. edition, 2011. (Cited on page 28.)

[51] N. Read and D. Green. Paired states of fermions in two dimensions with breaking of parity and time-reversal symmetries and the fractional quantum hall effect. *Phys. Rev. B*, 61:10267–10297, Apr 2000. (Cited on page 29.)

[52] X.-L. Qi and S.-C. Zhang. Topological insulators and superconductors. *Rev. Mod. Phys.*, 83:1057–1110, Oct 2011. (Cited on page 30.)

[53] K. D. Nelson, Z. Q. Mao, Y. Maeno, and Y. Liu. Odd-parity superconductivity in Sr_2RuO_4. *Science*, 306(5699):1151–1154, 2004. (Cited on pages 30, 89, and 93.)

[54] A. P. Mackenzie, R. K. W. Haselwimmer, A. W. Tyler, G. G. Lonzarich, Y. Mori, S. Nishizaki, and Y. Maeno. Extremely strong dependence of superconductivity on disorder in Sr_2RuO_4. *Phys. Rev. Lett.*, 80:161–164, Jan 1998. (Cited on page 30.)

[55] A. F. Andreev. Thermal conductivity of the intermediate state of superconductors. *Soviet Physics JETP*, 20:1490, 1965. (Cited on page 31.)

[56] H. Courtois, P. Gandit, B. Pannetier, and D. Mailly. Long-range coherence and mesoscopic transport in n-s metallic structures. *Superlattices and Microstructures*, 25(5-6):721 – 732, 1999. (Cited on pages 31, 32, and 133.)

[57] S. Guéron, H. Pothier, N. O. Birge, D. Esteve, and M. H. Devoret. Superconducting proximity effect probed on a mesoscopic length scale. *Phys. Rev. Lett.*, 77:3025–3028, Sep 1996. (Cited on page 32.)

[58] G. E. Blonder, M. Tinkham, and T. M. Klapwijk. Transition from metallic to tunneling regimes in superconducting microconstrictions: Excess current, charge imbalance, and supercurrent conversion. *Phys. Rev. B*, 25:4515–4532, Apr 1982. (Cited on pages 36, 58, and 59.)

[59] K. Jousten. *Handbook of vacuum technology*. John Wiley & Sons, 2008. (Cited on page 37.)

[60] Y. Koval, T. Borzenko, and S. Dubonos. Use of polymethylmethacrylate for pattern transfer by ion beam etching: Improvement of etching homogeneity and patterning quality. *Journal of Vacuum Science & Technology B*, 21(5):2217–2219, 2003. (Cited on page 38.)

[61] F. Pobell. *Matter and methods at low temperatures*, volume 2. Springer, 1996. (Cited on page 39.)

[62] U. Bockelmann and G. Bastard. Phonon scattering and energy relaxation in two-, one-, and zero-dimensional electron gases. *Phys. Rev. B*, 42:8947–8951, Nov 1990. (Cited on page 39.)

[63] S. Mandal, T. Bautze, R. Blinder, T. Meunier, L. Saminadayar, and C. Bäuerle. Efficient radio frequency filters for space constrained cryogenic setups. *Review of Scientific Instruments*, 82(2):–, 2011. (Cited on page 40.)

[64] J. Bardeen, G. Rickayzen, and L. Tewordt. Theory of the thermal conductivity of superconductors. *Phys. Rev.*, 113:982–994, Feb 1959. (Cited on page 42.)

[65] J. M. Martinis, M. H. Devoret, and J. Clarke. Experimental tests for the quantum behavior of a macroscopic degree of freedom: The phase difference across a josephson junction. *Phys. Rev. B*, 35:4682–4698, Apr 1987. (Cited on page 42.)

[66] Oxford Instruments Superconductivity. Remanent fields in superconducting magnets. Technical bulletin, Oxford Instruments Superconductivity Limited, Germany Otto-von Guericke Ring 10 D-65205 Wiesbaden, 2000. Ref: OI 557 12.00. (Cited on page 44.)

[67] S. S. Lorant. Superconducting shields for magnetic flux exclusion and field shaping. In *Superconducting Shields for Magnetic Flux Exclusion and Field Shaping*, volume 227, page 2. 4th International Conference on Magnet Technology, 1972. (Cited on page 44.)

[68] B. Josephson. Possible new effects in superconductive tunnelling. *Physics Letters*, 1(7):251 – 253, 1962. (Cited on pages 51 and 68.)

[69] C. T. Olund and E. Zhao. Current-phase relation for Josephson effect through helical metal. *Phys. Rev. B*, 86:214515, Dec 2012. (Cited on pages 51, 79, and 82.)

[70] M. Mohammad, M. Muhammad, S. Dew, and M. Stepanova. Fundamentals of electron beam exposure and development. In M. Stepanova and S. Dew, editors, *Nanofabrication*, pages 11–41. Springer Vienna, 2012. (Cited on page 54.)

[71] A. D. K. Finck, C. Kurter, Y. S. Hor, and D. J. Van Harlingen. Phase coherence and andreev reflection in topological insulator devices. *ArXiv e-prints*, Mar. 2014. (Cited on page 62.)

[72] L. Maier, J. B. Oostinga, D. Knott, C. Brüne, P. Virtanen, G. Tkachov, E. M. Hankiewicz, C. Gould, H. Buhmann, and L. W. Molenkamp. Induced superconductivity in the three-dimensional topological insulator hgte. *Phys. Rev. Lett.*, 109:186806, Nov 2012. (Cited on page 66.)

[73] J. B. Oostinga, L. Maier, P. Schüffelgen, D. Knott, C. Ames, C. Brüne, G. Tkachov, H. Buhmann, and L. W. Molenkamp. Josephson supercurrent through the topological surface states of strained bulk hgte. *Phys. Rev. X*, 3:021007, May 2013. (Cited on page 66.)

[74] H. Courtois, M. Meschke, J. T. Peltonen, and J. P. Pekola. Origin of hysteresis in a proximity josephson junction. *Phys. Rev. Lett.*, 101:067002, Aug 2008. (Cited on page 72.)

[75] K. Flensberg, J. B. Hansen, and M. Octavio. Subharmonic energy-gap structure in superconducting weak links. *Phys. Rev. B*, 38:8707–8711, Nov 1988. (Cited on pages 72, 88, and 135.)

[76] P. Dubos, H. Courtois, B. Pannetier, F. K. Wilhelm, A. D. Zaikin, and G. Schön. Josephson critical current in a long mesoscopic s-n-s junction. *Phys. Rev. B*, 63:064502, Jan 2001. (Cited on page 73.)

[77] A. Chrestin and U. Merkt. High characteristic voltages in Nb/p-type InAs/Nb josephson junctions. *Applied Physics Letters*, 70(23):3149–3151, 1997. (Cited on page 73.)

[78] B. A. Aminov, A. A. Golubov, and M. Y. Kupriyanov. Quasiparticle current in ballistic constrictions with finite transparencies of interfaces. *Phys. Rev. B*, 53:365–373, Jan 1996. (Cited on page 73.)

[79] F. Rohlfing. Induzierte Supraleitung in Nb/InAs-Hybridstrukturen in parallelen und senkrechten Magnetfeldern, April 2008. (Cited on pages 73 and 85.)

[80] M. Veldhorst, M. Snelder, M. Hoek, T. Gang, V. K. Guduru, X. L. Wang, U. Zeitler, W. G. van der Wiel, A. A. Golubov, H. Hilgenkamp, and A. Brinkman. Josephson supercurrent through a topological insulator surface state. *Nat Mater*, 11(5):417–421, May 2012. (Cited on page 74.)

[81] G. Eilenberger. Transformation of gorkov's equation for type ii superconductors into transport-like equations. *Zeitschrift für Physik*, 214(2):195–213, 1968. (Cited on page 74.)

[82] C. Beenakker and H. van Houten. Quantum transport in semiconductor nanostructures. In H. Ehrenreich and D. Turnbull, editors, *Semiconductor Heterostructures and Nanostructures*, volume 44 of *Solid State Physics*, pages 1 – 228. Academic Press, 1991. (Cited on pages 76 and 83.)

[83] R. Meservey and B. B. Schwartz. *Superconductivity*. Marcel Dekker Inc., 1969. (Cited on page 77.)

[84] A. I. Gubin, K. S. Il'in, S. A. Vitusevich, M. Siegel, and N. Klein. Dependence of magnetic penetration depth on the thickness of superconducting Nb thin films. *Phys. Rev. B*, 72:064503, Aug 2005. (Cited on page 81.)

[85] M. D. Fiske. Temperature and magnetic field dependences of the josephson tunneling current. *Rev. Mod. Phys.*, 36:221–222, Jan 1964. (Cited on page 85.)

[86] T. Klapwijk, M. Sepers, and J. Mooij. Regimes in the behavior of superconducting microbridges. *Journal of Low Temperature Physics*, 27(5-6):801–835, 1977. (Cited on page 85.)

[87] C. Tsuei and J. Kirtley. Pairing symmetry in cuprate superconductors. *Rev. Mod. Phys.*, 72:969–1016, Oct 2000. (Cited on pages 89 and 93.)

[88] D. A. Wollman, D. J. Van Harlingen, W. C. Lee, D. M. Ginsberg, and A. J. Leggett. Experimental determination of the superconducting pairing state in YBCO from the phase coherence of YBCO-Pb dc SQUIDs. *Phys. Rev. Lett.*, 71:2134–2137, Sep 1993. (Cited on page 89.)

[89] W. Buckel and R. Kleiner. *Supraleitung: Grundlagen und Anwendungen*. Wiley-VCH, 7th edition, november 2012. (Cited on page 89.)

[90] N. Byers and C. N. Yang. Theoretical considerations concerning quantized magnetic flux in superconducting cylinders. *Phys. Rev. Lett.*, 7:46–49, Jul 1961. (Cited on page 90.)

[91] T. V. Duzer and C. W. Turner. *Principles of Superconductive Devices and Circuits*. Elsevier, 1981. (Cited on page 91.)

[92] M. Sigrist and T. M. Rice. Unusual paramagnetic phenomena in granular high-temperature superconductors—a consequence of *d*- wave pairing? *Rev. Mod. Phys.*, 67:503–513, Apr 1995. (Cited on page 93.)

[93] H. B. Heersche, P. Jarillo-Herrero, J. B. Oostinga, L. M. K. Vandersypen, and A. F. Morpurgo. Bipolar supercurrent in graphene. *Nature*, 446(7131):56–59, Mar. 2007. (Cited on page 101.)

[94] S. Hart, H. Ren, T. Wagner, P. Leubner, M. Muhlbauer, C. Brune, H. Buhmann, L. W. Molenkamp, and A. Yacoby. Induced superconductivity in the quantum spin hall edge. *Nat Phys*, 10(9):638–643, Sept. 2014. (Cited on page 104.)

ACKNOWLEDGMENTS

I would like to thank the following people who all contributed in their way to this thesis.

- *Laurens W. Molenkamp* for the chance to work at EP3
- *Hartmut Buhmann* for accepting me into his workgroup, numerous helpful discussions as well as allowing and encouraging us to visit several conferences.
- *Jeroen Oostinga* who seriously increased my knowledge in the subject of superconductivity both theoretically and practically and played a major role in the publication of the first two papers on HgTe and superconductors.
- *Mathias Mühlbauer* was my first mentor and laid the foundation in the field of lithography during my Diploma thesis and still was a very important discussion partner through my complete PhD thesis.
- *Holger Thierschmann* did the same for me in the field of measurements and cryostat techniques.
- *Cornelius Thienel* who always was available for discussions, serious and not so serious ones alike.
- *Christopher Ames* and *Philipp Leubner* for the growth of the HgTe layers.
- My masters, who invested their time working on the superconducting project and in this way contributed to this work: *Daniel Knott*, *Peter Schüffelgen*, *Sebastian Schneider*, *Manuel Grimm*, *Christian Thurn*.
- *Oliver Herrmann* has prepared and measured the graphene samples of the last chapter and helped in discussions about superconductivity.
- *Erwann Bocquillon* and *Jonas Widenmann* who took over the superconducting project at the end of my thesis.
- *Andreas Budewitz*, who has helped me in many situations with his broad technical skills.
- All other group members not mentioned so far, only to name a few *Christoph Brüne*, *Bastian Büttner*, *Felicitas Gerhard*, *Rebekka Pfeuffer*, *Andreas Roth* and many more. All those people together created a very special atmosphere that I will miss in the future.
- *Claus Schumacher* for teaching me in network and server related topics.
- *Tanja Borzenko* for discussions about the development of lithographic recipes.
- Our cleanroom team *Volkmar Hock*, *Martin Zipf* and Petra *Wolf-Mueller* constantly helping with the machinery and chemistry.

- *Roland Ebert* and *Cornelius Sebastian Ziga* for the endless supply of helium and various tips and discussions concerning cryostat questions.

Especially I would like to thank my girlfriend *Teresa Schmeiler*, who supported me enormously during the course of this thesis and helped a lot with proof reading.

My parents *Christl* and *Rudi Maier* as well as my sister *Lilli Maier* for the extensive support during this experience.

I also want to mention the technical side of things and thank the development teams of the following free software products, who made the writing of the thesis possible.

The text was written in LyX with the use of LaTeX. The classicthesis format used was created by André Miede. For the graphical editing the following programs were used (only open source programs listed):

Inkscape 

GIMP 

Blender